TECHNISCHE UNIVERSITÄT WIEN

VIENNA UNIVERSITY OF TECHNOLOGY

DISSERTATION

Opto-Electronic Integrated Correlation Receivers for Time-of-Flight Based Distance Measurement Systems

ausgeführt zum Zwecke der Erlangung des akademischen Grades eines Doktors der technischen Wissenschaften unter der Leitung von

Univ. Prof. Dr.-Ing. Horst ZIMMERMANN
am Institut für Elektrische Mess- und Schaltungstechnik

eingereicht an der Technischen Universität Wien
Fakultät für Elektrotechnik und Informationstechnik

von

Dipl.-Ing. Klaus Oberhauser
Matr.-Nr.: 9726107
Gentzgasse 120/10
1180 Wien

Wien, im November 2006

Kurzfassung

Mit den heute zur Verfügung stehenden Sensortechnologien sind wir in der Lage, eine Vielzahl von physikalischen Größen zu messen. So gibt es eine große Anzahl von berührungslosen eindimensionalen Abstandssensoren. Für viele Steuerungs- und Überwachungsaufgaben wären aber 3D-Messsysteme notwendig. Der Vergleich verschiedener Abstandssensoren von Ultraschall über Radarsensoren bis hin zu optischen Sensoren führt zum Schluss, dass ein 3D-Messsystem, welches eine hohe laterale Auflösung aufweisen soll, nur unter Verwendung optischer Signale implementiert werden kann. Um ein kompaktes und robustes Sensordesign zu erreichen, müssen bewegliche Teile, wie z.B. rotierende Spiegel, unter allen Umständen vermieden werden. Aus diesem Grunde ist es das Ziel dieser Dissertation, einen monolithischen Sensor zu entwickeln, der in der Lage ist, Abstände in jedem einzelnen Pixel zu messen.

Diese Doktorarbeit befasst sich daher mit der Realisierung von neuen Pixelarchitekturen für solch einen optischen 3D-Abstandssensor. Das Messprinzip beruht auf der Bestimmung der Laufzeit eines optischen Signals von einer aktiven, optischen Beleuchtungsquelle hin zu einem zu vermessenden Objekt und zurück zum Empfangspixel. Dabei ergibt sich für den angestrebten maximalen Messbereich von bis zu $s_d = 15$m eine zu messende Signallaufzeit von $t_{tof} = 100$ns. Für eine gewünschte Auflösung im cm-Bereich ist es daher notwendig, Zeitintervalle von 66ps aufzulösen. Um diese kurzen Zeitintervalle messen und unterschiedliche Reflexionseigenschaften von verschiedenen Materialen unterdrücken zu können, wird eine Korrelation zwischen dem gesendeten und dem empfangenen Signal durchgeführt. Die Theorien über das Korrelationsprinzip und das Photonenrauschen, die für die Entwicklung eines Korrelationsempfängers nötig sind, werden in der vorliegenden Dissertation zusammenfassend dargestellt.

Im Rahmen dieser Arbeit wurden drei verschiedene Typen von Korrelationsempfängern in einer modifizierten 0.6µm BiCMOS Technologie entwickelt und charakterisiert. Die Umwandlung der empfangenen Lichtleistung in freie Ladungsträger erfolgt entweder mittels einer schnellen und effizienten integrierten PIN Photodiode oder mit einem neu entwickelten Detektor, der in der Lage ist, direkt eine opto-elektronische Korrelation durchzuführen, dem sog. Doppel-Anoden Photodetektor. Abhängig vom verwendeten Empfänger sind unterschiedliche Auswerteschaltungen notwendig.

Die erste Pixelarchitektur, die für Hochgeschwindigkeitsmessungen entwickelt wurde, besteht aus einer PIN Photodiode und einer aktiven Ausleseschaltung. Dabei wird ein einstufiger Transimpedanz-Verstärker als Vorverstärker verwendet. Eine darauf folgende analog-digitale Multiplizierer-Stufe, kombiniert mit einem aktiven Tiefpassfilter, führt die eigentliche Korrelation durch. Die Schaltung erzielt sehr kurze Messzeiten für eine einzelne Abstandsmessung von $t_{measure} = 500$µs für einen Messbereich von $s_d = 0.1$m−3.7m. Bei einem maximalen Linearitätsfehler von $s_{lin} = \pm 0.67\%$ wurde eine Standardabweichung von $\sigma_d = 4$cm erreicht. Die Gesamtfläche eines einzelnen Pixels beträgt $A_{pixel} = 220 \times 400 \mu m^2$.

Auch die zweite Ausleseschaltung, die Brücken-Korrelator-Schaltung, verwendet eine PIN Photodiode als Detektorelement. Die komplett passive Brücken-Korrelator-Schaltung ist in der Lage, die notwendige Korrelation, sowie eine perfekte Hintergrundlichtunterdrückung parallel durchzuführen. Auf Grund der passiven Schaltung und dem damit verbundenen geringen Stromverbrauch ist der Brücken-Korrelator sehr gut für multi-pixel Lösungen geeignet. Für einen Messbereich von $s_d = 0.1\text{m}-3.7\text{m}$ erreicht die Schaltung eine ebenfalls kurze Messzeit von $t_{measure} = 2\text{ms}$ und einen Linearitätsfehler von $s_{lin} = \pm 0.47\%$. Die erzielte Standardabweichung beträgt $\sigma_d = 2\text{cm}$. Die Pixelfläche beträgt $A_{pixel} = 250\times 200\mu\text{m}^2$.

Durch erweitern der Brücken-Korrelator-Schaltung mit einem aktiven Verstärker wird es möglich die Empfindlichkeit der Schaltung zu erhöhen. Der in der ursprünglichen Schaltung auftretende Sättigungseffekt kann dadurch beseitigt und somit die gewünschte integrierende Funktion realisiert werden. Hintergrundlicht wird auch von dem IC der dritten Generation unterdrückt. Ohne nachjustieren des optischen Aufbaues wurde ein Messbereich von $s_d = 0.7\text{m}-3.4\text{m}$ erzielt. Der Linearitätsfehler beträgt $s_{lin} = \pm 0.58\%$. Die Standardabweichung für eine Messzeit von $t_{measure} = 5\text{ms}$ über den gesamten Messbereich ist kleiner als $\sigma_d = 1.4\text{cm}$. Durch die geringe Pixelfläche von $A_{pixel} = 85\times 180\mu\text{m}^2$ wurde ein optischer Füllfaktor von $\eta_{fill} = 61\%$ erzielt.

Die empfindlichste Ausleseschaltung dieser Dissertation verwendet einen korrelierenden Doppel-Anoden Photodetektor (DAP) als Empfangselement. Durch das einseitige Modulieren des DAP wird es möglich, an der Auslese-Anode einen abstandsabhängigen Gleichstrom zu messen. Damit wird verhindert, dass auch an der Ausleseelektrode die Modulationsspannung mit ihrer hohen Amplitude auftritt. Durch die Verwendung einer aktiven Transimpedanz-Stufe als Ausleseschaltung konnten Objektabstände im Bereich von $s_d = 0.1\text{m}-15\text{m}$ vermessen werden. Ein sehr geringer Linearitätsfehler von $s_{lin} = \pm 0.23\%$ wurde festgestellt. Die maximale Standardabweichung beträgt $\sigma_d = 3.4\text{cm}$ Die Gesamtfläche der in jedem Pixel notwendigen Schaltungselemente beträgt nur $A_{pixel} = 150\times 220\mu\text{m}^2$.

Abstract

Using today's sensor technology we are able to measure a wide range of physical quantities. Various one-dimensional contactless distance measurement sensors are available. However, for many supervision tasks three-dimensional vision systems would be of great importance. Comparison of different distance measurement sensors ranging from ultrasound- over radar-based solutions to optical sensors leads to the result that a high-resolution 3D imager has to rely on active optical signals. To reach a compact and robust sensor solution, moving parts like e.g. rotating mirrors have to be avoided altogether. Therefore an all solid-state sensor capable of measuring object distances within every pixel is intended.

This thesis deals with the realisation of new pixel architectures for optical 3D distance measurement sensors. The measurement principle is based on the determination of the time-of-flight from an actively transmitted optical signal to an object and back to the receiving pixel. The aspired mid-distance measurement range of up to s_d = 15m results in a maximum signal runtime of t_{tof} = 100ns, which has to be resolved in 66ps steps to reach a resolution of 1cm. To measure these short time intervals and to suppress the influence of different object reflectivity correlation between sent and received signal is performed. All theory concerning the correlation principle and the photon noise, necessary to design a correlation receiver is included in this thesis.

In a modified 0.6µm BiCMOS technology three different correlating receiver structures were developed and characterised during this work. The detection of the received optical power is performed either by a fast and efficient integrated PIN photodiode or by a newly developed opto-electronic correlation detector, the so-called double-anode photodetector. Depending on the detector element different readout circuits are necessary.

The first pixel architecture intended for high-speed distance measurements consists of a PIN photodiode and an active readout circuit. A single-stage transimpedance amplifier is used as pre-amplifier. A subsequent analogue-digital multiplication stage in combination with an active low-pass filter performs the correlation. A very short single distance measurement time of $t_{measure}$ = 500µs and a linearity error of s_{lin} = ±0.67% for a distance measurement range of s_d = 0.1m−3.7m are reached. The standard deviation of a single-shot measurement is σ_d = 2cm. The occupied pixel area is A_{pixel} = 220×400µm^2.

The second readout circuit, the so-called bridge-correlator circuit, also uses a PIN photodiode as receiving element. The all-passive bridge-correlator performs the correlation and perfectly suppresses any background light at the same time. Due to the all passive setup it is well suited for multi-pixel integration. For a distance measurement range of s_d = 0.1m−3.7m, still a short single distance measurement time of $t_{measure}$ = 2ms is reached. The maximum linearity error is s_{lin} = ±0.47%. The standard deviation is σ_d = 2cm. The overall pixel size is A_{pixel} = 250×200µm^2.

By adding an active amplifier to the bridge-correlator circuit it was possible to enhance the sensitivity of the circuit. Saturation effects are avoided and the desired integration operation is performed. Background light is also suppressed by this third-generation

opto-electronic integrated circuit (OEIC). Without adjusting the opto-mechanical measurement setup a distance range of $s_d = 0.7\text{m}-3.4\text{m}$ is reached. The linearity error is $s_{lin} = \pm 0.58\%$ and the standard deviation is only $\sigma_d = 1.4\text{cm}$. The single distance measurement time is $t_{measure} = 5\text{ms}$. For a pixel area of only $A_{pixel} = 85\times180\mu\text{m}^2$ a very high optical fill factor of $\eta_{fill} = 61\%$ is achieved.

The most sensitive circuit structure introduced in this thesis is based on a double-anode photodetector. By performing a single-sided modulation of the DAP device, it is possible to readout a DC current containing the distance information and to avoid the large-signal modulation voltage at the output terminal. The use of an active transimpedance stage as readout circuit enables the measurement of distances within the range of $s_d = 0.1\text{m}-15\text{m}$. A linearity error of $s_{lin} = \pm 0.23\%$ and a standard deviation of $\sigma_d = 3.4\text{cm}$ are achieved. The total pixel size including all necessary functional components is $A_{pixel} = 150\times220\mu\text{m}^2$.

Acknowledgement

From the circuit design group at the Institute of Electrical Measurement and Circuit Design at the Vienna University of Technology, I would like to thank all colleagues for their suggestion and their support, especially Gerald Zach for valuable discussions for the latest OEIC developments. My special thanks go to Alexander Nemecek who has been working with me on the problem of optical distance measurement systems from the beginning.

I further have to thank Dr. Gernot Languth and DI Holger Wille from Infineon Technologies for their constructive cooperation and technical support for the OEIC fabrication.

I want to give special thanks to Univ.Prof. Mag.rer.nat. Dr.techn. Horst Zimmermann for making this work possible and for his great encouragement and Univ.Prof. Dipl.-Ing. Dr.techn. Michael Vellekoop for the examination of this thesis.

Furthermore I would like to thank Dr. Ines Kastil for proofreading and especially for supporting me during this work.

Contents

List of Figures

List of Tables

List of Abbreviations

2D/3D	two/three-dimensional
ADC	analogue-to-digital converter
APD	avalanche photodiode
ARC	anti-reflection coating
CB	conduction band
CCD	charge coupled device
CDS	correlated double sampling
CMOS	complementary metal-oxide-semiconductor
CPLD	complex programmable logic device
CW	continuous-wave
DAP	double-anode photodetector
DFT	discrete Fourier transform
DSP	digital signal processor
DSO	digital storage oscilloscope
FFT	fast Fourier transform
FMCW	frequency modulated continuous-wave
FPGA	field-programmable gate array
IC	integrated circuit
LED	light emitting diode
MSM	metal-semiconductor-metal technology
OEIC	opto-electronic integrated circuit
OPA	operational amplifier
OTA	operational transconductance amplifier
PCB	printed circuit board
PMD	photonic mixer device
PSD	position sensitive device
PSK	phase-shift keying
RMS	root mean square
S/D	source/drain
SGV	self guided vehicle

SNR	signal-to-noise ratio
SPAD	single photon avalanche diode
TDC	time to digital converter
TIA	transimpedance amplifier
TOF	time-of-flight
TVC	time to voltage converter
VB	valence band

List of Symbols

A_{amp}	1	amplifier gain
A_{lens}	m^2	lens area
A_{pd}	m^2	photodiode area
A_{pixel}	m^2	pixel area
A_v	1	open loop gain
C_{A1A2}	F	coupling capacitance of DAP anodes
C_{CA1}, C_{CA2}	F	parasitic capacitances of DAP
C_{fb}	F	parasitic capacitance of R_{fb}
C_{GS}, C_{GD}	F	gate-to-source, gate-to-drain capacitance
C_{in}	F	input node capacitance
C_{int}	F	integration capacitance
C_{par1}, C_{par2}	F	parasitic capacitances of C_{int}
C_{par}	F	total parasitic capacitance of C_{int}
C_{pd}	F	photodiode capacitance
C'_{pd}	F/m	perimeter capacitance
C''_{pd}	F/m^2	area capacitance
c_0	299 792 458 m/s	vacuum speed of light
D_{pin}	–	PIN photodiode
d_{apd}	m	depth of multiplication region
d_{ccd}	m	depth of correlating region
d_j	m	junction width
d_{pd}	m	diameter of photodiode
d_{pin}	m	depth of depletion region
d_{lens}	m	lens diameter
e^-	$1.602176 \cdot 10^{-19}$ As	elementary charge
E_g	eV	bandgap energy
E_p	eV	phonon energy
E_{ph}	eV	photon energy
ER	1	extinction ratio
f_1	Hz	fundamental wave

f_{3db}	Hz	bandwidth
f_{max}	Hz	maximum frequency
f_{min}	Hz	minimum frequency
f_{mod}	Hz	modulation frequency
f_{ref}	Hz	reference frequency
f_{sample}	Hz	sampling frequency
G_{eh}	1/ms	electron-hole pair generation rate
g_m	A/V	transconductance
h	$6.626068 \cdot 10^{-34}$ Js	Planck constant
$\hbar$	Js	$h/2\pi$
h^+	As	hole, positive elementary charge
I_{AC}	A	AC current
I_{A1A2}	A	coupling current between DAP anodes
I_{DS0}	A	DC bias current
I_{DSsat}	A	drain to source current of a MOS device
I_{anode1}, I_{anode2}	A	DAP output current
I_{dark}	A	dark current
I_{dd}	A	supply current
I_{out}	A	output current
I_{pd}	A	amplitude of the photocurrent
i_{bg}	A	current from background light
i_{ph}	A	AC photocurrent
k_b	$1.3806503 \cdot 10^{-23}$ J/K	Boltzmann constant
k_c	1	width of confidence intervall
k_{diff}	1	differential gain
k_{gain}	1	inherent gain of a detector
k_p	1	proportional factor
k_{sup}	1	suppression factor
L	m	transistor length
N	1	number of phase steps
N_a	$1/m^3$	acceptor concentration
N_d	$1/m^3$	donator concentration
n	1	number of photons

n_i	$1/m^3$	intrinsic density
n_{max}	1	maximum number of detected photons
$\overline{n}$	1	average photon number within t_{bin}
$\overline{n}_{back}$	1	number of photons of background light
$\overline{n}_{signal}$	1	number of signal photons
P_{opt}	W	optical power
$P_{opt,back}$	W	optical power of background light
$P_{opt,signal}$	W	optical signal power
p_{p}	1	probability of Poison distribution
Q_{inj}	As	injected charge
R	A/W	responsivity
R_{fb}	Ω	feedback resistor
s	m	real object distance
s_d	m	distance range
s_{err}	m	distance measurement error interval
s_{lin}	m	linearity error
$s_{measure}$	m	measured object distance
s_{per}	m	diode perimeter
s_{res}	m	distance measurement resolution
s_{unamb}	m	unambiguous range
Δs_{ref}	m	distance error due to reference clock
T	K	temperature
T_p	s	periodic time
$T_{sampling}$	s	sampling time
t	s	time
t_{bin}	s	time window
t_{delay}	s	time delay
t_{fall}	s	fall time
t_{final}	s	settling time
$t_{measure}$	s	measurement time
t_{off}	s	turn off time
t_{on}	s	turn on time
t_{rise}	s	rise time

t_{sim}	s	simulation time
t_{skew}	s	time skew
t_{step}	s	duration of a single phase-shift step
t_{tof}	s	time-of-flight
V_{anode1}, V_{anode2}	V	DAP anode voltage
V_{bias}	V	bias voltage
V_d	V	built-in voltage
V_{mod}	V	modulation signal
V_{pd}	V	voltage across photodiode
V_{ref}	V	reference signal
V_T	V	threshold voltage
$V_{trigger}$	V	trigger signal
v_p	m/s	velocity of propagation
W	m	transistor width
X_v, X_p	1	Fourier series of x_v, x_p
x_{si}	m	depth from wafer surface
$x_v(t)$, $x_p(t)$	1	periodic signals
Z_{in}	Ω	input impedance
Z_{par}	Ω	parasitic impedance
Z_{pd}	Ω	photodiode impedance
Z_{tot}	Ω	total transimpedance
Φ	rad	aberration angle
α	1/m	absorption coefficient
β	1/m	free range propagation attenuation
ε_0	$8.8541878176 \cdot 10^{-12}$ F/m	permittivity in vacuum
ε_r	1	relative dielectric constant
η_{fill}	%	optical fill-factor
η_{lens}	%	lens efficiency
η_{sen}	V/A	correlation sensitivity
λ	m	wavelength
λ_{max}	m	maximum wavelength
ρ_{ref}	%	reflection coefficient
σ_d	m (%)	distance precision

σ_p^2	1	variance of Poisson distribution
σ_φ	rad	variance of phase
τ	s	time delay
τ_{bc}	s	time constant of bridge-correlator
φ	rad	phase-shift
φ_{pot}	V	potential
φ_{vp}	1	cross-correlation function
ω	1/s	angular frequency
ϑ	°C	temperature

1 Motivation

Today's sensor technology is capable of measuring almost any physical quantity. Depending on the measurement task the number of sensors that are built to solve a dedicated problem strongly varies. For the detection of particles within a particle accelerator only a small number of sensors are built around the world. On the contrary, to receive the infrared signal of a remote control to control a TV set, millions of sensors are being used. The main difference between these two examples is that the detection systems strongly vary in cost and complexity depending on the total number of sensors built.

Recording and processing of three-dimensional (3D) image data is fundamental for many control and supervision tasks. Even simple problems e.g. to recognise if an object is placed within the danger zone of a closing door, before it touches the door itself, demands a highly sophisticated 3D vision system. Other tasks like part recognition or surveillance of an entrance hall would be eased by such a system, as well.

Right now a lack of affordable, easy to use and robust 3D measurement sensors having a high lateral resolution can be seen. High resolution two-dimensional (2D) colour and infrared cameras are available on a grand scale, but no depth information can be recorded by them. Stereo-metric systems need at least two cameras to reconstruct 3D information. This is obviously no compact sensor solution, since the cameras cannot be placed close to each other. The same effect can be seen by the human eyes. They are placed approximately 6.6cm apart. This all passive 3D vision system provides a good depth resolution for close objects, but a poor one for far distant ones e.g. which mountain is closer?

To avoid the use of two sensors placed at different points a 3D distance measurement system has to transmit an active signal. Various signal sources are available right now. They are based on the transmission of ultrasound, microwave or optical signals. The key information of the desired 3D sensor is its high lateral resolution. Therefore it becomes possible to measure the distance of an object point instead of measuring the mean object distance. Thus high focus capability of the transmitting source and the receiving sensor is necessary. In general it can be stated that the shorter the wavelength of the carrier signal is, the better it can be focused onto the receiver. Therefore short optical wavelengths are preferable.

Out of this the detection problem arises. How can we detect the received optical signals? Fast detection of optical signals is solved by transforming the optical signal into a signal proportional current by the use of semiconductor materials. Typical materials used for optical detection are GaAs or Silicon.

Keeping in mind that the system should have a high lateral resolution to distinguish also small objects, it is necessary to place the photodetector elements close to each other. Since the output signal of a fast photodetector is a current, it would be advantageous to process this current already within every pixel.

By far most circuit designs implemented for mass products are done by using the cheap material silicon. Since silicon is capable of detecting light and to integrate a readout circuit on the same chip it is the material of choice.

Out of this the motivation and the demands on the development of a new 3D vision system can be defined. The final system has to fulfil the following criteria. It has to:

- be easy to use
- avoid the use of more than one sensor
- use an active illumination source
- avoid any mechanically moving parts to be robust
- use optical signals to reach a high lateral resolution
- detect fast optical signal
- be built up on a semiconductor material
- integrate the photodetector and the readout circuit on the same chip
- be cost efficient
- use available technology

Therefore the motivation for this thesis was to successfully implement a new 3D vision sensor concept operating on the time-of-flight principle which has to be realised as an opto-electronic integrated circuit (OEIC). Design and fabrication has to be done by using an available and accessible standard silicon technology.

2 Introduction

Distance measurement sensors are of fundamental importance for a wide range of applications. Especially in industrial and automotive environment, mid-range distance sensors operating from short distances in the cm range up to some meters are necessary. Basic tasks like autonomous navigation of a self guided vehicle SGV through a manufacturing hall or supervision of the danger zone of an automatically closing door demand highly sophisticated three-dimensional (3D) distance measurement systems.

Systems for the given range can be based on microwave radar, ultrasonic or optical sensors. The common distance measurement principle is the determination of the time-of-flight (TOF) of a carrier signal from a transmitter to an object and back to a receiver. The distance information s is calculated by (2.1), with the velocity of propagation v_p and the TOF t_{tof}.

$$s = \frac{v_p t_{tof}}{2} \tag{2.1}$$

Mid distance range radar sensors used for automotive applications operate at a typical carrier frequency of 77GHz [1]. This results in a wavelength of $\lambda = 3.9$mm. To reach a sufficiently high lateral resolution for a 3D measurement it is necessary to collimate the aperture angle of a single receiver channel and to use a large number of receiving antennas to form a line or a matrix multi-pixel receiver. The beam angle of a signal is roughly directly proportional to the ratio of wavelength to antenna diameter [2]. Therefore the antenna diameter has to be at least in the range of millimetres for radar receivers [3]. Out of this it is not possible to integrate pixel arrays with high lateral resolution. This drawback does not apply to optical systems operating in a typical wavelength range of $\lambda = 650$nm−1000nm.

Ultrasound sensors transmit a chirp of sound waves ranging from $f_{mod} = 20$kHz−50kHz to determine the distance information. They suffer from the low propagation speed of sound in air of approximately $v_p = 343$m/s. For a $s = 15$m distant target, this results according to (2.1) in a TOF of $t_{tof} = 87$ms neglecting any signal processing time. This is not sufficient for applications requiring a high frame rate. The TOF of light for the same distance is $t_{tof} = 100$ns.

Due to the limitations of radar and ultrasound systems for high-speed 3D measurement systems with high lateral resolution, this thesis will focus on active optical distance measurement systems.

2.1 State-of-the-art of Optical Distance Measurement Systems

Optical 3D measurement systems for the mentioned distance range can be divided into two classes. These are triangulation based systems and TOF systems. Triangulation based systems measure the depth information of a scene due to geometrical relations between the sent and received light signal. TOF systems gather distance information by measuring the travel time of light from the light source to the object and back to the receiver.

A triangulation based system determines the distance of a particular point of a 3D scene by illuminating this point. The distance is mapped onto a position sensitive device (PSD) or a charge coupled device (CCD) line sensor with a picturing lens. A line sensor is realised using a sheet beam for illumination and a 2D CCD camera for readout. By mechanical scanning of the projected sheet beam it is possible to acquire the 3D information with high lateral resolution of the entire scene. A measurement system based on triangulation with VGA resolution of 640×480 pixel is presented in [4], [5]. Frame rates up to 1kfps have been reported for a 375×365 pixel system with a range resolution of 1.1mm for a 600mm distant object [6], [7].

Mechanical scanning has to be avoided for many applications due to cost limitations and robustness of the overall system. An all solid-state 3D sensor therefore has to measure the object distance within every single pixel. This results in the loss of geometrical information of the projected beam. Due to the constant, finite speed of light in air the distance information can be obtained by determining the TOF of the light beam. The use of a receiving lens and arranging of 1D pixels in matrix format, allows the mapping of a direction in space onto the x-y position on the sensor surface [8]. The 3D distance output data is represented in a spherical coordinate system.

Two different approaches are used for TOF measurements. Pulsed runtime systems are operated with low duty cycle, high intense optical pulses. The runtime between sent and received pulse is proportional to the distance. Continuous-wave systems in contrast use an amplitude-modulated light source to illuminate the scene. The receiver correlates the electrical modulation and the optical received signal. The phase-shift between these two signals is also proportional to the distance (2.2).

$$s = \frac{c_0 \varphi}{4\pi f_{mod}} \tag{2.2}$$

The common structure of a TOF system is shown in Figure 2.1. The reference clock oscillator is used to derive all phase stable signals for the TOF measurement. The control unit generates the modulation signal V_{mod} for the light source and all reference signals V_{ref} for the TOF sensor. For continuous-wave systems high power light emitting diodes (LEDs) and for pulsed runtime systems fast laser diodes are in use. An analogue-to-digital converter (ADC) or a time to digital converter (TDC) serves as interface to the digital post processor. Actual distance calculation is performed by the post processor implemented either by a signal processor or directly by a PC.

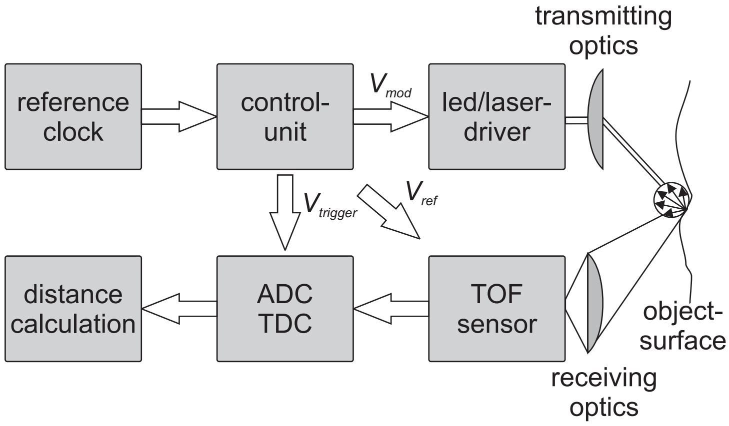

Figure 2.1 Structure of a TOF system

2.1.1 Pulsed Run Time Systems

A single pixel pulsed runtime system with an external avalanche photodiode (APD) and resonance-based pulse shaping is presented in [9], [10]. The receiver channel having a bandwidth of $f_{3db} = 1.6$GHz was fabricated in a 0.35µm BiCMOS SiGe process. It reaches a single-shot precision of $\sigma_d = 3.3$cm for an input signal-to-noise ratio (SNR) of 10. The time measurement is performed using an external TDC [11], [12].

For solid-state 3D TOF systems the use of integrated photodetectors is necessary to reach a sufficiently low pixel pitch. The CMOS 3D imager presented in [13] operates on the pulsed runtime principle. The 4×64 pixel sensor is fabricated in 0.5µm CMOS technology. A time to voltage conversion is performed using the correlated double sampling (CDS) technique. A single distance measurement is based on four measurement cycles with varying integration time windows. The distance information is gained by the ratio of the received energy of the optical pulse within a defined window and the total receivable energy of the pulse.

Suppression of background light is performed by determining the received optical energy for the same time durations without pulses and subtracting these analogue values within the pixel. The division is performed off-chip. The pixel size is $A_{pixel} = 130\times300\mu m^2$. Due to the arrangement of the pixels as a line sensor, an optical fill-factor into one direction of almost $\eta_{fill} = 100\%$ is reached. The peak power of the transmitted optical pulse is $P_{opt} = 70$W for a pulse duration of 30ns and a laser wavelength within $\lambda = 850$nm−910nm. For a distance range up to $s_d = 8$m a resolution better than $s_{res} = 5$cm (1cm) at a frame rate of 19.5kfps (195fps) is reported [14].

A pixel setup including a low-power differential operational transconductance amplifier (OTA) in combination with a standard PN photodiode for TOF systems is introduced in [15], [16]. By adding a dummy photodiode a fully differential pixel layout for a 16×16 pixel array in 0.35µm CMOS technology was realised [17]. The optical fill-factor of the $A_{pixel} = 80\times80\mu m^2$ pixel is $\eta_{fill} = 20\%$. Distance information is obtained by integrating the current caused by the received light pulse during a defined time window. The influence of different object reflectivity is cancelled by repeating the measurement for different windows. Background light suppression is performed by discharging the feedback capacitors of the OTA with charge carriers generated by background illumination during a second acquisition phase. Illumination of the 3D scene is done using a laser source with $P_{opt} = 1W$ and $\lambda = 905nm$. A precision of $\sigma_d = 5\%$ for a cooperative target is reported for a distance range of $s_d = 2m-9m$ at a frame rate of 30fps.

Latest developments of integrated APDs in high voltage CMOS technology [18] led to the development of two-dimensional single photon avalanche diode (SPAD) arrays [19]. A CMOS based SPAD consists of a p^+ anode surrounded by a p-type guard ring to avoid lateral surface break through (Figure 2.2). The cathode is formed by a deep n-well. An n^+ doped ring is used to contact the cathode. By connecting the anode to a negative potential down to -25V it is possible to build up a multiplication region below the p^+ region of the anode.

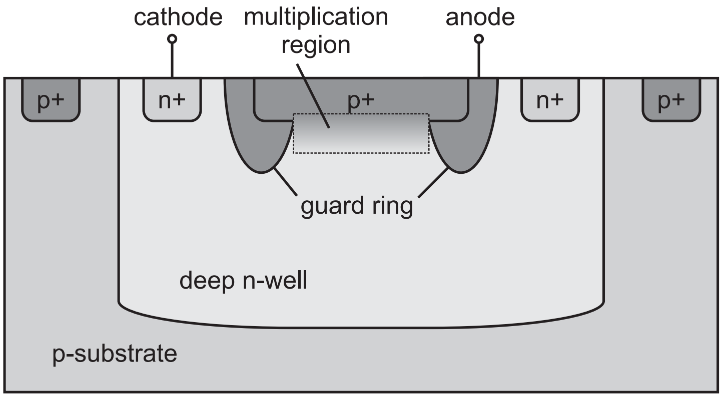

Figure 2.2 Cross section of a CMOS SPAD [15]

Each photon that enters the device and generates an electron-hole pair inside the multiplication region causes an avalanche generation of secondary charges. This results in a built-in current amplification of SPADs compared to other photodetectors. The amplification is limited to a defined value, if the avalanche effect stops without changing of the supply voltage. Therefore the output current is proportional to the power level of the incident light. If the avalanche effect causes more and more secondary charges to be generated, the amplification is infinity. This mode is called Geiger mode. In this case the amplitude of the supply voltage has to be lowered until all charge carriers are swept out of the amplification region to stop the avalanche process, otherwise the remaining charge carriers would trigger a new avalanche. All information about the optical power of the incident light is lost. Photons arriving during a persisting avalanche breakthrough are not recognised.

A 32×32 pixel SPAD receiver for 3D measurements realised in 0.8µm high voltage CMOS technology is used for a pulsed runtime system. The pixel size is 58×58µm² with an optical fill-factor of $\eta_{fill} = 1.1\%$ [20]. The photon detection probability at $\lambda = 635nm$ is 12%. The SPADs are operated in Geiger mode. The output signal of each pixel is digital. The time point of the rising edge of the output signal is directly related to the detection time of the first arriving photon after reset of the SPAD, no matter if the photon dates from the transmitted optical pulse or background illumination. Readout of the chip is performed in sequential way using an external commercial TDC-chip. By physically shifting the entire integrated circuit (IC) horizontally and vertically with piezo-actuators the lateral resolution is enhanced up to 64×64 pixel [21]. The maximum distance range is 3.75m. By averaging 10^4 distance measurements a root mean square (RMS) distance accuracy of 1.3mm is reported for an optical peak power of 250mW.

A SPAD line sensor with 64×1 pixel resolution and in-pixel time to voltage converters (TVCs) is introduced in [22]. The SPADs operated in Geiger mode, are realised in a modified 0.8µm high voltage CMOS technology. The pixel size including the TVC is $A_{pixel} = 38\times180\mu m^2$. Averaging of up to 100 time measurements inside each pixel is possible with the internal implemented TVC. The distance range for a cooperative target is $s_d = 2m-5m$ with a single-frame precision of $\sigma_d = \pm3.75cm$. A 3D image recorded by using a mechanical scanner and a laser peak power of 250W at a wavelength of $\lambda = 905nm$ is shown to demonstrate the 3D capability of future SPAD array realisations.

2.1.2 Continuous-Wave Systems

Continuous-wave systems determine the phase-shift between the amplitude-modulated transmitted signal and the received signal. The modulated light source operates in continuous-wave mode. This results in a maximum useable amplitude $\hat{P}_{opt}$ equal to the mean value $\overline{P}_{opt}$ of the optical signal (2.3).

$$P_{opt}(t) = \overline{P}_{opt} + \hat{P}_{opt}\sin(\omega t) \qquad for\ \overline{P}_{opt} \geq \hat{P}_{opt} \tag{2.3}$$

Due to the low receivable optical power, correlation between the input signal and the original modulation signal is performed. To reconstruct the phase information and to suppress the influence of the object reflectance, frequency or phase modulation of the light source is necessary.

A single pixel frequency modulated continuous-wave (FMCW) system with multi-target capability is presented in [23]. For a distance range of $s_d = 1m-2.4m$ a standard deviation $\sigma_d = 2.6cm$ is reported. The multi-target resolution is 0.5m.

Due to the complex frequency analysis and the high frequency linearity of the receiver channel, necessary for FMCW systems, multi-pixel sensors use phase-shift keying (PSK) methods. Therefore the multi-target capability within a single pixel is lost. The opto-electronic correlation can be performed directly by a correlating photodetector or by a combination of photodiode and correlating readout circuit.

The basic operating principle of a correlating detector relies on the transport of the photogenerated charge carriers to different readout terminals by applying a time dependent lateral electric field to the photo sensitive area. The separation efficiency of such detectors strongly depends on the penetration depth and therefore on the wavelength λ of the incident light. This is due to the fact that charge carriers generated deep in the substrate will not be separated by the electric field at the surface. In general it can be stated that it is difficult to perform an opto-electronic correlation for near infrared light by integrated silicon based detectors, because of the large penetration depth.

A metal-semiconductor-metal (MSM) device as depicted in Figure 2.3 is used as external opto-electronic correlator in [24].

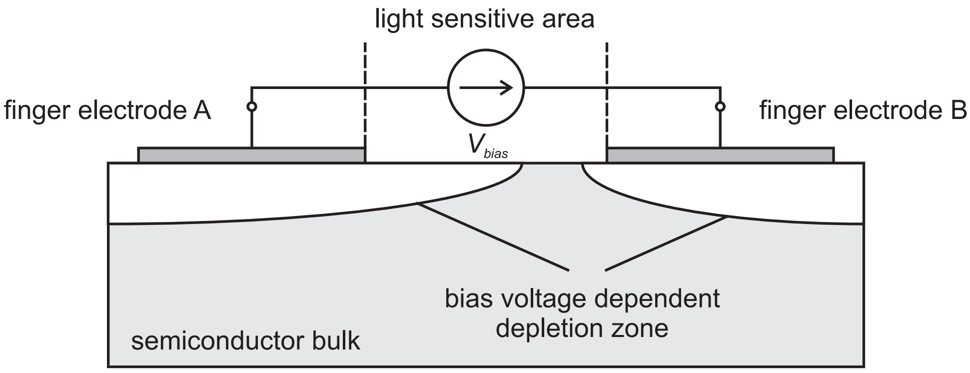

Figure 2.3 Cross section of a GaAs MSM [24]

The metal finger electrodes on the floating GaAs bulk form two schottky barriers. The extension of the depletion zones is controlled by the bias voltage between the electrodes. This results in an opto-electronic mixing effect. The low-frequent output current is proportional to the incident optical power and to the width of the depletion zone. Low-pass filtering has to be performed to suppress the high frequency modulation voltage at the output. The current direction is determined by the sign of the bias voltage.

An optical distance sensor based on MSM technology is presented in [25]. An external MSM diode and PSK modulation with 120 phase steps for a single distance measurement is used. Background light mixed up to the modulation frequency is suppressed by low-pass filtering. For a distance range of $s_d = 0.55\text{m}-0.75\text{m}$ a standard deviation of $\sigma_d = 4.7\text{mm}$ for a highly reflective target and $\sigma_d = 12.13\text{mm}$ for cardboard is reported.

A correlating detector in CMOS technology is the so-called photonic mixer device (PMD). It consists of two modulation gates on an oxide layer and two readout terminals A and B [26]. The transparent poly silicon gates are used to apply an electric field in the p-substrate (Figure 2.4). Photogenerated electron-hole pairs are separated by the vertical field. Therefore the holes flow toward the grounded substrate contact, whereas the electrons are forced either to readout terminal A or B depending on the modulation voltage V_{mod}. This results in a mixing effect. Charge carriers generated by background light contribute equally to A and B. Therefore countermeasures have to be met to suppress background illumination.

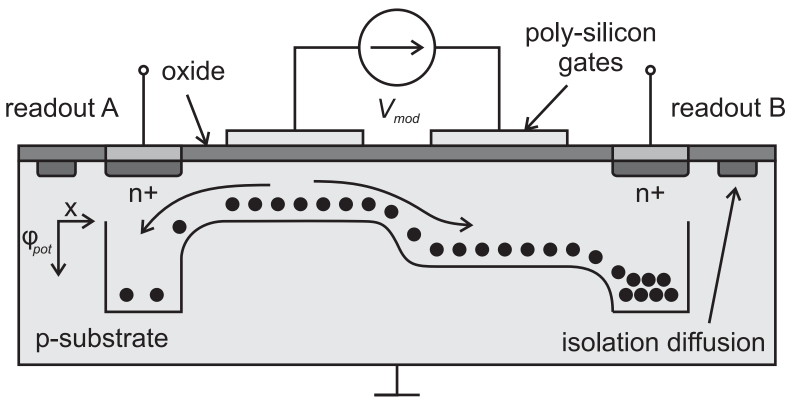

Figure 2.4 Functional principle of a PMD

A 3D camera based on PMD technology with 16×16 pixel and a pixel size of A_{pixel} = 210×150µm² is reported in [27]. The modulation frequency of f_{mod} = 20MHz limits the unambiguous range to s_{unamb} = 7.5m. The sensor is fabricated in 0.6µm CMOS technology. It reaches a standard deviation of σ_d = 35mm for a distance range of s_d = 1.5m−3.5m by using a LED array for illumination. The average optical power transmitted to the object is P_{opt} = 1W at the wavelength λ = 740nm.

A closely related operating principle is used for the CCD/CMOS based 3D sensor presented in [28]. The main difference is the in-pixel charge carrier storage capability due to the introduction of an additional integration gate (Figure 2.5). The pixel is capable of integrating photogenerated charges from several modulation cycles below the gate. Background light is not suppressed by this functional principle therefore an additional control loop has to be added to each pixel [29]. The 124×160 pixel 3D camera realized in 0.8µm CCD/CMOS technology measures distances up to 7.5m at frame rates up to 100fps [30]. 48 sinusoidal modulated LEDs illuminate the scene with an average optical power of P_{opt} = 800mW at a wavelength of λ = 870nm. An optical band pass filter is used to lower the influence of background light. A 176×144 pixel sensor with integrated background light monitoring for distances up to s_d = 6m still uses optical band pass filtering [31].

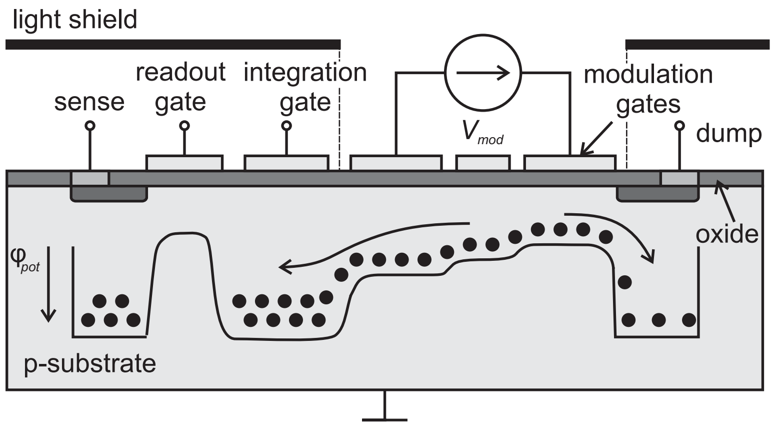

Figure 2.5 CCD/CMOS pixel for TOF measurement with in-pixel storage capability [28]

A time-of-flight sensors with high lateral resolution is presented in [32]. The pixel consists of two pairs of controllable poly gates on a PIN diode structure. One pair is used for correlating photo-generated charges with the modulation voltage, whereas the other pair is used for background light suppression.

The measurement object is illuminated by a pulsed LED array. The pulses have a duty cycle of 10% at f_{mod} = 1MHz. The readout process is divided into two cycles. During the first cycle correlation is performed with the received light pulse, equal to the functionality of the CCD/CMOS sensor. During the second cycle no photons dating from the optical pulse arrive. Therefore all charges generated in this phase are drained by the second pair of electrodes. Using this timing scheme it is possible to reduce the influence of background light down to the fifth part, because the optical peak power of the pulse during active measurement is increased by a factor of five, compared to the pure continuous-wave CCD/CMOS pixel.

The sensor fabricated in 0.35µm CMOS technology features a lateral resolution of 336×252 pixel [33]. The pixel size is $A_{pixel} = 15 \times 15 \mu m^2$. Due to the distance determination algorithm based on the division of only two output voltages good measurement results are only possible for a range of $s_d = 1.5m - 12m$. An optical band pass filter at $\lambda = 870nm$ is used to further suppress background light. The minimal resolution for a reflective board is 2.8cm. The optimal resolution is reached only for equal distribution of received electrons below the modulation gates. This corresponds exactly to the centre of the distance measurement range.

The correlating PIN photodetector pixel presented in [34] is capable of suppressing background light by performing a difference integration of the detector output currents. The pixel fabricated in a modified 0.6µm BiCMOS technology contains a correlating photodetector operating on the PMD principle. The suppression of background light is realized using a current mirror that subtracts the output current of one output terminal from the second output. The difference current containing the distance information is integrated using a capacitor. An optical fill factor of $\eta_{fill} = 24\%$ for this structure is reached. A maximum standard deviation of $\sigma_d = 5cm$ over the entire distance range of $s_d = 0.1m - 15m$ is reported.

An active pixel structure with an integrated PIN photodiode fabricated in a modified 0.6µm BiCMOS process is introduced in [35]. The bandwidth of the PIN photodiode exceeds $f_{3db} = 1.35GHz$. The received input current is amplified by a current pre-amplifier and correlated in a second stage using a switching network and an operational amplifier (OPA) for active integration. The standard deviation is better than $\sigma_d = 2\%$ over the full distance range of $s_d = 0.1m - 3.7m$.

The circuit is improved by substituting the current pre-amplifier by a single-stage transimpedance amplifier [36]. Therefore the sensitivity could be enhanced, resulting in an extended measurement range of $s_d = 0.1m - 15m$ for a diffuse reflecting object. The standard deviation for an optical transmitted power of $P_{opt} = 1.6mW$ is $\sigma_d = 7cm$.

2.2 Outline of the Doctoral Thesis

This doctoral thesis is divided into seven chapters followed by the references used. The content of each chapter will be introduced in brief in this section. Furthermore, a list of figures, a list of tables, a list of abbreviations and a list of symbols used within this thesis are included.

Chapter 1 describes the motivation why cost efficient, robust, all solid-state 3D vision systems are necessary to supervise many automatically controlled tasks occurring in daily life. It points out that an opto-electronic system built in silicon technology can solve these problems.

Chapter 2 shows the state-of-the-art of optical distance measurement systems. Various measurement principles are introduced, including systems operating on a triangulation or a time-of-flight based principle. Time-of-flight based systems are either implemented as pulsed runtime systems or continuous-wave systems. Pulsed runtime systems use fast, amplifying receivers as e.g. avalanche photodiodes or the combination of PIN photodiodes and transimpedance amplifiers to trigger a time measurement unit. Correlation based systems perform a correlation of sent and received signal to retrieve the distance information.

In chapter 3 all fundamentals necessary to design a continuous-wave optical distance measurement system are introduced. The physical conditions regarding time durations to be measured and optical power levels of transmitted and received light are addressed. Furtheron the correlation principle to gain the distance information from the noisy received optical signal is explained. Also the physical limitation of the achievable standard deviation of a single distance measurement dating from photon noise is illustrated.

Chapter 4 describes the operating principle of a fast and effective integrated PIN photodiode provided by the available modified 0.6µm BiCMOS technology. Also an opto-electronic correlating photodetector, the so-called double-anode photodetector, is introduced. It is capable of performing this correlation highly effective at a high-speed.

In chapter 5 a newly developed active high-speed readout circuit is introduced. An integrated PIN photodiode serves as detector element. The readout circuit consists of a pre-amplifier realised by a single-stage transimpedance amplifier, a correlation stage and an active differential low-pass filter. Single distance measurement times of only $t_{measure} = 500\mu s$ have been achieved for distances in the range of $s_d = 0.1m - 3.7m$. An electro-optic measurement setup to verify the distance measurement capability is presented in this chapter.

Chapter 6 deals with all passive readout circuits which are necessary for multi-pixel systems to keep the power consumption of the entire OEIC sufficiently low. The first structure introduced in section 1 consists of a fast PIN photodiode and a bridge-correlator circuit. It is capable of inherently suppressing background light by charging and discharging an integration capacitor within one modulation period. Due to the parasitic photodiode capacitance the circuit saturates and therefore the sensitivity is limited. A detailed model for this behaviour is derived. The distance measurement range of the sensor is $s_d = 0.1\text{m}-3.7\text{m}$. For a redesigned OEIC a single distance measurement time of $t_{measure} = 2\text{ms}$ is reached. Section 2 introduces a modified bridge-correlator circuit which includes an active amplifier within every pixel. Therefore the pixel is not all-passive anymore but the sensitivity is enhanced by at least a factor of 30. For a distance measurement range of $s_d = 0.7\text{m}-3.4\text{m}$ a maximum standard deviation of $\sigma_d = 1.4\text{cm}$ is reached for an optical transmitted power of $P_{opt} = 1\text{mW}$ without any adjustment of the optical setup.

The third section of chapter 6 shows again an all passive readout circuit based on diode-connected MOS transistors. The DC current fed to the active transimpedance stage is provided by the integrated double-anode photodetector which performs an opto-electronic correlation. Due to high transimpedance and low noise level at the same time the DAP based sensor is very sensitive. Therefore a large distance measurement range of $s_d = 0.1\text{m}-15\text{m}$ is reached. The single distance measurement time is $t_{measure} = 5\text{ms}$ and the maximum linearity error is $s_{lin} = \pm 0.23\%$.

Chapter 7 summarises the content of this thesis. A brief design guide for optical distance measurement systems operating on the time-of-flight principle is given. The measurement results of the three different sensor concepts are highlighted. Finally a detailed data table is provided to compare the measurement results of the newly developed opto-electronic correlation receivers with the ones of the current state-of-the-art systems.

3 Fundamentals of Optical Distance Measurement Systems

The idea to determine an object's distance by measuring the time-of-flight of light from the source to the object and back to the receiver leads to a set of basic conditions that will be treated in this chapter. Limiting factors are the maximum transmittable optical power as well as the short time durations to be measured. Correlation methods will be introduced for distance determination. The relevant characteristics of the correlation principle used for the newly developed pixel structures will be highlighted. The minimum achievable standard deviation for optical TOF systems is determined to estimate the effectiveness of different receiver concepts.

3.1 Physical Conditions

In contrast to 3D stereo systems, TOF systems rely on modulated active illumination to gain distance information of the object. Due to power consumptions and eye safety reasons the maximum optical power is limited to the mW range for a single pixel. High demand on stability in terms of additional phase-shift introduced by the illumination module is given to ensure high distance measurement accuracy.

3.1.1 Optical Power Budget

Aim of continuous-wave systems is to measure 3D information of the surrounding environment. A typical 3D scene consists of objects of different material. Therefore strongly varying surface reflectivity occurs. As shown in Figure 3.1 four main types of reflection have to be distinguished for TOF systems.

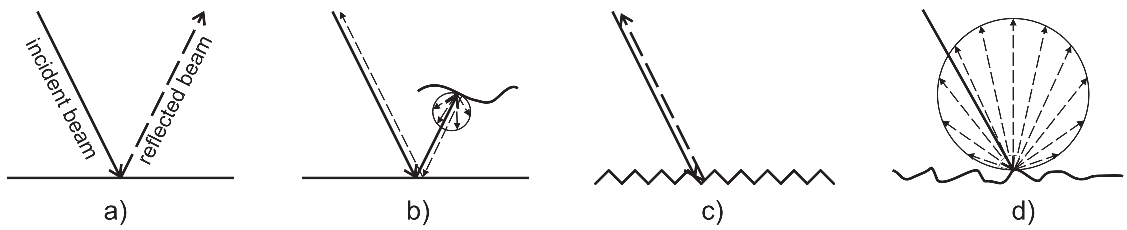

Figure 3.1 Types of reflection: a) total away, b) secondary, c) retro and d) diffuse reflection

Total away reflection occurs when the transmitted beam is reflected by a mirror into free-space. If the reflected beam hits an object, secondary reflection may occur and a portion of the secondary reflected light will be focused via the mirror back into the receiver. In this case the TOF system measures the distance from the transmitter to the mirror and furtheron the distance from the mirror to the object.

A retro reflector often also denoted as cooperative target reflects the incident light back to the illumination source, this results in very high optical power levels for the TOF receiver. Cooperative targets like triple or corner cube mirrors are often used for long distance TOF measurements e.g. for land surveying to enhance the SNR. In daily live retro reflectors occur as e.g. traffic signs, road markings or license plates.

Unstructured rough surfaces reflect the incident light beam omni-directionally according to Lambert's cosine law. This property applies to most surfaces occurring in nature and is fully described by the reflection coefficient ρ_{ref}. The reflection coefficient is defined as the ratio of reflected optical power $P_{opt,ref}$ to total incident optical power $P_{opt,tot}$ (3.1). The power difference $P_{opt,abs}$ is absorbed by the object. In Table 3.1 reflection coefficients of different materials can be seen. For materials occurring in daily live they range from $\rho_{ref} = 10\%-100\%$.

$$\rho_{ref} = \frac{P_{opt,ref}}{P_{opt,tot}} = 1 - \frac{P_{opt,abs}}{P_{opt,tot}} \tag{3.1}$$

Material	Reflectivity ρ_{ref}
White paper	up to 100%
Snow	80-90%
Beer foam	88%
Newspaper with print	69%
Beach sands	typ. 50%
Rough wood pallet (clean)	25%
Black neoprene	5%
Black rubber tire wall (clean)	2%

Table 3.1 Reflection coefficients for different materials [37]

The receivable optical power $P_{opt,rec}$ of a sensor is determined by the radar equation (3.2) with the transmitted optical power $P_{opt,tra}$, the free range propagation attenuation β, the reflection coefficient ρ_{ref}, the aberration angle Φ, the receiving lens area A_{lens} and the efficiency of the receiving optics η_{lens}. Due to the short measurement distances, the term for free range propagation attenuation for visible and near infrared wavelengths ($\beta \approx 0.02$dB/km) can be neglected [38].

$$P_{opt,rec} = P_{opt,tra} e^{-2\beta s} \cdot \frac{A_{lens} \eta_{lens} \rho_{ref} \cos(\Phi)}{s^2 \pi} \qquad for \ d_{lens} \ll s \tag{3.2}$$

By assuming an optical transmitted power of $P_{opt,tra} = 1$mW, a one inch receiving lens, an aberration angle of $\Phi = 0°$ and a lens efficiency of $\eta_{lens} = 70\%$, it is possible to estimate the receivable optical power of a TOF distance measurement system in a typical environment. From the estimation results shown in Figure 3.2 it can be seen that the minimum expected optical power for distances up to $s = 15$m ranges from $P_{opt,rec} = 50$pW−0.5nW depending on the object reflectivity. The results are valid for object distances much larger than the lens diameter and full coverage of the illuminated object area within the sensors field of view. For short distances $P_{opt,rec}$ remains constant or even decreases with decreasing object distance [39].

For continuous-wave TOF systems also the extinction ratio ER of the amplitude-modulated optical signal has to be considered. The extinction ratio ER of an optical signal is defined as ratio of maximum and minimum optical power level (3.3). The extinction ratio is always positive since no negative optical power exists. It ranges from 1 for an un-modulated up to ∞ for a fully modulated signal.

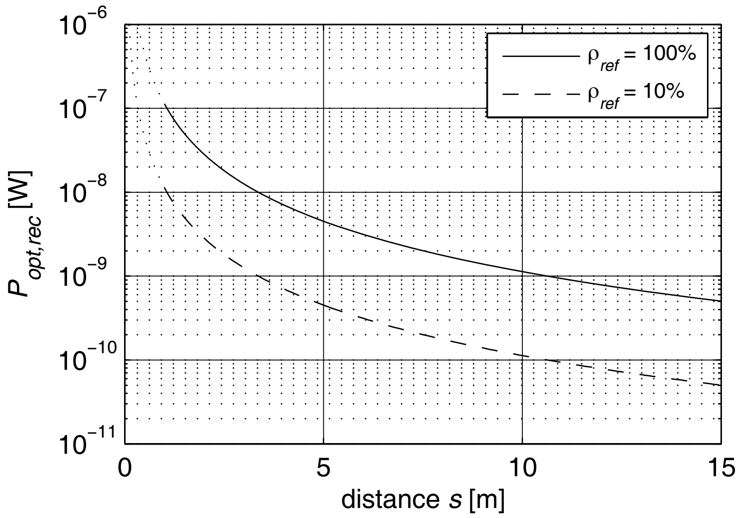

Figure 3.2 Minimum and maximum receivable optical power of an optical TOF system for $P_{opt,tra}$ = 1mW, one inch receiving lens, Φ = 0° and η_{lens} = 0.7

$$ER = \frac{\max\left(P_{opt}\right)}{\min\left(P_{opt}\right)} \tag{3.3}$$

Values of ER less than ∞ result in a decreased useable amplitude of the received signal, as well as an inherently existing and signal power proportional background illumination. Fast optical sources like e.g. laser diodes often require a minimum power level in the low state to reach sufficient low rise and fall times and to avoid any overshoot of the optical output signal. Sinusoidal modulated LEDs are also often operated with $\hat{P}_{opt} < \overline{P}_{opt}$ to avoid clipping of the negative half-wave.

3.1.2 Timing Resolution

The time duration to be measured for a certain distance is determined by (2.1). The constant speed of light is used to map the mid-range distances to short measurable time intervals. The runtime of light for an s = 1.5m distant object is t_{tof} = 10ns. To be able reach a measurement resolution of Δs = 1cm time intervals of Δt_{tof} = 66ps have to be resolved. Direct time measurements e.g. used for pulsed runtime systems require fast, power consuming electronic receiver channels. To relax the demand on the receiving electronics in terms of speed or bandwidth another transformation from the time to the phase domain is done by modulating the light source at a fixed frequency f_{mod} (2.2). The modulation frequency has to be chosen sufficiently low to cover the desired distance measurement range. This results from the property of periodic signals that the phase-shifts of two signals can only be determined unambiguously within a phase range of 2π. The unambiguous distance range is therefore given by (3.4).

$$s_{unamb} = \frac{c_0}{2 f_{mod}} = \frac{\lambda}{2} \tag{3.4}$$

Furtheron the modulation frequency has to be as high as possible to reach maximum phase sensitivity defined by $2\pi/s_{unamb}$ to minimize the standard deviation σ_d of the overall measurement system.

3.2 Correlation Principle

The distance information represented by the phase-shift between sent and received signal can be reconstructed by measuring the cross-correlation function φ_{vp} over the entire phase range (3.5). The modulation signal $V_{mod}(t)$ is of square-wave type with the periodic time T_p (3.6). Depending on the receiver structure the modulation signal has to be inserted as bipolar (1,-1) or uni-polar (1,0) signal into eq. (3.5). The received optical signal $P_{opt}(t)$ is of bandwidth limited square-wave or sinusoidal type. Solving (3.5) for a bipolar modulation signal V_{mod} shows that a DC value of P_{opt} e.g. caused by background illumination is inherently suppressed by the receiver, whereas a uni-polar modulation signal results in an offset of $\varphi_{vp} \sim P_{opt}/2$.

$$\varphi_{vp}\left(t+t_{tof}\right) = V_{mod}\left(t\right) \otimes P_{opt}\left(t+t_{tof}\right) = \int_{-T_p/2}^{T_p/2} V_{mod}\left(\tau\right) P_{opt}\left(t+t_{tof}+\tau\right) d\tau \qquad (3.5)$$

$$\begin{aligned} &V_{mod}\left(t+T_p\right) = V_{mod}\left(t\right) && for -\infty < t < \infty \\ &V_{mod}\left(t\right) = \begin{cases} 1 & for\ \ 0 \le t < \dfrac{T_p}{2} \\ -1\left(0\right) & for\ \ \dfrac{T}{2} \le t < T_p \end{cases} \end{aligned} \qquad (3.6)$$

From the simulations shown in Figure 3.3 it can be seen that the cross-correlation function of a bipolar signal $V_{mod}(t)$ and an ideal (first order bandwidth $f_{3db} = 1\text{GHz}$) square-wave signal $P_{opt}(t)$ of $f_{mod} = 10\text{MHz}$ is a triangle function with the amplitude 1, whereas φ_{vp} of the non-filtered sinusoidal signal results in a pure sinusoidal signal.

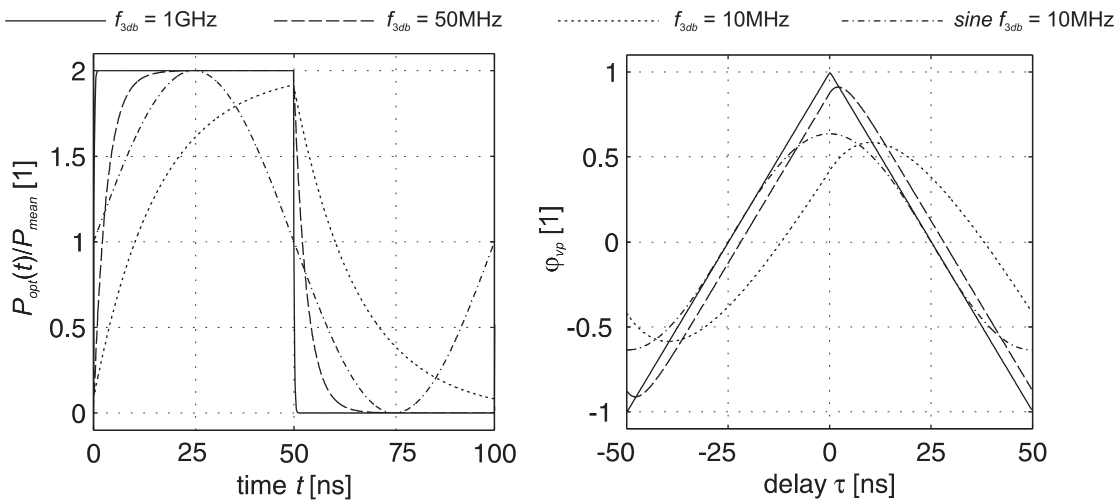

Figure 3.3 Bandwidth limited signals $P_{opt}(t)$ (left) and resulting correlation functions φ_{vp} (right)

The cross correlation functions φ_{vp} of the bandwidth limited signals $P_{opt}(t)$ approximate the sinusoidal one. Beside the decrease of the amplitude also an additional time delay τ occurs for decreasing bandwidth. The smaller amplitude corresponds to a lower demodulation contrast and therefore a reduced SNR. The additional bandwidth depending time delay τ directly results in a longer measured distance.

For bandwidth limited receivers and detectors it has therefore to be kept in mind that every variation of the bandwidth e.g. caused by a change of temperature or supply voltage, results in a varying additional time delay. The resulting distance measurement error is non-correctable. This applies especially to detectors operated close to their cut-off frequency. To be able to deal with this problem the bandwidth has either to be stable over the entire operating range or to be sufficiently high.

The phase-shift dating from the TOF leads to a shift of the cross-correlation function along the delay axis. By using the transformation (3.7) the time delay can also be expressed by the phase φ.

$$\varphi = 2\pi f_{mod}\tau \tag{3.7}$$

The situation for two different distant objects is shown in Figure 3.4. The resulting signals φ_{vp} differ in amplitude and phase. The smaller amplitude of P_{opt} for distance 2 dates from the larger distance or from a lower reflectivity ρ_{ref} of the object 2 as stated by (3.2). Therefore no absolute distance information is included in the amplitude. For a constant noise floor of the sensor the SNR only depends on the amplitude, thus enabling the estimation of the standard deviation σ_d of the actual distance measurement. The absolute distance information is gained by determining the position of the maximum of φ_{vp} using a least square algorithm or by directly calculating the phase-shift using the Fourier transform.

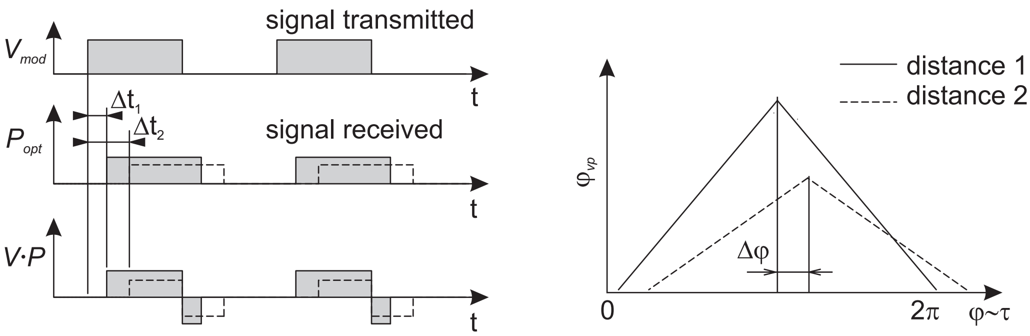

Figure 3.4 Phase-shift of cross-correlation function for two different distant objects

The cross-correlation function can be measured by phase-shifting the modulation voltage of the receiving sensor electronically, related to the modulation signal of the transmitter. A discrete correlation function is obtained by stepping the additional phase in equidistant phase steps. Due to the large availability of high-speed digital programmable devices it is very common to choose the number of phase steps N according to (3.8).

$$N = 2^k \quad for\, k \in \mathbb{N}, k \geq 2 \tag{3.8}$$

To fully determine a sinusoidal function with unknown amplitude, phase and frequency or a triangle function with unknown slope, phase and frequency at least 3 points have to be measured. This results in a minimal value of $N = 4$ for equidistant sampling.

The sampled discrete correlation functions of the two objects mentioned before are depicted in Figure 3.5 for $N = 16$ phase steps. Two substantially different approaches for phase recovery are indicated. The first approach for phase recovery based on a least square error algorithm relies on optimal fitting of two straight lines to the measured values (Figure 3.5a). The second one determines the Fourier coefficient of the fundamental wave by performing an N-point discrete Fourier transform (DFT) on the given data set (Figure 3.5b).

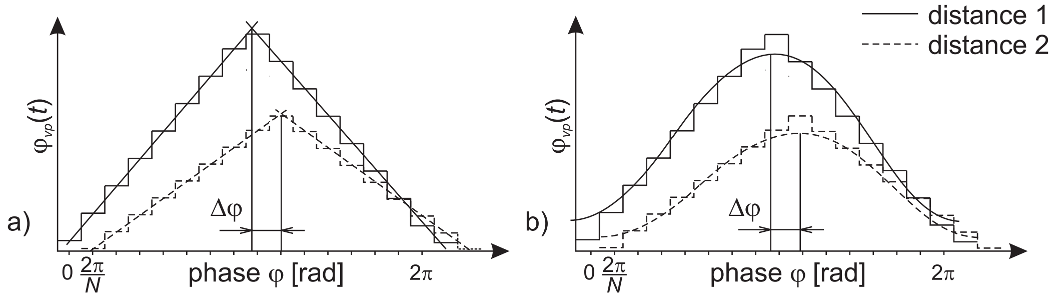

Figure 3.5 Discrete cross-correlation function: a) least square fitting b) DFT algorithm

3.2.1 Least Square Fitting

For the least square algorithm two straight lines described by (3.9) are fitted to the N points of the discrete correlation function in an optimal manner. The phase-shift is determined by the intersection point of the two lines.

$$\begin{aligned} y_1 &= kx + d_1 \\ y_2 &= -kx + d_2 \end{aligned} \tag{3.9}$$

There are two main problems concerning this method. These are the limited bandwidth of every signal and the decision process how to decide if a sample point belongs to line 1 or line 2. If the bandwidth of the input signal is infinite this method delivers the exact value for the phase-shift $\Delta\varphi$. Due to the limited bandwidth of every system the correlation function is not an ideal triangle function. In detail the triangle function will be smoothened. Therefore a bandwidth limited function is approximated by an ideal non bandwidth limited triangle function, resulting in non-perfect phase estimation.

The second problem concerns the decision process if a sample points belongs to one or the other line. For noiseless signals a mathematical solution can be found to solve this problem. If the sampling points are covered with noise more or less a trial and error algorithm has to be used to find the optimal fit by a least square mean. The algorithm implemented operates in the following way.

From the triangle correlation function N equidistant samples are taken. The first trial uses the points $1-N/2$ for the first line and $(N/2+1)-N$ for the second line. Then the least square operation is performed on this data set. Outputs of the least square estimation are the optimal slope and the two ordinate offsets for the minimal square error and the remaining fitting error. The second trial uses the points 2−(N/2+1) for the first line and (N/2+2)−N plus data point number 1 for the second line. Again the remaining error is calculated. After performing this operation N times, the data set with the minimum error is chosen for actual phase calculation. For this optimal data set the intersection point of the two lines is calculated.

For bandwidth limited signals e.g. the 50MHz signal shown in Figure 3.3 it turned out that the measurement results can be improved by omitting the minimum and the maximum value of φ_{vp}. This is due to the fact that the nonlinearity occurring at the smoothed peak of the triangle function causes a large remaining error for the least square estimation. On the other hand omitting measured values is equal to a loss of information and decreases the SNR of the measurement. The algorithm turned out to be not very robust for noisy signals and therefore no further investigations will be made on the least square approach.

3.2.2 Discrete Fourier Transform Fitting

The determination of the TOF by directly calculating the phase-shift of the fundamental wave is in contrast to the least square estimation, exact, if and only if the highest frequency component of the correlation function is lower than half the sampling frequency. Otherwise aliasing phenomena occur. The resulting aliasing error is deterministic and can be corrected to a large extent.

The DFT performs the frequency decomposition of a periodic signal based on a data set of N uniformly-spaced sampling points x_n into the Fourier components X_k contained in the signal. The coefficients of the DFT are given by (3.10). In the case of phase recovery of a sampled signal the data values x_n are of real type. This results in a discrete spectrum that is symmetrical around $k = N/2$. The mean value of the signal is determined by X_0. The minimum resolvable frequency f_{min} of X_1 is (3.11) with the sampling time $T_{sampling}$. The maximum frequency f_{max} is (3.12) and relates to $X_{N/2-1}$.

$$X_k = \sum_{n=0}^{N-1} x_n e^{-\frac{j2\pi nk}{N}} \quad for\ k = 0,1,\cdots,N-1 \tag{3.10}$$

$$f_1 = f_{min} = \frac{1}{T_{sampling} N} \tag{3.11}$$

$$f_{max} = \frac{N/2-1}{T_{sampling} N} \tag{3.12}$$

Sampling of the cross-correlation functions is done by shifting the modulation voltage V_{mod} of the distance measurement sensor electronically in discrete steps. The original triangle function dates from continuous phase-shifting of the optical signal P_{opt} by varying the object distance. From the property of Fourier series for periodic signals (3.13) it can be seen that the k-frequency component of φ_{vp} only exists if $|X_v(jkf_1)|$ and $|X_p(jkf_1)|$ are different from zero.

$$\varphi_{vp}(\tau) = V_{mod}(\tau) \otimes P_{opt}(\tau) \circ\!\!-\!\!\bullet\ X_v^*(jkf_1)\, X_p(jkf_1) \tag{3.13}$$

The modulation voltage V_{mod} is of square-wave type. The discrete Fourier series of the square-wave (3.14) contains only odd numbered harmonics. The signal is not bandwidth limited, therefore an infinite number of harmonics exists. The amplitude is inversely proportional to the order of the harmonics.

$$X_{v,k} = \frac{1}{T}\int_0^T V_{mod}(t)\, e^{-j2\pi k f_1 t}\, dt = \frac{1-(-1)^k}{j2\pi k} \qquad for\ k \in \mathbb{Z} \tag{3.14}$$

The bandwidth limited received signal P_{opt} contains the same frequency components with different amplitudes. In detail the higher harmonics above the signal bandwidth f_{3db} are attenuated. Due to (3.13) also the bandwidth of the cross-correlation function is determined by the bandwidth of the received signal. To avoid aliasing effects either the signal bandwidth or the sampling time has to be sufficient low.

As stated before, the sampling time for the correlation function is simply decreased by increasing the number of phase steps N. On the one hand choosing the number of phase steps sufficiently high ensures that aliasing is completely avoided. On the other hand also the total measurement time $t_{measure}$ and the computational effort for a single distance measurement increase. To be able to determine the optimum number of phase steps N, the maximum resulting error for the worst case of two ideal square-wave signals will be quantified.

The Fourier coefficients of the triangle function are (3.15). The exponential term corresponds to the time shift dating from the TOF between sent and received signal. The spectrum of the cross-correlation functions is periodically repeated in the frequency domain at multiple frequencies of $f_{sample} = Nf_1$ because of the discrete sampling process. The situation for $N = 8$ is shown in Figure 3.6.

$$X_{vp,k} = X_{v,k}^{*} X_{p,k} = \frac{1-(-1)^k}{-j2\pi k}\frac{1-(-1)^k}{j2\pi k} e^{-j2\pi k f_1 t_{tof}} = \frac{1-(-1)^k}{2\pi^2 k^2} e^{-j2\pi k f_1 t_{tof}} \qquad for\ k \in \mathbb{Z} \tag{3.15}$$

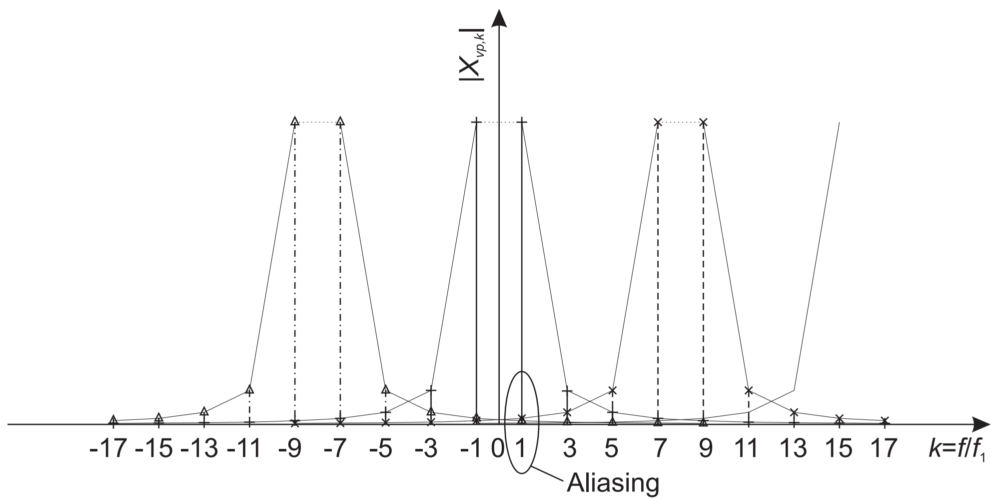

Figure 3.6 Aliasing effect due to under-sampling of non bandwidth limited signals

When aliasing occurs the phase of the infinite sum $X_{vp,k,res}$ (3.16) is determined instead of the phase of $X_{vp,k}$. The distance information is now gained by calculating the phase φ_{res} of the fundamental wave $X_{vp,1,res}$ (3.17). From (3.18) it can be seen that the remaining linearity error is inversely proportional to the modulation frequency.

$$X_{vp,k,res} = \sum_{l=-\infty}^{\infty} X_{vp,lN+k} \qquad for\ 0 \le k < N \tag{3.16}$$

$$\varphi_{res} = \arg\left(X_{vp,1,res}\right) = \arg\left(\sum_{l=-\infty}^{\infty} \frac{1}{\pi^2 \left(lN+1\right)^2} e^{-j2\pi(lN+1)f_1 t_{tof}}\right) \tag{3.17}$$

$$s_{lin} = s - s_{res} = \frac{c_0 \left(\arg\left(X_{vp,1}\right) - \arg\left(X_{vp,1,res}\right)\right)}{4\pi f_1} = \frac{c_0 \left(\varphi - \varphi_{res}\right)}{4\pi f_1} \tag{3.18}$$

Detailed analysis of (3.18) pointed out that the maximum error mainly depends on the modulation frequency $f_{mod} = f_1$ and on the number of phase steps N. For f_{mod} = 10MHz simulations have been performed to investigate the properties of the DFT on filtered and unfiltered signals (Figure 3.7). The filter bandwidth is f_{3db}=50MHz. The order of the filter was varied. For the unfiltered signal the maximum error decreases by a factor of eight by doubling the number of phase steps N. To reach a maximum error smaller than s_{lin} = 2.4mm N has to be at least N = 16. Filtering of the received signal further decreases the error. Since the fundamental wave should not be attenuated by the filter, f_{3db} has to be larger than f_{mod}. To reach a significant improvement by filtering, the filter order has to be at least two, resulting in an error of s_{lin} = 0.7mm for N = 16 phase steps and f_{3dB} = 50MHz.

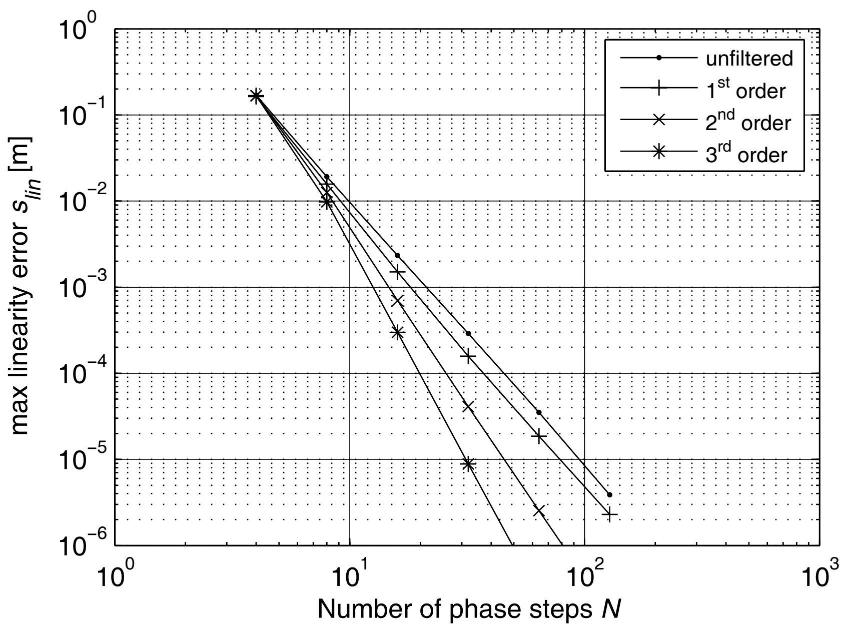

Figure 3.7 Remaining systematic linearity error for DFT phase recovery, f_{mod} = 10MHz, f_{3dB} = 50MHz

From a theoretical point of view the systematic error can be completely eliminated, by using a sinusoidal modulated illumination source. In practice it is difficult to generate an optical sine-wave signal without higher harmonics because of the non-perfectly linear interrelation between large-signal modulation current and optical output power P_{opt} of LEDs and laser diodes. Furtheron it is difficult to phase-shift an analogue signal in discrete phase steps. Digital phase-shifting is easy to implement by a counter based clock divider. Approximating a sinusoidal input signal by using slow, low-pass filtering optical sources e.g. LEDs and choosing the number of phase steps N higher than 4 should result in an optimum result.

Apart from the systematic error introduced by the fast Fourier transform (FFT) algorithm also the influence of noise has to be considered. For an integrated circuit two different types of noise sources are dominant. These are low-frequency 1/f noise or constant frequent background light e.g. neon light and higher frequent thermal white noise.

Preamplifier input stages based on CMOS transistors add low-frequency $1/f$ noise components to the received signal. Also slowly varying background light can be interpreted as low-frequent noise. By correlating 1/f noise using a bipolar modulation scheme, 1/f noise is transformed up to the modulation frequency and can therefore easily be filtered away.

By using an uni-polar modulation scheme, 1/f noise is not suppressed. In this case, DC background light raises the entire correlation function as was stated in chapter 3.2. Low-frequency noise has to be treated in the same way. This results in an output correlation function which is covered by low-frequent noise. Depending on the amplitude of the noise component this causes an unpredictable additional phase-shift. The suppression of low-frequency noise can be improved by measuring more than one correlation function during the measurement time $t_{measure}$ in a sequential way.

High-frequency thermal noise dating e.g. from the feedback resistor of a transimpedance amplifier (TIA) cannot be distinguished from the original input signal. Therefore it is transformed into the baseband and appears at the measurement output as low-frequency distortion signal independent of the chosen modulation process. Since the distortion is of the same frequency as the correlation function it cannot be filtered away. The only way to improve the measurement is to increase the measurement time $t_{measure}$ or the received optical power P_{opt}. Circuit components adding noise to a large extent at the modulation frequency f_{mod} prior to the correlation process should be avoided at all.

3.3 Photon Noise

The fundamental physical lower boundary of the measurement accuracy of optical TOF systems is determined by the photon noise of the received light. Due to the wave-particle dualism the properties of light are described by an electromagnetic wave or an particle beam depending on the actual problem. The detectors of TOF systems implemented as semiconductor photodiodes use an impinging photon to bring one or more electrons from the valence band (VB) to the conduction band (CB) if the energy of the photon E_{ph} is larger than the bandgap energy E_g. Therefore the received light is treated as a particle beam. Photon noise is an amplitude discrete random process. The optical properties of the laser source used are described by the Poisson distribution (3.19). p_p denotes the probability that n photons arrive during the time window t_{bin} for an average optical photon flux of $P_{opt}/\hbar\omega$ (3.20) [8].

$$p_\mathrm{p}\left(n\right)=\frac{1}{n!}\overline{n}^{n}e^{-n} \tag{3.19}$$

$$\overline{n}=\frac{P_{opt}}{\hbar\omega}t_{bin} \tag{3.20}$$

The variance of the Poison distribution σ_p^2 is proportional to the average number of photons within t_{bin} (3.21). The SNR given by (3.22) is also equal to $\overline{n}$. Therefore the SNR can directly be increased by increasing $\overline{n}$ due to a higher optical power P_{opt} or a longer time window t_{bin}. The improvement of the SNR due to higher P_{opt} is obvious because a larger number of photons is available for a given distance measurement time $t_{measure}$. Increasing t_{bin} only increases the SNR for each measurement bin. For a fixed measurement time $t_{measure}$ the number of bins decreases. The influence of the bin number on the overall performance will be investigated later on.

$$\sigma_\mathrm{p}^2=\sum_n p_\mathrm{p}\left(n\right)\left(n-\overline{n}\right)^2=\overline{n} \tag{3.21}$$

$$SNR_\mathrm{p}=\frac{\overline{n}^2}{\sigma_\mathrm{p}^2}=\overline{n} \tag{3.22}$$

Three realisations of optical square-wave signals based on Poison distribution as they are used for further simulations are shown in Figure 3.8. The ideal square-wave signals are all of the same type. The extinction ratio is $ER = 10$, the wavelength is $\lambda = 650$nm and the modulation frequency is $f_{mod} = 10$MHz. A time delay of $t_{delay} = 10$ns is added to the signal. The left and the middle figure represent the same square-wave having a mean optical power of $P_{opt} = 1$nW. The first one is divided into 32 measurement bins whereas the second one consists of 8 measurement bins. According to (3.22) the SNR of the second realisation is 4 times higher. The third realisation shows the same signal with 32 bins but with higher optical power of $P_{opt} = 1$mW. It can clearly be seen that the SNR of this signal is higher. In detail it is exactly 1000000 of the first realisation.

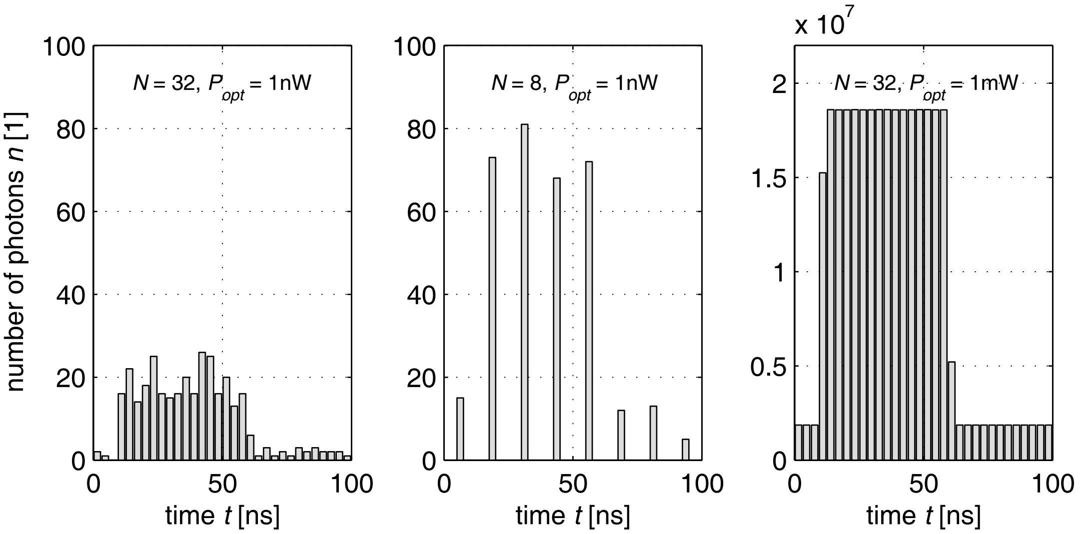

Figure 3.8 Realisation of square-wave signals for simulations: f_{mod} = 10MHz, λ = 650nm, *ER* = 10, t_{delay} = 10ns

The actual phase φ is according to (3.10) given by (3.23). The photon noise based minimal standard deviation can now be calculated, due to the mathematically defined variance of the Poisson distribution.

$$\varphi = \arg\left(X_1\right) = \arctan\left(\frac{\mathrm{Im}\left(X_1\right)}{\mathrm{Re}\left(X_1\right)}\right) = \arctan\left(\frac{\mathrm{Im}\left(x_1 + x_2 e^{-j\frac{2\pi}{N}} + x_3 e^{-j\frac{2\pi 2}{N}} + .. + x_N e^{-j\frac{2\pi(N-1)}{N}}\right)}{\mathrm{Re}\left(x_1 + x_2 e^{-j\frac{2\pi}{N}} + x_3 e^{-j\frac{2\pi 2}{N}} + .. + x_N e^{-j\frac{2\pi(N-1)}{N}}\right)}\right) \tag{3.23}$$

The variance of the phase σ_φ is given by (3.24) by using the formula of error propagation. The derivative terms are calculated after a few conversions to (3.25). With the substitutions $\mathrm{Re}(e^{j\varphi}) = \cos(\varphi)$, $\mathrm{Im}(e^{j\varphi}) = \sin(\varphi)$, $\sin(\varphi) = -\sin(\varphi)$ and the rotation matrix of a complex number (3.26) the terms can be simplified to (3.27).

$$\sigma_\varphi = \sqrt{\sum_{i=1}^{N}\left(\frac{\partial\varphi\left(x_1, x_2, .., x_N\right)}{\partial x_i}\right)^2 \sigma_i^2} \tag{3.24}$$

$$\frac{\partial\varphi}{\partial x_i} = \frac{\mathrm{Im}\left(e^{-j\frac{2\pi(i-1)}{N}}\right)\mathrm{Re}\left(X_1\right) - \mathrm{Re}\left(e^{-j\frac{2\pi(i-1)}{N}}\right)\mathrm{Im}\left(X_1\right)}{\left(1 + \left(\frac{\mathrm{Im}\left(X_1\right)}{\mathrm{Re}\left(X_1\right)}\right)^2\right)\cdot\mathrm{Re}\left(X_1\right)^2} \tag{3.25}$$

$$e^{-j\varphi}X_1 = \begin{pmatrix}\cos(-\varphi) & -\sin(-\varphi)\\ \sin(-\varphi) & \cos(-\varphi)\end{pmatrix}\begin{pmatrix}\mathrm{Re}\left(X_1\right)\\ \mathrm{Im}\left(X_1\right)\end{pmatrix} = \begin{pmatrix}\cos(-\varphi)\mathrm{Re}\left(X_1\right) - \sin(-\varphi)\mathrm{Im}\left(X_1\right)\\ \sin(-\varphi)\mathrm{Re}\left(X_1\right) + \cos(-\varphi)\mathrm{Im}\left(X_1\right)\end{pmatrix} \tag{3.26}$$

$$\frac{\partial\varphi}{\partial x_i} = \frac{-\mathrm{Im}\left(e^{j\frac{2\pi(i-1)}{N}} X_1\right)}{\left|X_1\right|^2} \tag{3.27}$$

The resulting minimum standard deviation based on photon noise for an arbitrary input signal can now be rewritten as (3.28).

$$\sigma_d = \frac{c_0 \sigma_\varphi}{4\pi f_{mod}} = \frac{c_0}{4\pi f_{mod}} \sqrt{\sum_{i=1}^{N} \left(\frac{-\mathrm{Im}\left(e^{j2\pi(i-1)/N} X_1\right)}{\left|X_1\right|^2} \right)^2 \sigma_i^2} \tag{3.28}$$

Depending on the realisation of the modulation process two different cases have to be distinguished. The modulation can either be uni-polar or bipolar as stated in (3.6). For the uni-polar case only 50% of the periodic time T_p photogenerated charge carriers are processed, whereas during the remaining time, the charge carriers are dumped. Therefore background light is integrated and raises the mean level of the entire correlation function. In this case the value σ_i^2 is equal to x_i. In the bipolar case all photons are processed. Background light is subtracted during second half period. Thus resulting in a zero mean correlation function. The value of σ_i^2 has to be equal to the total number of photons dating from the received optical power for all σ_i^2.

From Figure 3.8 it can be seen that the standard deviation of the Poisson distribution depends on the number of measurement bins. For correlation based TOF systems this corresponds to the number of phase steps N chosen for a single distance measurement. In Figure 3.9 the standard deviation depending on N was calculated for uni-polar and bipolar modulation processes using (3.28). It is clearly shown that the number of phase steps has almost no influence on the resulting standard deviation. In detail for $N = 4$, σ_d even deteriorates. The standard deviation for the bipolar modulation process $\sigma_{d,bip}$ is approximately $\sqrt{2}$ better than $\sigma_{d,uni}$.

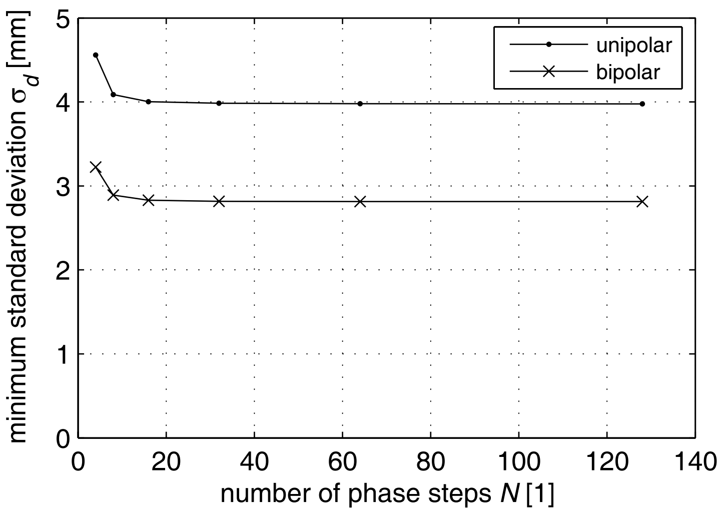

Figure 3.9 Calculated standard deviation depending on the number of phase steps *N* with P_{opt} = 1nW, $t_{measure}$ = 1ms, λ = 650nm, *ER* = 10

In the next step the influence of background illumination on σ_d has been investigated. The results shown in Figure 3.10 indicate that an increase of background light above the signal level of P_{opt} = 1nW strongly increases the minimal achievable standard deviation. An increase of $P_{opt,back}$ by a factor of 100 results in 10 times higher standard deviation. Therefore even for a readout circuit performing optimal background light suppression an optical band-pass filter should be used to filter all unwanted wavelength components.

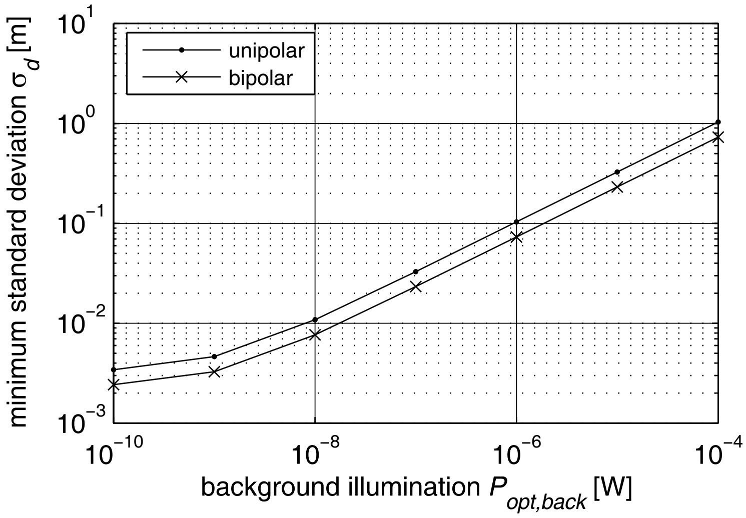

Figure 3.10 Calculated standard deviation depending on background illumination with P_{opt} = 1nW, $t_{measure}$ = 1ms, λ = 650nm, N = 16

To proof the validity of eq. (3.28) simulations using Matlab software have been done. The simulations performed for a uni-polar correlation process using the realisations of Figure 3.8 are exactly coincident with the calculated standard deviations. To determine a single value of σ_d, 100 random square-wave signals have been generated to simulate the photon noise. The duration for a single distance measurement is $t_{measure}$ = 1ms.

The achievable standard deviation is inversely proportional to the square root of the received optical signal power as shown in Figure 3.11. Using the constant measurement time $t_{measure}$ and the wavelength λ of the illumination source, σ_d is also proportional to $\sqrt{\bar{n}}^{-1}$. According to (3.28) the standard deviation is indirectly proportional to the modulation frequency f_{mod}. This influence can also clearly be seen from Figure 3.11. Summarising all results σ_d can be quantified by (3.29) with the average optical power due to background illumination $P_{opt,back}$, the average signal power $P_{opt,signal}$ and the total number of photons from background light $\bar{n}_{back}$ and received signal $\bar{n}_{signal}$.

$$\sigma_d = k_p \frac{c_0}{4\pi f_{mod}} \sqrt{\frac{hc_0}{\lambda P_{opt,signal} t_{measure}} \left(1 + \frac{P_{opt,back}}{P_{opt,signal}}\right)} = k_p \frac{c_0}{4\pi f_{mod}} \sqrt{\frac{1}{\bar{n}_{signal}} \left(1 + \frac{\bar{n}_{back}}{\bar{n}_{signal}}\right)} \qquad (3.29)$$

The proportional factor k_p has to be calculated separately depending on the modulation process and the input signal type, e.g. square-wave or sine. For the uni-polar correlation process with optical square-wave signals k_p was found to be $k_p \approx 2.5$. For the bipolar modulation process the factor is $k_p \approx 1.76$.

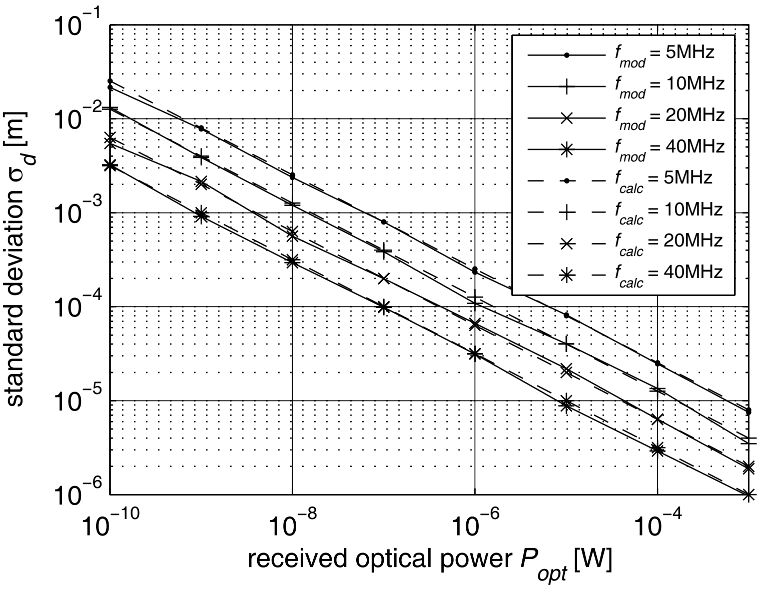

Figure 3.11 Simulated and calculated standard deviation depending on signal power with $t_{measure}$ = 1ms, λ = 650nm, *ER* = 10, *N* = 16

Analysis of (3.29) leads to different possibilities to improve the achievable standard deviation caused by photon noise of TOF based distance measurement systems.

The correlation process should be of **bipolar** type. The correlation process is determined by the readout circuit. Especially for non-correlating photodetectors e.g. PIN photodiodes suitable readout circuit structure can easily be developed.

Limiting the unambiguous range to the maximum necessary distance range by **increasing** the modulation frequency $\boldsymbol{f_{mod}}$ decreases σ_d. The maximum useable frequency may depend on the cut-off frequency of the photodetector or any high-speed pre-amplifier in front of the correlation stage.

The emitting wavelength λ of the illumination source should be chosen as long as possible. This results from the fact that due to the lower energy E_{ph} of a photon having a longer wavelength, the number of available photons for a given optical power increases. Since the responsivity R of semiconductor photodiodes strongly depends on λ and even decreases for very long wavelengths, **λ** should be chosen to meet the **maximum responsivity *R*** of the photodetector.

The received optical signal power $\boldsymbol{P_{opt,signal}}$ has to be **maximised** either by increasing the transmitted optical power $P_{opt,tra}$ or by using large receiving optics. A limit of $P_{opt,tra}$ is given due to eye-safety considerations. Large optics having a short focal length is hard to implement. Therefore a trade-off has to be found by the system designer.

The measurement time $\boldsymbol{t_{measure}}$ is often determined by the application e.g. the required frame rate for robot navigation or the reaction time for passenger position recognition for controlled airbag inflation. It should be sufficiently low to meet the timing requirements but **maximised** to decrease the photon noise.

Photons caused by background light $\boldsymbol{P_{opt,back}}$ should be **filtered away** before entering the photodetector. Typical optical filters are implemented as band-pass filters. For wavelength stable laser sources extremely narrow band filters can be used. For LED sources a wider band-pass filter is necessary.

Using a short burst of high intense optical pulses and long dark phases of the illumination source between the bursts are a possibility to increase the signal-to-background-light ratio. The principle of burst-mode illumination is depicted in Figure 3.12. For continuous-wave operation the received optical signal and the background light are processed by the photodetector and furtheron by the readout circuit.

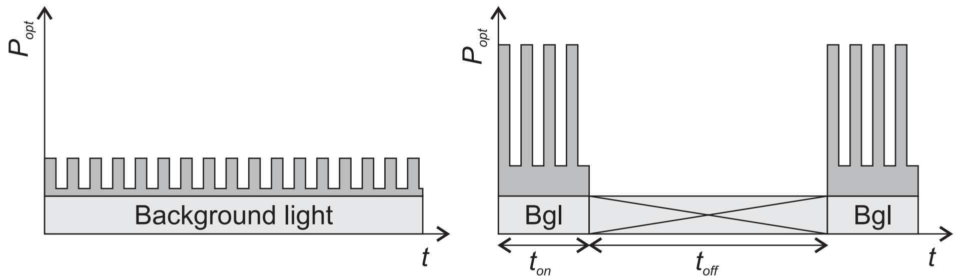

Figure 3.12 Principle of burst-mode illumination

By using short, high intense optical pulses during the time t_{on} and turning off the emitter and the receiver circuit during the time t_{off} it is possible to receive the same optical signal energy for distance determination. The received energy and therefore the number of photons dating from background light is only the fraction $t_{on}/(t_{on}+t_{off})$. This results in an improved standard deviation caused by photon noise due to an improved signal-to-background-light ratio.

The benefit of burst-mode illumination can only be utilised, if the readout circuit is capable of storing the actual measured value and continuing the measurement after the dark phase t_{off}. Furtheron the photons received during the dark phase have to be dumped without influencing the old measurement value. This is a problem e.g. for correlating CCD/CMOS detectors storing the wanted electrons below an integration gate.

For burst-mode systems, laser illumination is very common because of the large availability of dedicated pulsed laser diodes. High power LEDs are often designed for continuous-wave (CW) operation. Operating them in pulsed mode within their CW operating range results in a poor utilisation of the LEDs.

4 Integrated Photodetectors in BiCMOS Technology

Many different types of photodetectors have been introduced in chapter 2.1. External photodetectors can be fabricated from a wide range of materials e.g. MSM diodes made of GaAs or discrete PIN photodiodes made of SiGe. Integrated photodetectors arrays are built up in CMOS, BiCMOS or CCD technology. All these processes are based on silicon substrates. Therefore the specific optical properties of silicon, relevant for multi-pixel TOF systems, will be treated in this chapter.

A BiCMOS realisation of an integrated high-speed PIN photodiode developed at our institute will be discussed in detail. Originally developed for optical data receivers, it could be modified to meet the requirements of optical distance measurement systems. Furtheron the operating principle and measurement results of a highly efficient opto-electronic mixing device, the so-called double-anode photodetector (DAP) are described.

4.1 Opto-Electronic Properties of Semiconductor Materials

The principle photon detection process in a semiconductor material is based on an impinging photon that transfers the bandgap energy E_g to an electron e^- in the valence band. Due to the resulting higher energy level of the electron, it is raised to the conduction band (Figure 4.1). The missing e^- in the VB is called a hole h^+ and is interpreted as a positive charge carrier. This excitation process is also denoted as electron-hole pair generation. The e^- and the h^+ are free charge carriers inside the semiconductor until they recombine.

Photons with a lower energy cannot excite an electron. For these photons the material appears to be transparent. Photons having a lower energy cannot be detected. The $e^-{-}h^+$ pair can be separated by applying a local electrical field. Because of the opposite sign of their charges they are deflected in opposite direction.

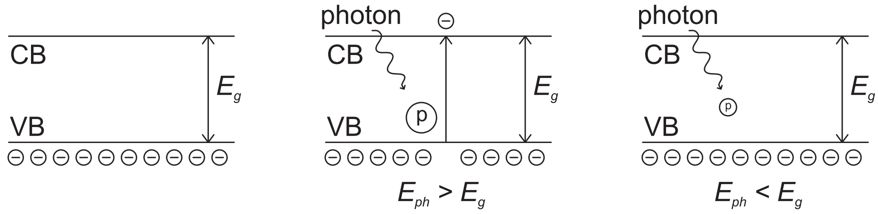

Figure 4.1 Photogenerated electron-hole pair

The situation is shown for a direct semiconductor as e.g. GaAs or InP. The energy of a single photon given by (4.1) depends only on the wavelength λ. Therefore direct semiconductors are very sensitive up to $\lambda = hc_0/E_g$ and transparent for longer wavelengths.

$$E_{ph} = \hbar\omega = hf = \frac{hc_0}{\lambda} \tag{4.1}$$

Silicon in contrast is an indirect semiconductor. This means that an additional phonon with the energy E_p has to be created or consumed during a transition process to conserve the momentum. Indirect gap materials have weaker absorption compared to direct ones thus the impinging photons penetrate deeper into the material.

The bandgap energy of silicon is $E_g = 1.12\text{eV}$ at 300K, resulting in a maximum detectable wavelength of $\lambda = 1103\text{nm}$. Therefore it can be used to detect near infrared radiation as it is necessary for optical TOF systems. The bandgap energy E_g, as well as the bandgap type, the resulting maximum wavelength λ, the intrinsic density n_i and the relative dielectric constant ε_r for various semiconductor materials sensitive in the visible wavelength range are given in Table 4.1.

Material	E_g	λ_{max}	Type	n_i	ε_r
	eV	nm		cm^{-3}	1
Si	1.124	1103	Indirect	1.5×10^{10}	11.9
Ge	0.664	1867	Indirect	2.4×10^{13}	16.2
SiC	2.416	513	Indirect		9.72
GaAs	1.424	871	Direct	1.8×10^{6}	13.18
AlAs	2.153	576	Indirect		10.06
InAs	0.354	3502	Direct	1.2×10^{15}	15.15
InP	1.344	923	Direct	1.2×10^{8}	12.56

Table 4.1 Properties of opto-electronic semiconductor materials

Due to the indirect transition process the detection probability of Si in the visible range is smaller than for GaAs or InP. On the other hand the detection probability decreases more smoothly with increasing wavelength.

One measure for this probability is the absorption coefficient α. It defines the penetration depth $1/\alpha$ of light with the wavelength λ into the material. The values of α for the materials silicon, germanium, gallium-arsenide and indium-phosphor are shown in Figure 4.2. For silicon it can clearly be seen that light in the blue range ($\lambda \approx 450\text{nm}$) is absorbed at the surface, whereas near infrared light ($\lambda > 800\text{nm}$) penetrates deep into the substrate.

The absorption coefficient for GaAs having a direct bandgap is much higher than that of Si up to $\lambda \approx 850\text{nm}$ and decreases very fast for longer wavelengths. The relatively low cut-off wavelength dates directly from the high bandgap energy of GaAs of $E_g = 1.424\text{eV}$. GaAs is often used to build LEDs and laser diodes because of the direct bandgap. It enables very effectively the radiating recombination of $e^-{-}h^+$ pairs. The same behaviour applies to InP with a sensitivity range up to $\lambda \approx 920\text{nm}$.

For the technically important infrared wavelengths of $\lambda = 1310\text{nm}$ and $\lambda = 1550\text{nm}$ Ge or SiGe photodetectors are used because of the low bandgap energy $E_g = 0.664$ of Ge. Due to the large difference in the lattice constant of Si and Ge these photodetectors cannot be implemented as OEICs right now.

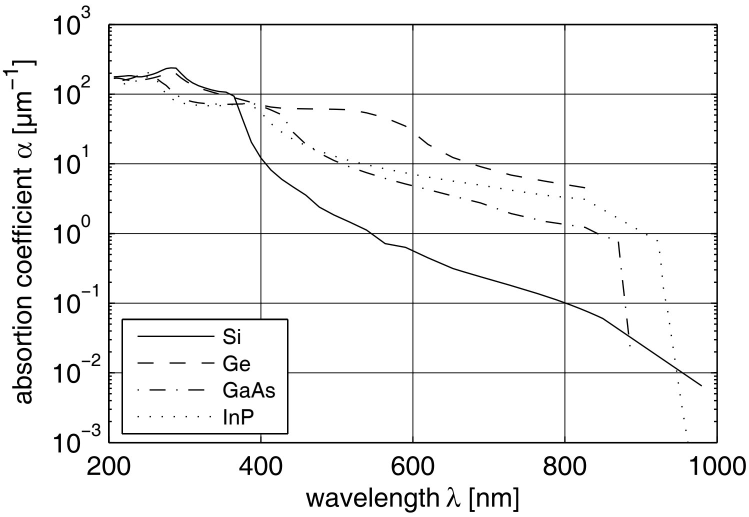

Figure 4.2 Absorption coefficient α of important semiconductor materials depending on the wavelength λ [40]

For runtime based measurement systems fast electron-hole pair separation is necessary to preserve the timing information of the received photons. Only photons generated inside the active region of a photodetector are separated sufficiently fast by an electric drift field. Photons generated in the substrate in the optimal case recombine before entering any other device of the readout circuit or reach the active region after a slow diffusion process. The travelling time is determined by the location of the $e^{-}-h^{+}$ generation and the diffusion speed. These charge carriers indicate a later arrival time for the readout circuit and influence the measured distance value. The width and position of the active region depends on the operating principle of the detector.

For an integrated CMOS SPAD presented in [19] a maximum width of $d_{apd} = 1\mu m$ is stated. The multiplication region is placed at the wafer surface. For the CCD/CMOS correlating detector shown in Figure 2.5 a maximum depth of the correlating electrical field of $d_{ccd} = 3\mu m$ is reported in [30]. The depletion region of integrated PIN photodiodes ranges from approximately 300nm below wafer surface down to 10µm. By using the Lambert-Beer law for the optical absorption it is possible to determine the electron-hole pair generation rate G_{eh} depending on the semiconductor depth x_{si} to (4.2) with the total number of photons n entering the surface during the time t [41].

$$G_{eh}\left(x_{si}\right) = \frac{n}{t}\alpha\left(\lambda\right)e^{-\alpha(\lambda)x_{si}} = \frac{P_{opt}\lambda}{hc_0}\alpha\left(\lambda\right)e^{-\alpha(\lambda)x_{si}} \tag{4.2}$$

The generation rates for constant incident power of $P_{opt} = 1nW$ and different wavelengths, depending on the depth inside a silicon waver are shown in Figure 4.3. The maximum generation rate is always at the wafer surface. Furtheron the active regions for the mentioned photodetectors are entered. The partial reflection of the incident light has been neglected because of possible dedicated anti-reflection coatings (ARC).

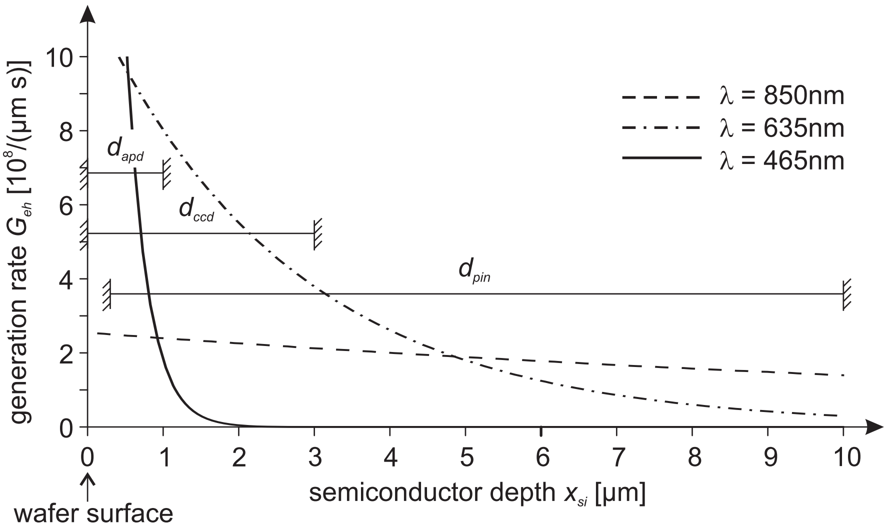

Figure 4.3 Electron-hole pair generation rate inside a silicon wafer

From the physical limitations due to photon noise it is known that the minimum achievable standard deviation σ_d mainly depends on the total number of converted signal photons. Even if the electron-hole pair generated by a single photon is amplified, as this is the case for the APD, the photon noise does not improve.

To ease the decision process which detector type fits best for TOF systems, the total number of processed photons is used instead of the responsivity R given by (4.3). The output current I_{out} depends on the number of photons n detected during the time interval t and the inherent gain k_{gain} of the detector. $k_{gain} = 1$ for CCD/CMOS detectors and PIN photodiodes. For APDs k_{gain} lies within a range of 10−100 operated in linear mode and ∞ for Geiger mode. For Geiger mode all information about the incident power P_{opt} is lost.

$$R = \frac{P_{opt}}{I_{out}} = \frac{P_{opt}t}{k_{gain}e^{-}n} \tag{4.3}$$

Integrating (4.2) over the active regions of the different detector types gives a measure of the total number of maximum useable photons n_{max}. n_{max} depends not only on the thickness, but also on the position of the active region within the semiconductor. The resulting numbers of photons, detected by silicon based photodetectors, versus the optical wavelength λ are depicted in Figure 4.4 for an incident optical power $P_{opt} = 1\text{nW}$.

$$\begin{aligned} n_{max} &= \int_{x_{min}}^{x_{max}} G_{eh}\left(x_{si}\right)dx_{si} = \int_{x_{min}}^{x_{max}} \frac{P_{opt}\lambda}{hc_0}\alpha\left(\lambda\right)e^{-\alpha(\lambda)x_{si}}dx_{si} = \\ &= -\frac{P_{opt}\lambda}{hc_0}e^{-\alpha(\lambda)x_{si}}\Bigg|_{x_{min}}^{x_{max}} = \frac{P_{opt}\lambda}{hc_0}\left(e^{-\alpha(\lambda)x_{min}} - e^{-\alpha(\lambda)x_{max}}\right) \end{aligned} \tag{4.4}$$

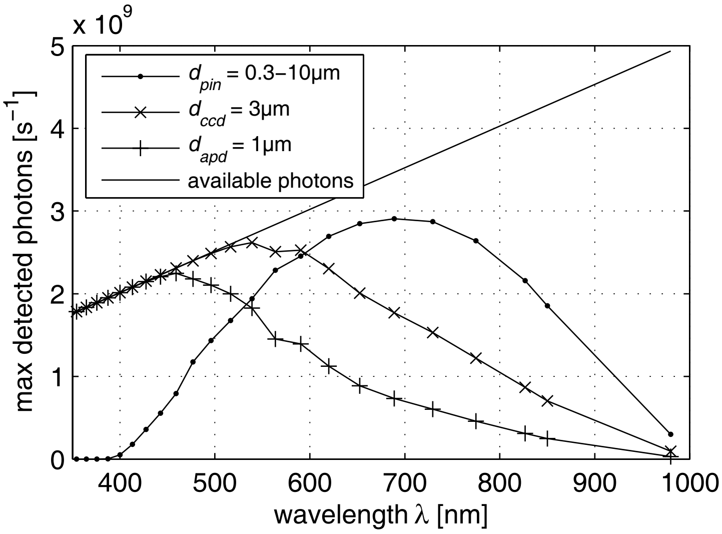

Figure 4.4 Maximum detectable number of photons n_{max} for different silicon based detector elements, P_{opt} = 1nW

Due to the thin active layer of integrated APDs, located at the wafer surface, they are most sensitive for short wavelength light. The sensitivity in the red and infrared range is very poor because the photons penetrating deeply into the substrate are not detected and therefore also not amplified. For a realised integrated SPAD an even lower photon detection probability of less than 4% at λ = 780nm is reported [20]. From the photon noise statistics it can be seen that detecting only the 25th part of the available light results in a 5 times higher minimum reachable standard deviation for a defined received optical energy, neglecting any losses occurring by the readout circuitry. Especially for low intensity levels as many photons as possible have to be detected to keep the photon noise low. Therefore SPADs are not suited very well for optical TOF systems operating in the near infrared wavelength range.

The CCD/CMOS sensor is capable of detecting light also deep in the substrate, but the immediate correlation process caused by the lateral electric field occurs only down to the depth of d_{ccd} = 3µm from the waver surface. The slowly moving charge carriers generated in the substrate are not correlated at the correct time point. Therefore they seem to date from non-modulated background light. The maximum sensitivity is around λ = 540nm.

To use an optical distance measurement system in daily life the wavelength of the active illumination has to be in the near-infrared range. To detect long wavelength light using silicon a thick detector has to be implemented. Vertical integrated PIN photodiodes do have an intrinsic layer of up to d_{pin} = 10µm thickness. This results in a maximum sensitivity at the wavelength λ = 690nm. Nevertheless it has to be mentioned that the total number of available photons increases for longer wavelengths, but the sensitivity decreases. Therefore the internal quantum efficiency decreases dramatically for near infrared light.

4.2 High-Speed PIN Photodiode

To be able to recover the phase of an optical signal correctly, the detection process has to be fast and efficient at the same time. High-speed detection is necessary to avoid the introduction of an additional phase-shift due to low-pass behaviour. Efficient detection ensures an enhanced SNR due to higher signal levels in relation to the constant noise level of the readout circuit. Furtheron it is the only way to minimize the photon noise.

Fast and efficient external photodetectors are available on a grand scale. In [42] e.g. a discrete APD is reported having a detection probability of 70% at 950nm for a bias voltage of 1600V. For an integrated setup necessary for multi-pixel realisations, such high bias voltages however, are not applicable.

A modified 0.6µm BiCMOS process is used for all integrated receivers in this thesis. The process is a planar technology. This means that for a given wafer, structuring process steps are performed only on the top surface layer. Therefore pn-junctions, used to separate the photogenerated electron-hole pairs within a photodetector, can only be diffused or implanted at the surface. As shown in Figure 4.5, three types of pn-junctions are available in standard CMOS technology to build photodiodes. These are source/drain (S/D) to well, well to substrate and S/D to substrate junctions. Using BiCMOS technology it is also possible to integrate a thin PIN diode between the p^+−S/D region and the n^+ buried collector.

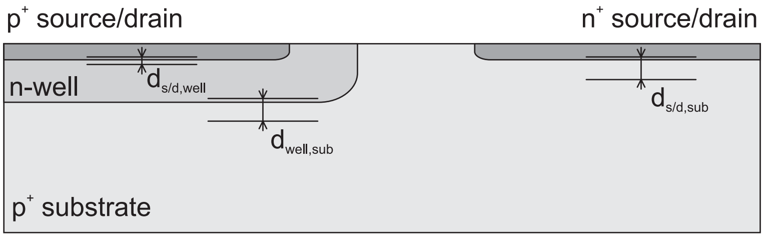

Figure 4.5 Typical pn-junctions within a CMOS process useable for photodetectors

The width of the active regions of the different CMOS diodes can be calculated by approximating their doping profiles by that of abrupt pn-diodes [41]. With the built-in voltage V_d (4.5) and the bias voltage V_{bias} the junction width d_j is given by (4.6). N_a and N_d are the acceptor respectively the donator concentrations of the p and n regions, n_i is the intrinsic concentration and ε_r is the relative permittivity of the semiconductor. ε_0 is the vacuum permittivity and T is the absolute device temperature.

$$V_d = \frac{k_b T}{q} \ln\left(\frac{N_a N_d}{n_i^2}\right) \tag{4.5}$$

$$d_j = \sqrt{\frac{2\varepsilon_r \varepsilon_0}{q} \frac{N_a + N_d}{N_a N_d} \left(V_d - V_{bias} - \frac{2k_b T}{q}\right)} \tag{4.6}$$

The location of the S/D to n-well junction in a 0.6µm technology is approximately 300nm below the surface. Also the S/D to substrate depletion region starts at about

300nm inside the semiconductor. The spreading direction of the junction is almost only into the massively lower doped region, in this case the well or the substrate. The junction of the well to substrate diode is located below the well at approximately 1.7µm. Inserting the doping concentrations $N_a = 10^{20}$ cm^{-3} for the p$^+$−S/D region, $N_d = 10^{17}$ cm^{-3} for the top of the n-well, $N_d = 10^{16}$ cm^{-3} for the bottom of the n-well, $N_d = 5{\cdot}10^{20}$ cm^{-3} for the n$^+$−S/D region, $N_a = 6{\cdot}10^{14}$ cm^{-3} for the substrate, the intrinsic carrier density of silicon $n_i = 1.5{\cdot}10^{10}$ cm^{-3}, $T = 300$K and $\varepsilon_r = 11.9$ results in the junction width d_j of the different diode types as stated in Table 4.2. Especially for the well to substrate capacitance usually the model of a graded PN junction is used, resulting in a somewhat lower value for C''_{pd}.

		V_{bias} = -3V		V_{bias} = -5V	
Diode type	V_d	d_j	C''_{pd}	d_j	C''_{pd}
	V	µm	aF/µm²	µm	aF/µm²
p$^+$-S/D-well	0.99	0.23	463	0.28	377
n$^+$-S/D-sub	0.90	2.90	36	3.58	29
well-sub	0.62	2.88	37	3.60	29

Table 4.2 Width of the space charge region of standard CMOS diodes

Comparing the widths and positions of the depletion regions of the CMOS diodes to Figure 4.3 indicates that the p$^+$−S/D to well diode is too thin to be very efficient, also the n$^+$−S/D to substrate and the well to substrate diodes are not optimal for near infrared detection. Furtheron the diode area capacitance values C''_{pd} given by (4.7) are very high for the p$^+$−S/D to well and moderate for the other two diodes.

$$C''_{pd} = \frac{\varepsilon_0 \varepsilon_r}{d_j} \tag{4.7}$$

To increase the efficiency, lower the diode capacitance and enhance speed of the diodes a thick intrinsic or low doped region between a p$^+$ and a n$^+$ region has to be inserted. The resulting structure is a vertical PIN photodiode. By modifying a BiCMOS process mainly two different types of PIN photodiodes can be realised. For the first one a thick epitaxial layer is grown on a n$^+$ buried layer serving as cathode and a thin p$^+$ anode is implanted on top of the stack. The second one is built upside down. On a p$^+$ wafer serving as anode a thick p$^-$ layer is applied before processing. A thin n$^+$−S/D implantation serves as cathode. The principal setup is determined by the available process and cannot be changed by the system designer. For the circuits following later on the first type is used.

4.2.1 BiCMOS PIN Photodiode with Buried Cathode

The necessity to reach high quantum efficiency and high-speed for an integrated photodetector led to the development of a buried collector based PIN photodiode. The structure is shown in Figure 4.6. By repeating epitaxial growing a thick n$^-$ layer is realised. The connection of the buried layer is done by a stacked n$^+$ sinker. Therefore no back-contact is necessary. The pn-junction between cathode and substrate is always reverse biased. Therefore the photodiode is completely isolated from the readout circuit.

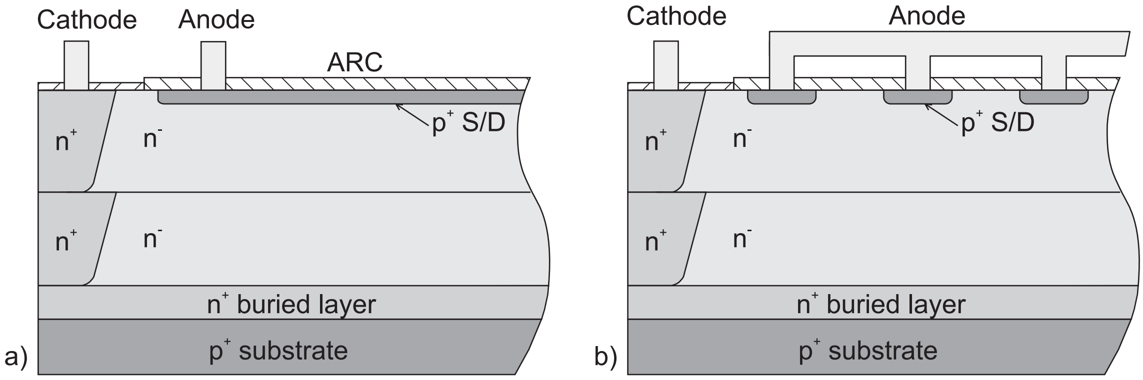

Figure 4.6 BiCMOS PIN photodiode with buried n$^+$ cathode and a) homogeneous and b) finger structured anode

The anode is either a plain or a finger structured p$^+$−S/D implantation. By using a plain anode dark currents and therefore diode shot noise can be minimized because the electric field between anode and cathode is homogenous. The diode is optimal for the red and the infrared wavelength range.

Using p$^+$ stripes as anode extends the useable wavelength range down to shorter wavelengths because also electron-holes pairs generated close to the surface are separated by an electric drift field [43]. The drawback of this solution is that high electric fields occurring at the edges of the fingers increase the dark current of the photodiode. From the simulated potential plot in Figure 4.7 the high electric fields occurring around the fingers can easily be seen.

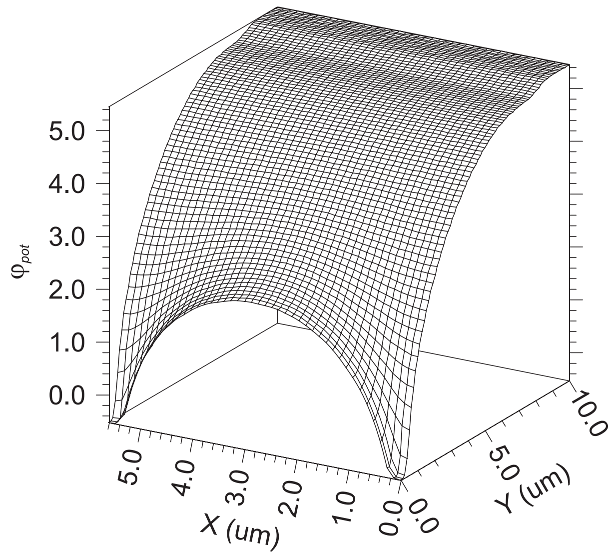

Figure 4.7 Simulated potential plot of a PIN photodiode with finger structured anode (V_{bias} = 5V)

The closer the fingers are located beside each other, the more the electric field distribution narrows to that of a standard PIN photodiode with plain anode. Furtheron the contact area between the space charge region at the surface and the ARC coating is smaller, resulting in a smaller number of e$^-$−h$^+$ pairs generated due to surface impurities. Therefore also the dark current decreases with closer finger distances. For measurement reasons two different versions of finger photodiodes have been realised. One version has metallised fingers to reduce the series resistance of the diode, the other one has no metallisation on it to maximise the responsivity.

The measured dark currents for four metallised PIN finger diodes of the size $A_{pd} = 100\times100\mu m^2$ with different finger spacing are shown in Figure 4.8. The dark currents of the finger diodes are within the range of $I_{dark} = 5-20$pA. The dark current of a homogenous PIN photodiode is in the range of $I_{dark} = 0.05-0.5$pA. Since dark current appears as shot noise it defines a lower boundary of the minimum detectable optical signal. It can be seen that an increase of the number of fingers leads to a reduced dark current. At the same time the remaining low doped area at the surface necessary for the detection of short wave light will be smaller. Therefore depending on the application a trade-off between minimum dark current and maximum responsivity in the blue range has to be found.

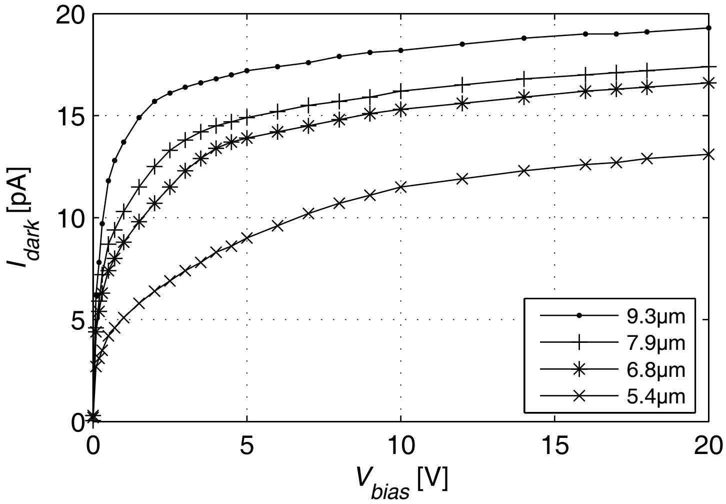

Figure 4.8 Dark current of PIN finger diodes with different finger spacing

4.2.2 Measurement Results

To build a sufficiently detailed electric model of the PIN photodiode necessary for circuit simulations all dominant electrical components have to be identified. One important component for the electrical behaviour is the parasitic photodiode capacitance C_{pd}. It consists of an area dependent capacitance C''_{pd} determined by the width of the vertical depletion region and a perimeter dependent capacitance C'_{pd}. As shown before area capacitance C''_{pd} depends on the bias voltage V_{bias} and on the doping concentration of the lower doped region $N_{a,d}$, whereas the perimeter capacitance C'_{pd} depends mainly on the layout of the diode surrounding. Summing it all up results in (4.8) for photodiode capacitance C_{pd}.

$$C_{pd} = s_{per} C'_{pd} + A_{pd} C''_{pd} \left(V_{bias}, N_{a,d} \right) \tag{4.8}$$

The total photodiode capacitance C_{pd} was measured for two different PIN photodiodes. Even though the active area of the larger diode ($A_{pd} = 100\times100\mu m^2$) is four times larger than that of the smaller one ($A_{pd} = 50\times50\mu m^2$), the measured capacitance values shown in Figure 4.9 only differ by a factor of approximately 2.7. Therefore a large portion of the total capacitance C_{pd} dates from the perimeter capacitance.

As a rule of thumb for integrated PIN photodiodes it can be stated that the total capacitance C_{pd} increases by a factor of 3 for a four times larger detector area of the same shape. Furtheron it can be seen that the space charge region reaches it maximum extension from the p^+ anode to the n^+ cathode already at a bias voltage of $V_{bias} = 1V$. Therefore a constant, bias point independent capacitance value can be used for circuit simulations.

Another important parameter for modelling the photodiode behaviour is the responsivity R. It determines the ratio of the output current to the incident optical power P_{opt} at a defined wavelength λ. An anti-reflection coating was used to maximise the responsivity. For a standard PIN photodiode with plain anode a responsivity of $R = 0.36A/W$ at a wavelength $\lambda = 660nm$ and $R = 0.26A/W$ at $\lambda = 850nm$ were measured. For the PIN photodiode with finger structured anode without metallisation the responsivity values could be enhanced to $R = 0.25A/W$, $0.43A/W$, $0.27A/W$ at the wavelengths $\lambda = 410nm$, 660nm, 850nm.

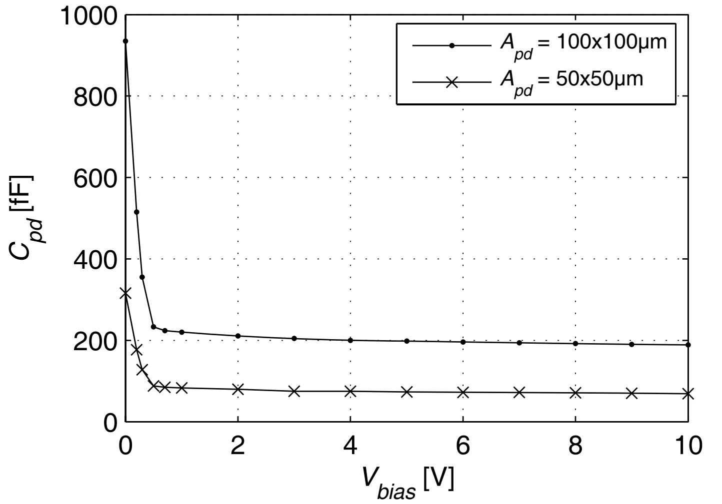

Figure 4.9 Measured photodiode capacitance C_{pd} of two integrated PIN photodiodes

Furtheron for TOF measurement systems the detection speed expressed in terms of bandwidth f_{3db} and rise t_{rise} and fall t_{fall} time is very important. The bandwidth depends on the local electric field at the position of the electron-hole pair generation. By applying a positive voltage to the n^+ cathode, two reverse biased diodes are created. These are the PIN photodiode mentioned so far and a cathode to substrate diode. All charge carriers generated in the substrate diffuse slowly toward this diode and are drained via the cathode.

Therefore inside the intrinsic region only fast detection within a local drift field occurs. Slow carrier diffusion is avoided due to the shielding effect of the cathode. This can also be seen by the high measured bandwidth f_{3db} and short rise t_{rise} and fall times t_{fall} shown in Table 4.3 even for near infrared light.

	λ = 660nm			λ = 850nm		
V_{bias}	f_{3db}	t_{rise}	t_{fall}	f_{3db}	t_{rise}	t_{fall}
V	MHz	ps	ps	MHz	ps	ps
3	255	258	556	88	2540	2620
5	709	132	274	256	703	1016
12	2243	84	200	1847	350	357
17	3000	88	187	2211	285	215

Table 4.3 Measured bandwidths and rise and fall times for integrated PIN photodiode with A_{pd} = 100×100µm²

4.3 Opto-Electronic Mixer - Double-Anode Detector

The high-speed PIN photodiode introduced in 4.2 is very fast, efficient and has a low parasitic capacitance. Nevertheless the correlation between the modulation voltage and the received optical signal has to be performed by the readout circuit. A new opto-electronic mixer based on a PIN photodiode with finger structured anodes was developed at our institute. The so-called double-anode photodetector (DAP) is capable of mixing the optical received signal and the modulation signal before entering the readout circuit [44].

4.3.1 Cross-Section

The setup and the functional principle of the DAP is shown in Figure 4.10. By reverse biasing the cathode to a positive voltage a PIN structure is realized, consisting of the p^+ anodes, the thick n^- epitaxial layer and the n^+ buried layer. Electron-hole pairs generated by the impinging photons are separated by the vertical electric field between the anodes and the cathode. The correlation between the received optical signal and the electrical modulation signal is done by applying a voltage difference between two neighbouring anodes. The voltage difference is changed in sign and amplitude forth and back during each modulation period. The positively charged holes are forced to the anode currently having the lower potential.

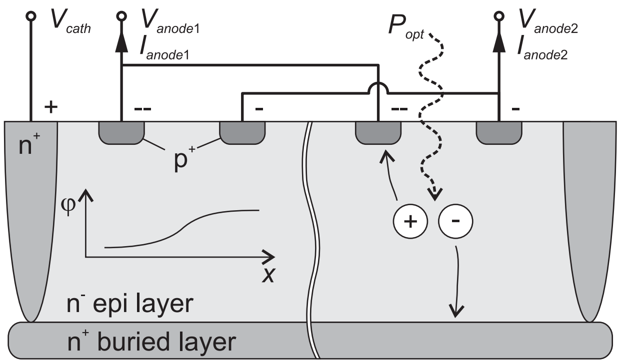

Figure 4.10 Functional principle of the double-anode photodetector

In contrast to the MSM introduced in chapter 2 is the direction of the output currents I_{anode1} and I_{anode2} always the same, independent of the sign of the modulation voltage. The phase, respectively the distance information is contained in the resulting current difference between anode 1 and anode 2. For a modulation voltage having a duty cycle of 50%, photogenerated charges, dating from background light, contribute equally to both anode currents. Therefore they appear as additional, phase independent DC offset current.

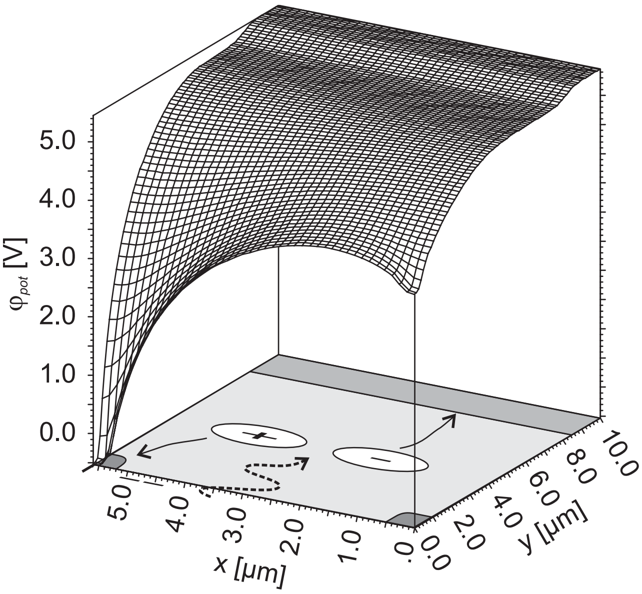

Figure 4.11 Simulated potential plot of a DAP device

The mixing mechanism can clearly be seen from the simulated potential plot in Figure 4.11. The electrons are absorbed by the cathode, whereas the holes are accelerated by the electric field along the steepest falling of the potential surface. Holes generated in the middle of the device are absorbed by anode 2 ($x = 5.5\mu m$) as intended, whereas charge carriers generated close to anode 1 ($x = 0\mu m$) are forced to anode 1 by the local electric field. This behaviour can be expressed by the separation efficiency η_{sep} given by (4.9) with the anode currents I_{anode1} and I_{anode2}.

$$\eta_{sep} = \left| \frac{I_{anode1} - I_{anode2}}{I_{anode1} + I_{anode2}} \right| 100\% = \left| \frac{\Delta I_{anode}}{\sum I_{anode}} \right| 100\% \qquad (4.9)$$

The separation efficiency depends on the applied modulation voltage, the cathode bias voltage and on the realised geometry. It can be enhanced by covering the anodes and all regions with an opaque metal layer which have a local electric field pointing to the anode having the higher potential φ_{pot}. By doing so the responsivity R of the entire device is lowered.

Transient device simulations have been performed to optimise the mixing effect. From the results shown in Figure 4.12 an expected separation efficiency of $\eta_{sep} = 66\%$ is determined with $V_{anode} = 0V{-}4V$ and $V_{cath} = 5V$.

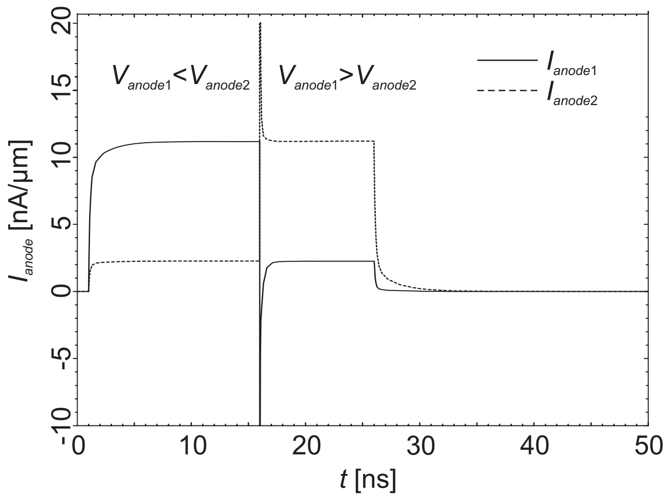

Figure 4.12 Simulated output currents of a DAP

4.3.2 Measurement Results

To be able to perform reliable circuit simulations during the TOF sensor development, an electrical equivalent circuit of the double-anode photodetector has to be derived. Since the setup for short circuited anodes is exactly that of the PIN fingerdiode, introduced in 4.2, a parasitic photodiode capacitance between anode and cathode has to be considered. Taking into account that the anode is divided into two pairs of stripe-anodes also the capacitance values C_{CA1} and C_{CA2} are half of the total photodiode capacitance C_{pd}. From Figure 4.12 two current spikes during switching of the modulation voltage indicate that a parasitic coupling capacitance C_{A1A2} between the two anodes exists.

To complete the equivalent circuit two voltage-controlled current sources are added. The sum of the output current I_1 and I_2 is equal to the current response of the fingerdiode on an optical received power. The distribution of the output current between the two anodes depends on the modulation voltage. It is determined by the separation efficiency η_{sep}.

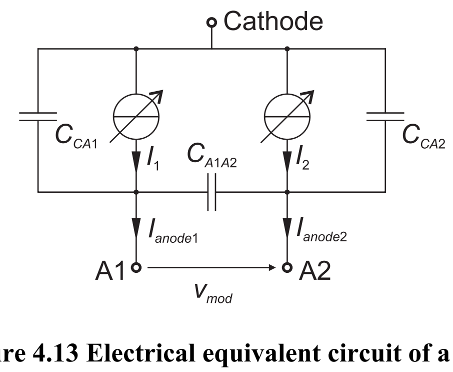

Figure 4.13 Electrical equivalent circuit of a DAP

The parasitic capacitance values of a DAP, having an active optical area of 50×50µm^2 with metallised fingers, have been measured directly on the wafer. The values are C_{CA1} = C_{CA2} = 30fF and C_{A1A2} = 17fF.

To determine the separation efficiency η_{sep} the transient response of the DAP was measured by modulating the optical light source and the anodes. As optical light source a pigtailed laser diode having a wavelength of $\lambda = 660$nm was used. One problem is to couple the optical signal into the structured photodetector. Fiber optics usually used for photodiode characterisation does have a non-uniform optical power distribution at the output resulting, in a strong position dependency for structured detectors. To homogenise the optical power at the detector surface, the fiber optics was lifted up some µm at the cost of less light falling into the detector.

The electrical measurements were performed using the measurement setup shown in Figure 4.14. Using this setup it is possible to determine the switching and therefore the maximum modulation speed and the separation efficiency η_{sep} at the same time. The 50Ω termination at anode 2 is the input resistance of a high-speed sampling oscilloscope, resulting in a direct current to voltage conversion. The node voltage at anode 2 is kept stable. The variation of 5mV caused by photocurrent through the 50Ω termination is negligible compared to the modulation voltage V_{mod} having an amplitude of 2.5V.

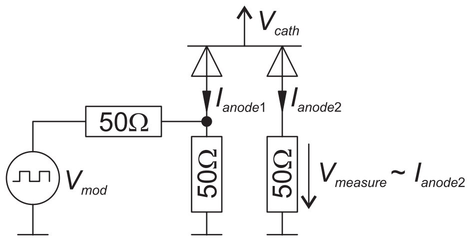

Figure 4.14 Electrical circuit for measurement of the separation efficiency η_{sep}

The measured transient response is depicted in Figure 4.15. The measurements have been performed on a DAP device which has been wire bonded to a printed circuit board. During switching of the modulation voltage V_{mod} the current spikes dating from charge injection Q_{inj} due to the coupling capacitance C_{A1A2} can clearly be seen. The amplitude of the spikes is symmetrical and independent of the incident optical power. They appear as pure AC signal with the frequency f_{mod} at the output terminal. The amplitude of an equivalent AC current is given by (4.10).

$$\hat{I} = f_{mod} Q_{inj} = f_{mod} \hat{U}_{mod} C_{A1A2} = 10 \cdot 10^{6} s^{-1}\, 5V\, 17 \cdot 10^{-15} F = 850nA \tag{4.10}$$

This current is considerably higher than the expected output current of TOF systems lying in the range of nA. Even though it is a high-frequent AC current countermeasures have to be met, as e.g. output filter or compensation networks.

The duration of the switching process is only 1.5ns to reach the steady-state output value. The rise time of V_{mod} is $t_{rise} = 1$ns, therefore the actual modulation time can be further decreased. The oscillations following the injection spike date from the parasitic inductance of the bond wire and do not occur when the device is used as an integrated detector.

Due to the symmetrical setup of the DAP the separation efficiency can now be determined by using (4.9) to $\eta_{sep} = 58\%$ with the measured output currents of $I_{anode1} = \max(I_{anode2}) = 111\mu A$ and $I_{anode2} = \min(I_{anode2}) = 29\mu A$.

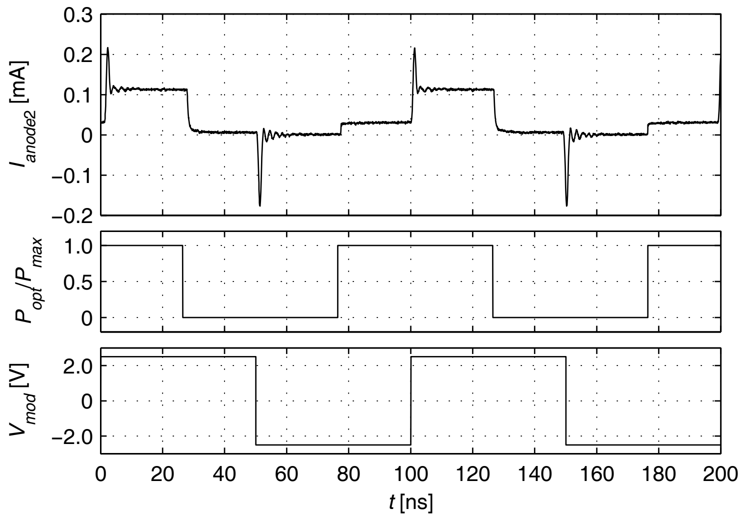

Figure 4.15 Measured transient response of a DAP with metallised fingers, V_{cath} = 4.5V, A_{pd} = 50×50µm^2

The ability of the DAP to mix an optical and an electrical signal is fundamental to determine the phase-shift of a weak optical signal. The phase information contained in the DC value of the output current can be gained by low-pass filtering or integrating the output signal. The high-frequent distortions dating from the modulation signal are suppressed that way.

Charges dating from background light are equally distributed to both anodes and appear as DC offset current. The readout circuit has to process this current, in detail the dynamic range has to be large. Inherent suppression of background light is not possible using opto-electronic mixers where only either electrons or holes are forced to an output terminal. Therefore the modulation process is of uni-polar type. Background light suppression can be performed by the readout circuit by introducing e.g. a difference integrator concept.

5 Active Readout Circuit for High-Speed Distance Measurement

To determine the distance information based on the phase delay of a very weak optical signal, two different types of readout circuits can be implemented. These are fast direct amplifying and slow integrating circuits.

The active readout circuit introduced in this chapter is capable of determining the distance information within a measurement time of $t_{measure}$ = 500µs [45]. It consists of a single-stage transimpedance amplifier, an electronic mixer and an active low-pass filter. The detector element D_{pin} is a PIN photodiode with a plain anode as shown in Figure 4.6 a). The complete readout circuit including the PIN photodiode and the active circuitry is depicted in Figure 5.1.

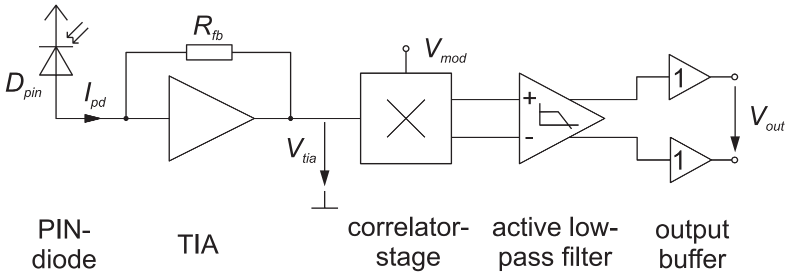

Figure 5.1 Active high-speed readout circuit with PIN photodiode

The circuitry is built as three stage architecture. The transimpedance amplifier is used to convert the photocurrent into a voltage via the high ohmic feedback resistor R_{fb}. The correlator stage performs the correlation between the digital modulation signal V_{mod} and the analogue output voltage of the TIA stage V_{tia}. The active differential low-pass filter smoothens and further amplifies the voltage signal. The output buffers are used to drive the measurement equipment and do not include any further functionality.

5.1 Transimpedance Amplifier with Electronic Mixer

The use of a TIA for current to voltage conversion is necessary to reach a high transimpedance and a high receiver bandwidth at the same time. But the main purpose of this type of input stage for TOF systems is to preserve the phase information of the optical input signal P_{opt}, which is directly proportional to the measured distance. This can easily be seen by having a closer look at the photodiode model.

The behaviour of a PIN photodiode in reverse bias mode can be modelled by an equivalent circuit consisting of two concentrated electrical components. These are a controlled ideal current source, representing the photogenerated current I_{pd} and a parasitic photodiode capacitance C_{pd}, as shown in Figure 5.2. The low-pass behaviour of the photodetector is not modelled because the high bandwidth of the PIN photodiode exceeds the one of the following TIA stage by approximately a factor of ten. The high-ohmic resistor dating from the dark current of less than 20pA can also be neglected.

The parasitic capacitance was determined using device simulation software and verified by measurements on the wafer. For circuit simulation the capacitance value was set to C_{pd} = 173fF for a photodiode having a diameter of d_{pd} = 100µm.

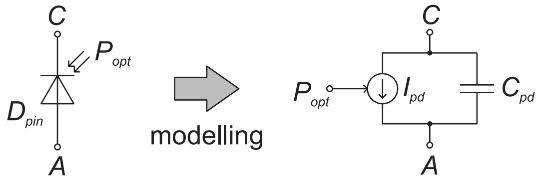

Figure 5.2 Reduced PIN photodiode model for electrical circuit design

The overall transimpedance of the TIA is R_{fb} = 200kΩ. Using a simple load resistor having the same impedance in combination with the parasitic capacitance C_{pd} would according to (5.1) result in a bandwidth of f_{3db} = 4.6MHz.

$$f_{3db} = \frac{1}{2\pi R_{fb} C_{pd}} \tag{5.1}$$

Beside the attenuation of the received 10MHz signal, especially the phase-shift changes with varying feedback resistance leading to a non-correctable absolute distance measurement error (5.2) with the input impedance Z_{in} seen from the current source I_{pd}. The maximum sensitivity of a phase change regarding to a change of the system bandwidth is at the band edge.

For the simple load resistor the phase sensitivity is given by (5.3). It is zero for very low and very high modulation frequencies f_{mod} and reaches its maximum at the system bandwidth. This result applies to all bandwidth limited systems.

$$Z_{in} = Z_{pd} \parallel R_{fb} = \frac{R_{fb}}{1 + j\omega C_{pd} R_{fb}} \quad \Rightarrow \quad \varphi = \arctan\left(-\omega C_{pd} R_{fb}\right) \tag{5.2}$$

$$\frac{d\varphi}{dR} = -\frac{\omega C_{pd}}{1+\left(\omega C_{pd} R_{fb}\right)^2} = -\frac{2\pi f_{mod} C_{pd}}{1+\left(2\pi f_{mod} C_{pd} R_{fb}\right)^2} \tag{5.3}$$

It is not possible to choose the modulation frequency very high above the system bandwidth because in this case the amplitude will be attenuated. For robust phase measurement systems therefore the bandwidth of the receiving input stage has to be sufficiently high compared to the modulation frequency.

The bandwidth of a TIA with a single poly-silicon feedback resistor R_{fb}, having a parasitic capacitance C_{fb}, is given by (5.4) [46]. The input node capacitance C_{in} is dominated by C_{pd}. For large values of the open loop gain A_v the bandwidth is much higher compared to (5.1).

$$f_{3db} = \frac{1 + A_v}{2\pi R_{fb}\left(C_{in} + C_{fb}\left(1 + A_v\right)\right)} \tag{5.4}$$

To minimize the influence of the parasitic feedback capacitance C_{fb} a capacitive coupled voltage divider network for the feedback path was used [47]. Therefore the bandwidth of the implemented TIA was increased up to $f_{3db} = 261\text{MHz}$, ensuring low phase distortion for the input stage.

5.1.1 Operating Principle

After pre-processing of the received input current by the TIA stage, the voltage is fed to a correlator. The correlation is done in two steps. In the first step the analogue voltage signal V_{tia} and the digital modulation voltage V_{mod} are multiplied by the circuit depicted in Figure 5.3. In the second step the signal is low-pass filtered. The circuit structure of the multiplier is similar to the one of a Gilbert multiplier cell, but instead of a multiplication of two analogue signals, the presented circuitry performs a digital multiplication by ±1. Thus the correlation process is of bipolar type, which is preferable considering the photon noise.

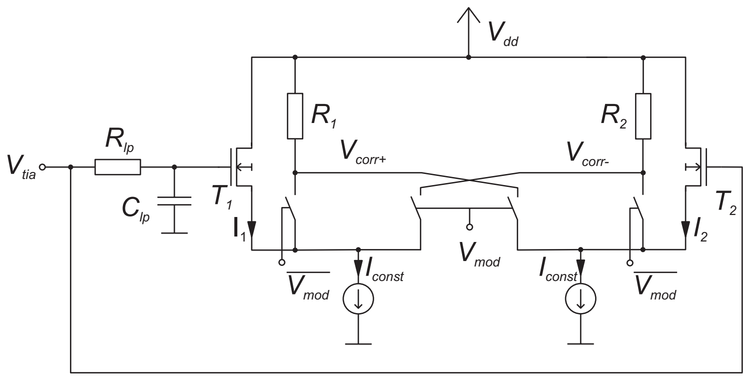

Figure 5.3 Analogue-digital multiplication stage

The multiplication stage is coupled to the transimpedance amplifier via an input low-pass filter network consisting of the resistor R_{lp} and the capacitor C_{lp} having a 3dB bandwidth of approximately $f_{3db} = 210\text{kHz}$. The DC operating points of the bypass transistors T_1 and T_2 are defined by the output voltage level of the TIA. In detail the gate voltage $V_{t1,g}$ of T_1 is given by eq. (5.5) with the current i_{bg} dating from background light.

$$V_{t1,g} = V_{tia,0} + V_{tia,bg} = V_{tia,0} - i_{bg} R_{fb} \tag{5.5}$$

It is determined by the superposition of the TIA DC output voltage $V_{tia,0}$ and the voltage decrease $V_{tia,bg}$ caused by slowly varying background light. The negative sign in eq. (5.5) dates from the inverting structure of the TIA.

The voltage $V_{t2,g}$ applied to T_2 given by (5.6) is equal to the TIA output voltage and contains also the phase information represented by the AC photocurrent i_{ph}.

$$V_{t2,g} = V_{tia} = V_{t1,g} + V_{tia,signal} = V_{t1,g} - i_{ph} R_{fb} \tag{5.6}$$

Due to the fully symmetrical structure of the circuit the difference in current flow is only determined by i_{ph}. Multiplication with the modulation signal V_{mod} is realized by two cross-coupled pairs of CMOS transistors operated in switching mode.

The functional principle can easily be understood by analysing the two different switching states. During the first half period V_{mod} is low, resulting in a current flow of $I_{const}-I_2$ through R_2. The current through R_1 is $I_{const}-I_1$. During second half period, the current flows through the resistors swap. The output voltage ΔV_{corr} (5.7) of the multiplication stage only depends on the amplitude and the phase-shift of the received optical signal.

$$\Delta V_{corr} = I_{R1}R_1 - I_{R2}R_2 = R\left(I_{R1} - I_{R2}\right) \tag{5.7}$$

The operating principle of the multiplier stage is shown in detail in Figure 5.4. Also the suppression of background light can easily be illustrated, since background light symmetrically decreases the mean value of I_1 and I_2. Thus the average value of ΔV_{corr} does not change.

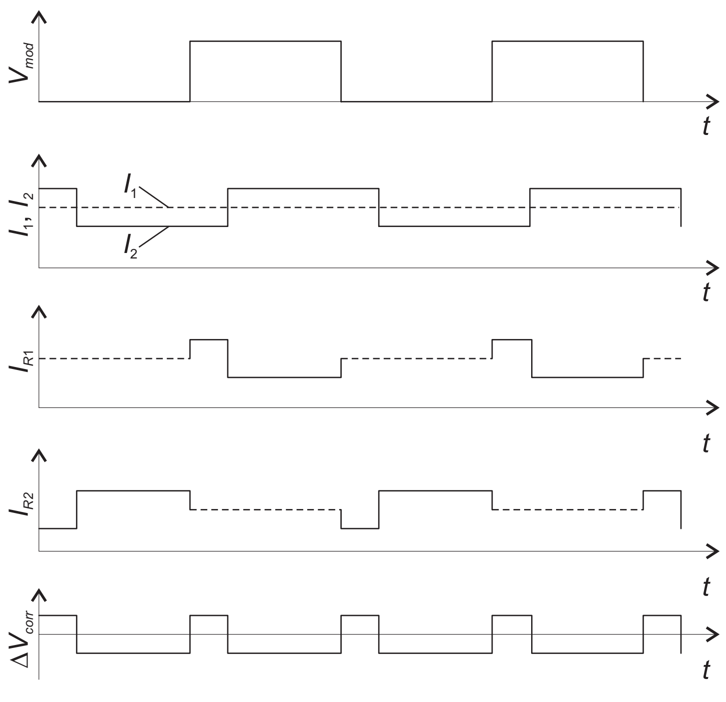

Figure 5.4 Operating principle of the analogue-digital multiplication stage

The suppression of background light is limited by the dynamic range of the input TIA operating in linear mode. For a useable TIA output voltage in the range of 1V and the feedback resistance $R_{fb} = 200\text{k}\Omega$ a maximum DC input current of approximately $i_{bg} = 5\mu\text{A}$ can be suppressed. This value exceeds the expected input signal current by a factor of 1000 and is therefore sufficiently large for indoor and most outdoor applications.

To complete the correlating functionality of the readout circuit, integration over the periodic time T_p has to be done, as stated in (3.5). Integration of a periodic signal over one period in analogue circuit design is equal to filtering the signal by using a low-pass filter having a cut-off frequency far below the signal frequency. As shown in Figure 5.4 the frequency of the output signal is $2f_{mod}$. For the presented high-speed distance measurement sensor the measurement speed is very high. In detail a complete correlation function consisting of 16 phase steps is measured within 26µs. To let pass the measured signal the filter bandwidth has to lie above f_{3db} = 40kHz. Furtheron the filter is also used to post-amplify the signal and to perform the mathematical subtraction.

The filter implemented as an active low-pass filter is built up as a bipolar differential amplifier with resistive load as shown in Figure 5.5. The differential gain is set to k_{diff} = 20. To minimize the chip area of the single pixel the low-pass functionality is realized within the differential amplifier by introducing the capacitances C_3 and C_4 between the base-collector terminals of the input transistors.

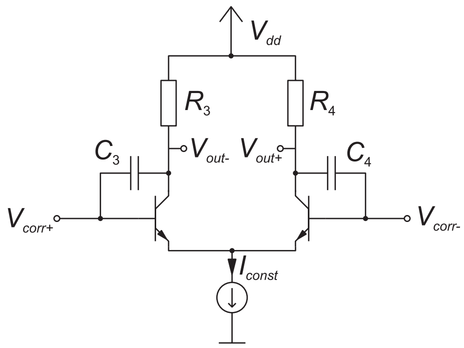

Figure 5.5 Active differential low-pass filter

Two unity gain amplifiers operated as voltage followers have been implemented on-chip to avoid distortions caused by external loads and to drive the measurement equipment.

5.1.2 Mixed-Signal Circuit Simulation

Design and simulation of the circuit was done using Cadence IC design software. The photodiode response was modelled using the circuitry shown in Figure 5.2. The rise and fall times of the optical square-wave input signal P_{opt} and the current output signal I_{pd} were assumed to be $t_{rise} = t_{fall}$ = 1ns, which could be verified by measurements.

The design of the transimpedance amplifier was done by a classical simulation approach by performing DC operating point, DC, AC, noise, transient and other types of analyses. All these analysing methods are provided by simulation software directly.

Mixed-signal simulation as it is necessary for the multiplication stage is not supported by software yet. Therefore mainly **transient simulations** can be performed to analyse the behaviour of mixed-signal circuits. The calculation effort necessary to perform transient simulations increases linearly with the simulation time. Since it may take a very long time until mixed-signal circuits reach a quasi steady-state operating point, also the possibility of performing **Monte Carlo analysis** is quite limited. Even by using dedicated simulation servers as they were available for this work these simulations have not be done due to the necessary computational power.

One way to overcome this problem is to use the **final operating point** of one simulation as initial operating point for the next simulation. Therefore the simulation time for the initial transient response can be minimized. This method works only as long as the structure of the circuit between the simulations runs is not changed. Adding or removing any devices e.g. parasitic capacitors forces a new transient simulation for the total transient response time to reach again the final operating point.

To avoid changes in the circuit structure it is good style to include all expected parasitic devices from the beginning and to set their values e.g. to zero for parallel capacitances, serial resistors or close to infinity for parallel loss resistors and so on. By doing so the overall complexity of the circuit increases. The optimal simulation strategy depends on the transient behaviour of the circuit.

Noise simulations can be approximated by adding input noise signals of sine-wave type if special frequencies are likely to occur during normal operation. For optical TOF systems e.g. 100Hz optical signals dating from light bulbs or other artificial illumination sources must be considered. Due to the extremely long periodic time of $T_p = 10$ms, compared to a reasonable simulation time of some µs it is no use to perform this kind of noise simulations. The circuit designer has to develop circuit structures that avoid problems caused by slowly varying input signals already by their operating principle.

The influence of device **mismatching** is usually simulated by performing a DC-matching analysis. Depending on the circuit structure no stable steady-state DC operating point for any switching state exists. Therefore mismatch within the multiplication stage can only be analysed during transient simulations by adding mismatch dependent voltage and current sources at critical circuit nodes. Identification of the critical points demands a high degree of experience of the designer. Mismatch analysis for pre- and post-amplifiers e.g. the TIA and the active differential low-pass filter can be done by implementing them as separate hierarchical blocks and using the analysis tools supported by the simulation software.

To verify the basic functionality of the presented circuit is to determine the phase-shift of a weak optical signal correctly. Therefore simulations have been done in the same way as the measurements are performed in the laboratory later on. For various optical intensities P_{opt} the entire correlation function has been recorded as it is shown in Figure 5.6.

The amplitude of the input current i_{ph} dating from the square-wave modulated signal was increased logarithmically from $i_{ph} = 1$n to $i_{ph} = 100$nA. The current dating from background illumination was set to $i_{bg} = 1$µA which is very high compared to the signal current. All simulations start at the same initial operating point as mentioned above. The time delay of the modulation signal V_{mod} in relation to the optical input signal P_{opt} was increased in steps by $\Delta t_{delay} = 10$ns after each simulation run. The simulations were repeated 6 times for every amplitude value of i_{ph} because for $t_{delay} = 0 - T_p/2$ one half of the triangle correlation function is recorded, including the minimum and the maximum output voltage value.

Also linearity of the output voltage depending on the time delay can be analysed that way. Linear dependence of the output voltage is indicated by equal spacing of the final value between consecutive voltage curves.

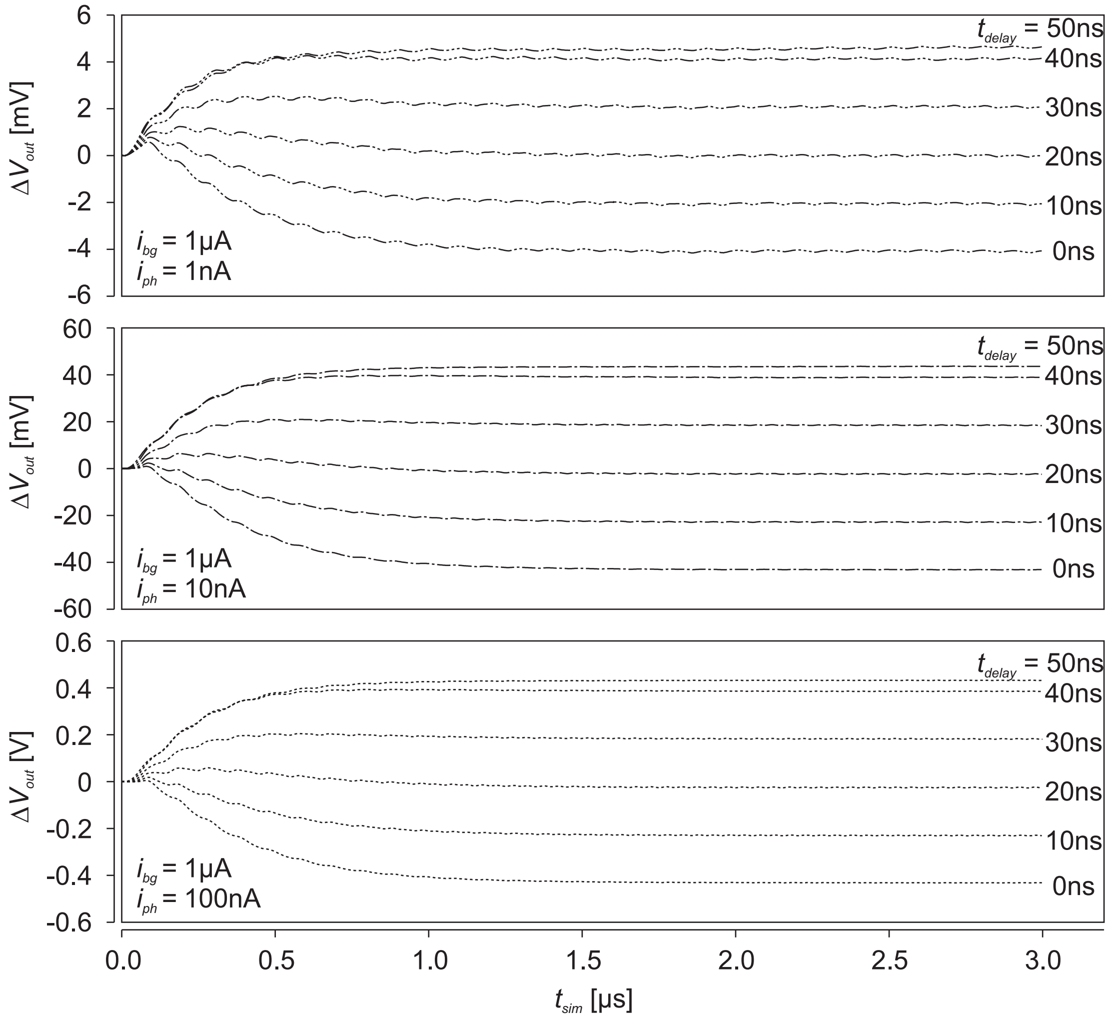

Figure 5.6 Simulated transient output voltages ΔV_{out} of the active readout circuit for high-speed distance measurement

The analysis of the simulation results shown in Figure 5.6 leads to the following circuit properties:

The settling time is maximum t_{final} = 1.2µs independent of i_{ph}. It is mainly determined by the 3dB cut-off frequency of the active differential stage. A change of the output voltage occurs after every change of the time delay or the amplitude of the received optical signal. The difference of the settling time t_{final} for t_{delay} = 0ns and t_{delay} = 50ns dates from the simulation setup. In detail the modulation voltage V_{mod} is shifted in time, instead of the input current i_{ph}.

This causes a discontinuity for the operation of the multiplication stage, therefore all voltage curves have a positive slope at the beginning of the simulation at the simulation time t_{sim} = 0−100ns. According to the simulation results a single distance measurement could be measured theoretically by performing 16 consecutive phase steps within a minimum measurement time of $t_{measure}$ = 19.2µs. The real measurement time for 16 phase steps is $t_{measure}$ = 26µs due to the digital measurement setup, as will be shown later on.

Another important characteristic value of the circuitry is the correlation sensitivity η_{sen} defined by eq. (5.8). It determines the maximum change of two measured output voltages ΔV_{out} caused by an additional time delay of $\Delta t_{delay} = T_p/2$ divided by the received signal current i_{ph}.

$$\eta_{sen} = \frac{\max\left(\Delta V_{out}\left(t_{delay}\right) - \Delta V_{out}\left(t_{delay} + \frac{T_p}{2}\right)\right)}{i_{ph}} \tag{5.8}$$

The correlation sensitivity includes the transimpedance of the TIA stage, the effectiveness of the multiplication stage and the amplification factor of the active differential low-pass filter.

Inserting the simulated final values of the output voltage ΔV_{out} into (5.8) leads to a correlation sensitivity given by (5.9) of $\eta_{sen} = 8.2\text{M}\Omega$. It is equal for all input current levels.

$$\eta_{sen} = \frac{4.2\text{mV} - (-4\text{mV})}{1\text{nA}} = 8.2\times10^{6}\,\frac{\text{V}}{\text{A}} \tag{5.9}$$

A linear dependency between output voltage ΔV_{out} and the time delay t_{delay} is necessary to measure the triangle correlation function correctly. From Figure 5.6 it can be seen that the voltage difference of the simulated curves between t_{delay} = 0ns and 10ns is equal to the one between t_{delay} = 10ns and 20ns, t_{delay} = 20ns and 30ns and so on. Only the top curve does not fit.

The difference is caused by the on-chip implemented clock driver stage. This stage is necessary to provide a stable inverted and non-inverted clock signal to the analogue-digital multiplication cell. The clock driver is built up by two chains of inverters and transfer elements. Each inverter element has a time delay between the input and the output signal mainly determined by the available technology. The clock driver consisting of inverter elements adds therefore an additional time skew t_{skew} to the modulation signal V_{mod} being approximately three times the delay time of an inverter element. The situation is shown in Figure 5.7.

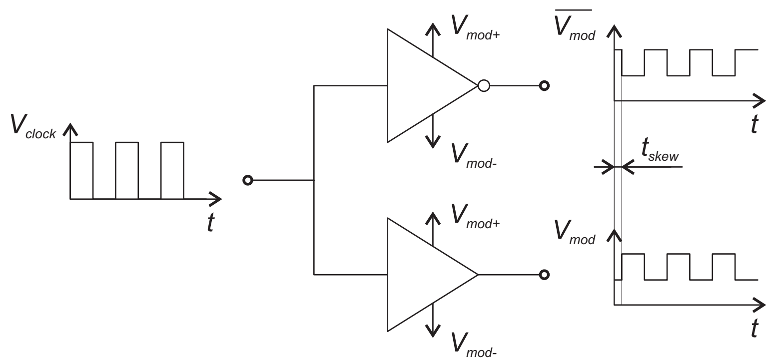

Figure 5.7 Additional time skew due to clock driver stage

This results in a measured correlation function that is virtually shifted back in time by t_{skew}. The situation is illustrated in Figure 5.8. For the ideal circuit without clock driver stage six equal spaced correlation points of ΔV_{out} would be determined. They would be placed on the straight line with positive slope of the triangle correlation function. Due to the additional time skew the correlation function is shifted back (dashed line). Therefore the correlation result for t_{delay} = 50ns moves to the straight line with negative slope. Out of this even for a linear circuitry a nonlinear simulation result occurs.

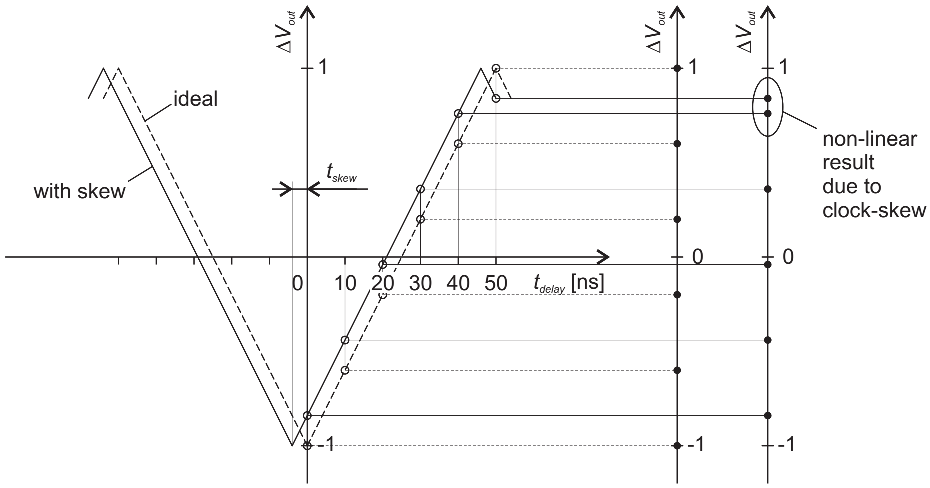

Figure 5.8 Shift of correlation function due to time skew introduced by clock driver

To be able to determine the linearity therefore at least four simulations starting at the same initial point have to be done, ensuring three consecutive points to be placed on the same straight line.

5.1.3 Measurement Setup

Similar to the simulation, also the opto-electronic chip characterisation is limited to the time domain, due to the mixed-signal circuitry. Electrical measurements by using classical measurement devices as e.g. spectrum analyser, network analyser and so on cannot be performed.

Therefore to verify the distance measurement capability of the IC an opto-electronic measurement setup was implemented. A high degree of flexibility is necessary to test ICs operating on different measurement principles. A modular, block oriented setup fits best for this task. Implementing most functionality by software ensures maximum flexibility. Signal generation is performed by an in-process programmable CPLD (complex programmable logic device). All data processing and data storage is done online during measurements.

The main functional blocks are illustrated in Figure 5.9. These are the reference clock module, the fast digital signal generator, the laser driver module including the laser diode, the opto-mechanical setup, the analogue-to-digital signal acquisition and the online data processing.

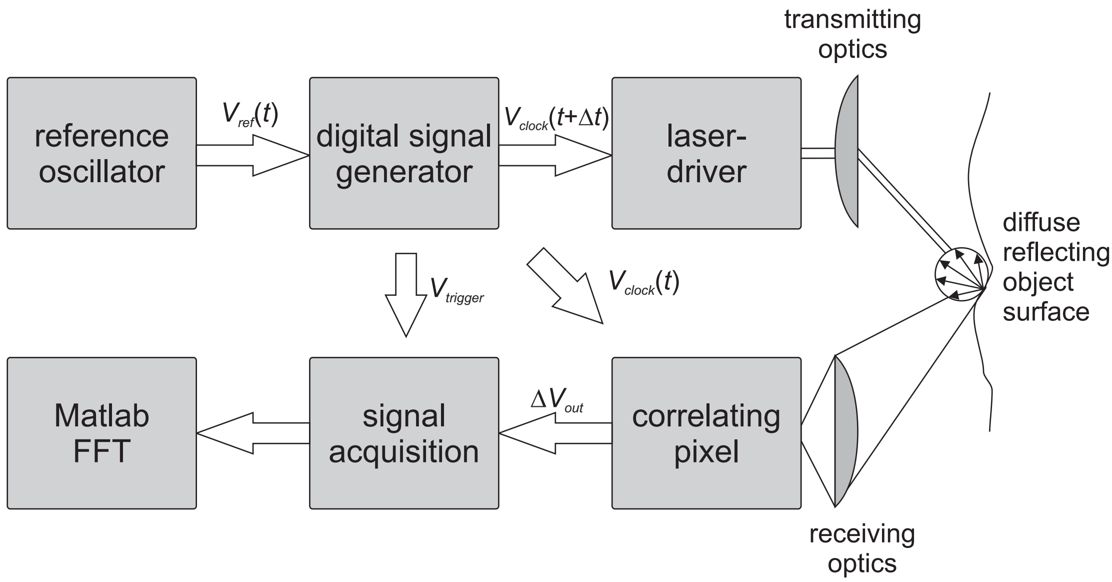

Figure 5.9 Opto-electronic measurement setup for IC characterization

The clock module generates a stable reference signal $V_{ref}(t)$ having the frequency of f_{ref} = 155.52MHz. It serves as reference signal for all distance measurements. To measure distances up to 15m the reference frequency is divided by 16. This results in a useable modulation frequency of f_{mod} = 9.72MHz. Due to the speed of light in air being approximately the vacuum speed of the light c_0 the signal wavelength is λ = 30.842m. Taking into account that the light has to propagate from the transmitter to the object and back to the receiver the unambiguous range can be determined by using (3.4) to be s_{unamb} = 15.42m.

The oscillator of type GXO-U108L/D does have a specified frequency stability of ±20ppm within the temperature range of −10 to +70°C. According to eq. (5.10) this results in a maximum distance uncertainty of Δs_{ref} = 0.617mm.

$$\Delta s_{ref} = s_{max} - s_{min} = \frac{c_0}{2}\left(\frac{16}{f_{ref}\left(1-20\text{ppm}\right)} - \frac{16}{f_{ref}\left(1+20\text{ppm}\right)}\right) = 0.617\text{mm} \tag{5.10}$$

The desired resolution of the implemented distance measurement systems lies in the cm range. Therefore the distance uncertainty is good enough for chip characterization. Due to the non-systematic behaviour of this error, it is treated as input noise for the distance measurement procedure.

Digital signal generation is the most critical part of the measurement setup. The signal generator has to generate all signals necessary to supply the laser driver, the correlating pixel and the data acquisition system. All signals have to be synchronous at a very high precision. The actual signal generation is performed by a fast CPLD having a maximum allowed input clock frequency of 400MHz, equal to a period time of 2.5ns. In comparison to reach a distance resolution of 1cm, means to resolve time intervals of 66ps correctly. Synchronisation of the signals is realized by adding synchronised clocked D-latches on every signal output.

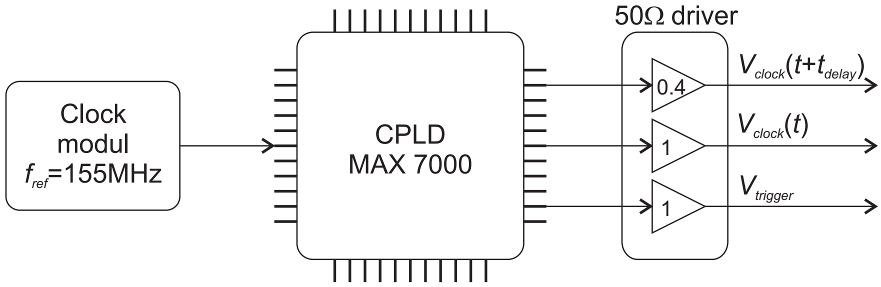

Figure 5.10 Functional setup of digital signal generator board

The principle setup of the signal generator board is shown in Figure 5.10. The board contains the reference clock, the CPLD and 50Ω line drivers. The line drivers are used to decouple the CPLD output stages from the 50Ω based measurement system. 50Ω cable and termination resistors are used to eliminate all electrical reflections. Furtheron pulse shaping is performed by the line drivers ensuring rise- and fall-times of the generated signals of t_{rise}, $t_{fall} \approx 1$ns. The line driver is also adjusting the output voltage levels using resistive voltage dividers.

One problem that has to be considered is that every device connected in the laser path between the CPLD and the laser driver adds an additional time delay, which is interpreted by the correlation receiver as a virtually increased distance. A time delay added to the sensor path is interpreted as a shorter distance.

Regarding the line drivers this means that the additional time delays introduced by the 50Ω drivers between CPLD output and the laser modulation signal $V_{clock}(t+t_{delay})$ and between CPLD output and the modulation signal $V_{clock}(t)$ of the opto-electronic integrated circuit (OEIC) have to be equal or at least constant.

Two different ways are possible to ensure equality of the additional time delays. The first approach is to use two identical 50Ω line drivers, the second one is to use a single 50Ω line driver with two input channels.

Fully electrically decoupling of the signals $V_{clock}(t)$ and $V_{clock}(t+t_{delay})$ is reached by using two separate line driver ICs. This ensures that the shape of the rising and falling edge of one signal is independent of the state of the other signal. The setup is depicted in Figure 5.11. It can be seen that the shape of the different signals is OK. Due to the usage of two different ICs in different packages the temperatures of the drivers usually are unequal and therefore the additional time delay might vary during a long-run measurement.

As mentioned before, already a small variation of the time skew of one driver of t_{skew} = 66ps (equal to a frequency of 15GHz) leads to a distance measurement error of 1cm. Different chip temperatures occur e.g. because of different load currents dating from different output voltage levels as it is the case for the laser and the modulation signal. This effect can easily be verified by measuring the distance of a single point over a long time range. The period time of the slowly varying variations lies within the range of 10 to 20min depending on the control mode of the heating and cooling system (air condition) of the laboratory.

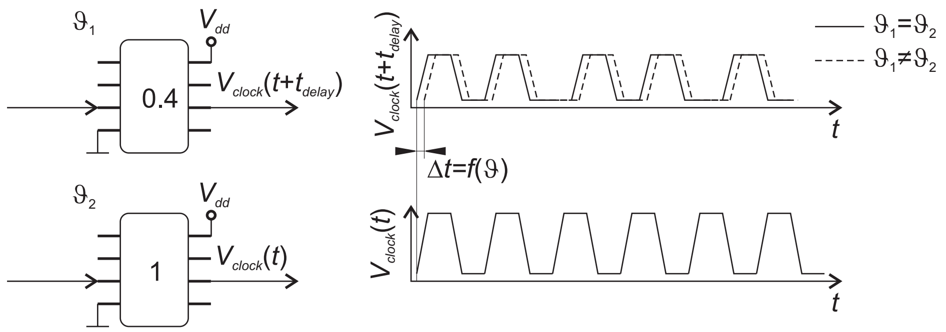

Figure 5.11 Temperature dependent time delay Δ*t* = *f*(ϑ) due to separated line driver ICs

By using only a single line driver IC, temperature drift between the two channels can be completely avoided. Main drawback of this solution is that the synchronised outputs of the CPLD force the line driver to switch the driver outputs synchronously as well.

Depending on the phase step given by the CPLD three cases have to be distinguished. As shown in Figure 5.12 both signals can change from the low to the high state at the same time. Therefore the change of the supply current I_{dd} is maximal during switching. Due to package inductances and resistors the rise times t_{rise} of the output signals increase. When the switching time does not overlap the situation is similar to the one with two driver ICs. The third possible state is that the rising edge of one signal occurs at the same time as the falling edge of the other signal. In this case the current of one output driver stage can commutate to the other driver and even lower the rise time t_{rise} for this switching setup.

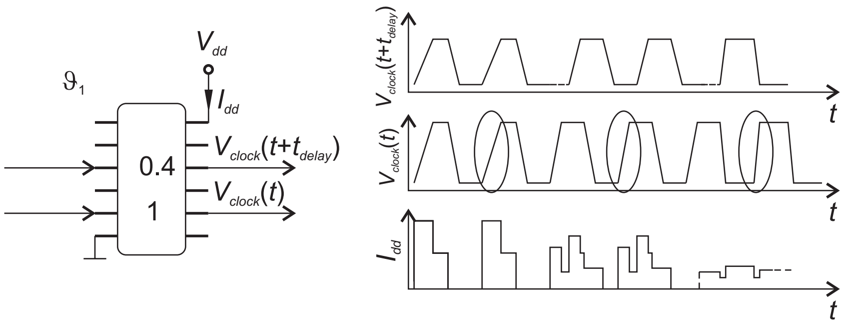

Figure 5.12 Different rise and fall times for a single chip two-channel line driver

For the mentioned CPLD based setup $N = 16$ different phase steps are generated. Therefore one phase having a shorter and one having a longer rise time t_{rise} is expected, whereas the 14 other signals should be similar. This behaviour could be verified by measuring the eye diagram of the modulation signal. By triggering on the rising edge of the modulation signal, the change in pulse width can be measured accurately by recording the falling edge over many cycles. From the measurement result shown in Figure 5.13 it can be seen that the change of pulse width is ±340ps. The influence on the actual distance measurement result is different from the temperature drift of the two separate line driver solution, explained before. In detail the correlation receivers change their operating point for varying duty cycles, resulting in a non-zero output signal, even if no light is received.

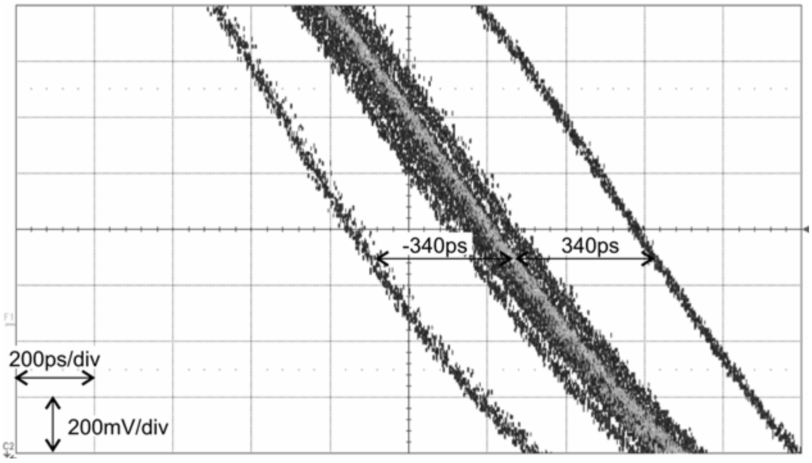

Figure 5.13 Measured change of the pulse width of the modulation signal due to single chip two-channel 50Ω line driver

This effect determines a lower boundary of the minimum necessary received optical power P_{opt}, to measure an object distance correctly. Depending on the operating principle of the OEIC the first or the second solution is preferable. In general, truly integrating receivers are more sensitive to non-ideal duty cycles.

The stable, electrical laser modulation signal $V_{clock}(t+t_{delay})$ generated by the CPLD has to be mapped onto the optical transmitted signal P_{opt} without any additional phase distortion. To preserve the short rise- and fall-times of the laser modulation signal a commercial high-speed 2.5Gbit/s laser driver board, originally intended for data communication purposes, is used. High-speed laser drivers usually consist of a DC bias current source and an AC coupled current source to add the data stream based current.

A $f_{mod} = 9.72$Mhz square-wave signal is equivalent to a 128bit high and 128bit low sequence. Since high-speed communication systems demand zero offset signals within some 20 to 50 bits modifications of the laser driver concerning the lower cut of frequency were done. Therefore it is possible to combine short rise- and fall-times with a long periodic time of $T_p = 103$ns. To avoid an overshoot of the optical power at the rising edge, the amplitude of the modulated signal current has to be set less than the average current through the diode, resulting in an extinction ratio *ER* less than infinity. Therefore also non-modulated light is transmitted by the laser source. For the OEIC this is equivalent to an intensity proportional DC background illumination.

The actual optical power generation is performed by a 5mW laser diode including a built-in photodiode for optical power control. The laser diode emits at a wavelength of $\lambda = 650$nm. The wavelength was chosen in the visible range to ease adjusting of the setup. The photodetectors itself, in detail the PIN photodiode and the double-anode photodetector, were also tested on a waferprober at a wavelength of $\lambda = 850$nm. Therefore the usability of the sensors also in the near infrared range is proven.

Laser diodes are very sensitive to temperature changes. Therefore the are only suited for a laboratory setup. Cooling of the laser diode is realized by mounting the diode, into a laser collimator, which is thermally and mechanically coupled to a breadboard.

The opto-mechanical setup is done using standard optical components including iris diaphragm, first surface mirrors and 1inch receiving lenses. The optical setup is not especially optimised for a 3D measurement task. It was implemented to achieve the same optical properties as they occur for a 3D camera. Especially for short distant objects the focus point at the picture surface has to be adjusted. This circumstance is acceptable since the opto-electronic behaviour of the receiver chip has to be characterized.

It has to be mentioned that especially for multi-pixel system the use of a standard single receiving lens is not sufficient. As reference object a sheet of white paper is used for all measurements. As shown in Table 3.1 the optical properties of white paper, having a diffuse reflectivity of ρ_{ref} up to 100%, are optimal for testing and comparing different types of TOF systems.

The newly developed OEICs are placed on a gold plated printed circuit board (PCB). Electrical connections are established by wire bonding the chip directly to the PCB. The PCB is mounted on a XYZ translation stage to couple the received light into the photodetector.

Signal acquisition is done using a real time sampling digital storage oscilloscope (DSO). The resolution of the input ADC is 8bit for the entire screen. Since the OEIC output signals ΔV_{out} vary in amplitude, due to the distant depending received optical power P_{opt}, the full resolution of the ADC cannot be utilized. Thus the resolution drops down to approximately 6bit to 7bit.

Due to the noisy output signals resolution can be enhanced by performing oversampling of the signal. Assuming uniformly distributed noise, the resolution can be enhanced by 4bit by performing 16 times oversampling. Because of the low resolution and the high computational power of the DSO, oversampling is a good compromise to preserve the flexibility of the measurement system. For a prototype sensor a field-programmable gate array (FPGA) or digital signal processor (DSP) based solution would be better suited.

To suppress slowly varying distortions in the output signal many triangle correlation functions are recorded sequentially within the measurement time $t_{measure}$. A typical number is around 20 correlation functions for one single distance measurement. Therefore high-frequent noise is suppressed by performing oversampling, whereas low-frequent noise is suppressed by shortening the measurement time of a single correlation function.

Distance calculations are performed online by the DSO using Matlab software package. The software functionality is illustrated in Figure 5.14. The main tasks of the software are to determine the trigger points which serve as reference phase; to average the data points for resolution enhancement; to overlay the triangle functions in the correct order; to calculate the distance information and to store all necessary data on the network. For each distance point the 16 final values of the averaged triangle correlation function, the calculated distance value and a time stamp is stored.

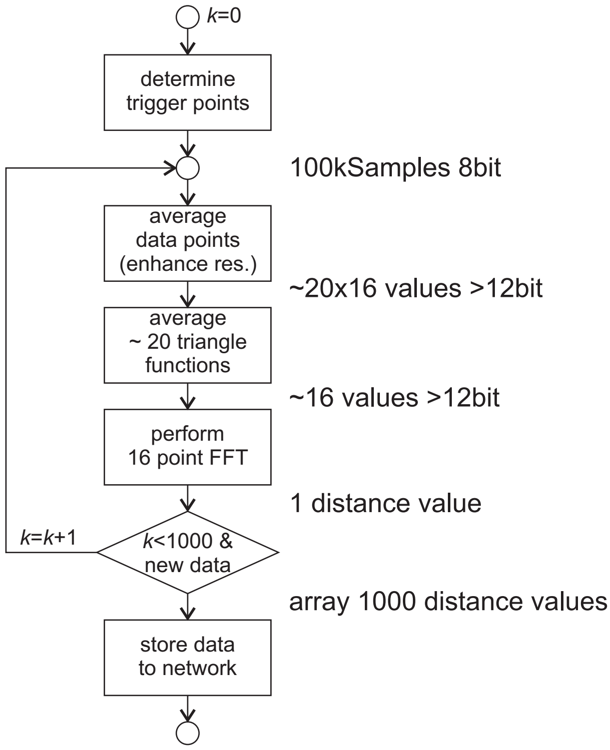

Figure 5.14 Flow chart of the distance calculation process

All relevant information's e.g. as the amplitude, the phase-shift and so on of the received signal are contained in the 16 input values fed to the FFT. Detailed data analysis like determination of linearity error, standard deviation, intensity dependence is done offline.

5.1.4 Measurement Results

All measurements were performed in a laboratory environment. To simulate background light the entire measurement setup was illuminated by neon lamps. Comparable illumination conditions occur for indoor use of the sensor e.g. in industrial manufacturing halls. As non-cooperative, diffuse reflecting object white paper was used. It was illuminated by the laser diode transmitting an average optical power of $P_{opt} = 1.44$mW to the object surface at a wavelength $\lambda = 650$nm. The PIN photodiode based sensor can also be used for near infrared active illumination, due to the similar responsivity of the photodetector $R = 0.36$A/W at $\lambda = 660$nm and $R = 0.26$A/W at $\lambda = 850$nm.

The high-speed distance measurement sensor directly amplifies and converts the optical received signal by the TIA stage, thus maximum sensitivity is reached already after approximately $t_{final} = 1.2$µs as was shown in Figure 5.6. No slow integrating process is involved. Choosing the optimal measurement time for a single phase step is critical. On the one hand it should be as short as possible to measure as many triangle functions within $t_{measure}$ to suppress slowly varying distortions, on the other hand the time should be long enough to reach the maximum sensitivity. Since the output voltage of the OEIC is covered by noise the time for a single phase step has to be at least t_{final} to reach maximum signal-to-noise ratio. Since the high-speed digital signal generator is only capable of dividing the reference frequency by multiples of two also the duration of a single phase-shift step t_{step} has to be a multiple of two of the periodic time T_p. According to (5.11) the step time was chosen to be t_{step} = 1.65µs.

$$t_{step} = 2^k T_p = 2^4 \cdot 102.9\text{ns} = 1.65\mu\text{s} \tag{5.11}$$

A typical measured output signal is depicted in Figure 5.15. The upper curve shows the trigger signal. Since the data acquisition is asynchronous the data intervals for each triangle function have to be derived from the trigger signal $V_{trigger}$ by software. The lower curve shows the sequentially measured triangle correlation functions.

Within the total acquisition time of a single distance measurement of $t_{measure}$ = 500µs 18 triangle functions are recorded. By measuring a smaller number of correlation functions the acquisition time can further be reduced at the cost of an increased standard deviation. Comparing the triangle shape with Figure 3.3 it can be stated that not only the fundamental wave of 10MHz, but also the higher harmonic frequencies of the received signal are processed by the TIA and the analogue-digital multiplication stage. Therefore the high bandwidth of 260MHz of the TIA can indirectly be seen. The offset voltage of the output signal ΔV_{out} of −0.41V dates from device mismatching in the analogue-digital multiplication stage and the active differential low-pass filter.

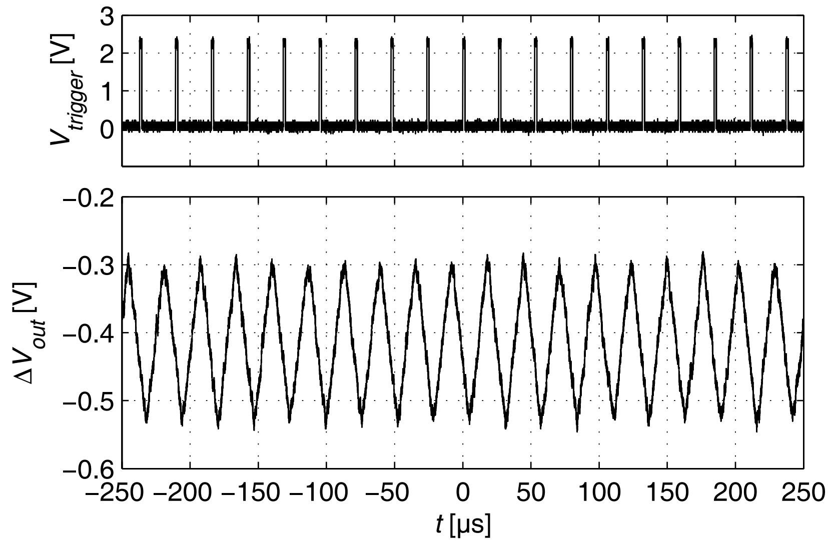

Figure 5.15 Measured sensor output signal of a *s* = 1m distant object

Having a closer look on the measured signal clearly indicates the limited resolution of the input ADC of the DSO. One single phase step of the measured signal is depicted in Figure 5.16. The minimum resolution in this case is 2.21mV. Since the amplitude of the noise level of the output signal is approximately 5mV oversampling for resolution enhancement is possible. Improving the measurement setup using a high resolution ADC in combination with an input low-pass filter would reduce the noise level and therefore the necessary sampling rate. To preserve maximum flexibility this will not be done for the current laboratory setup.

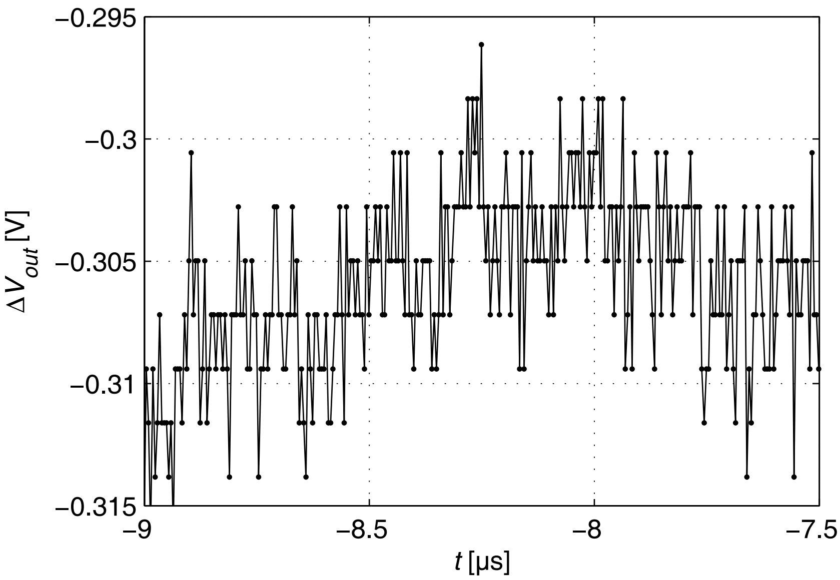

Figure 5.16 Output signal over-sampled by high-speed, low resolution ADC

Determination of the distance measurement characteristic was done by moving the object from the most distant point toward to the receiver. The target was shifted 0.1m every step. For each distance 100 measurement values were acquired to determine the linearity error s_{lin} and the standard deviation σ_d of the OEIC. The achieved distance measurement range is s_d = 0.1m−3.7m. The lower limit is determined by the receiving optics, because almost no collimation of the received light occurs for short object distances. The upper limit is given by the maximum acceptable standard deviation.

The actual distance measurement characteristic determined by averaging 100 measurement values for every object distance is shown in Figure 5.17. The strictly monotonic increase of the measured distance $s_{measure}$ can clearly be seen. Strictly monotonic increase is a necessary condition to assign a unique real distance value s to a measured value $s_{measure}$.

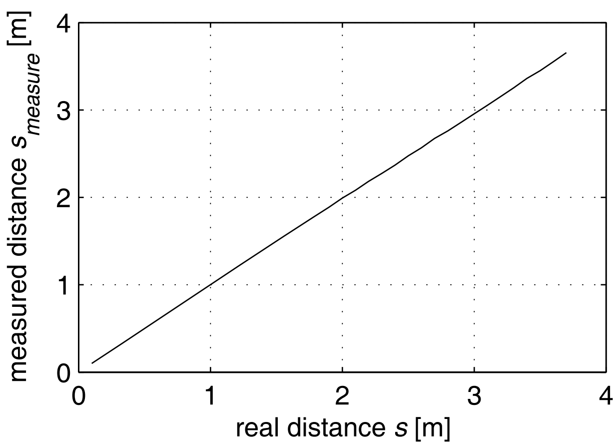

Figure 5.17 Measurement characteristic of the high-speed readout circuit

The condition defines the minimal achievable resolution of a sensor. This can easily be proven by having a look at the linearity error shown in Figure 5.18. The object is shifted by 10cm steps. If the linearity error of two neighboured measurement points differs more than −10cm (e.g. −12cm) the closer measurement point would be interpreted to be 2cm far distant than the following point. In this case the distance measurement is not unambiguous anymore.

For the characterized OEIC the minimal resolution is $s_{res} = 1.4$cm given by the measurements at $s = 2.7$ and $s = 2.8$m. The maximum linearity error is $s = -5$cm. On a first guess the linearity error seems to be correctable by a lookup table to a large extent.

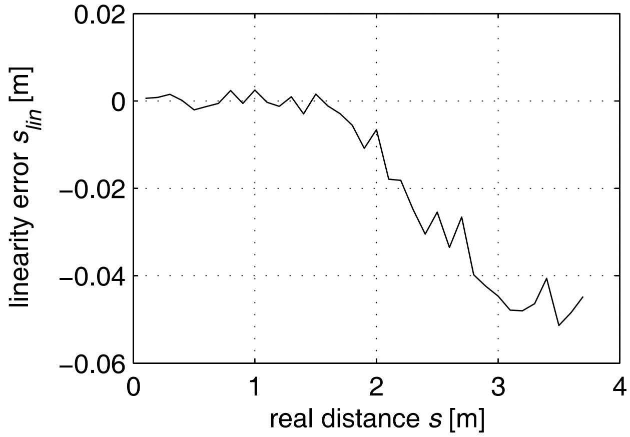

Figure 5.18 Measured linearity error of the high-speed readout circuit

Analysis of the interrelationship between amplitude of the fundamental wave of the FFT coefficients and the linearity error shows a clear dependence of s_{lin} from the amplitude. The result is shown in Figure 5.19. For amplitudes exceeding 0.05V the linearity error is less than ±3mm. For amplitudes below 0.05V a linear dependence can be seen. By using the curve-fitted dashed line, indicated in Figure 5.19, for online error correction it is possible to improve the linearity error close to the minimum resolution of $s_{res} = 1.4$cm if necessary. In a mass product sensor this can easily be done by the digital signal processor, which is used to perform the FFT operation.

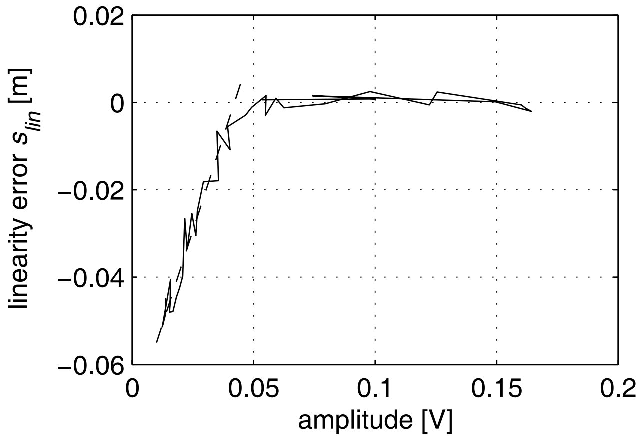

Figure 5.19 Intensity dependence of linearity error s_{lin}

The single-shot distance measurement accuracy of the OEIC is expressed by the combination of linearity error s_{lin} and standard deviation σ_d. The standard deviation is calculated from 100 distance measurement samples according to (5.12) with the average distance value given by (5.13). Since (5.13) includes the linearity error, the standard deviation can be lower than the linearity error. The total single-shot measurement error interval s_{err} can now be expressed using (5.14) with k_c defining the width of the confidence interval.

$$\sigma_d = \sqrt{\frac{1}{n-1}\sum_{i=1}^{n}\left(s_{measure,i} - \overline{s_{measure}}\right)^2} \tag{5.12}$$

$$\overline{s_{measure}} = \frac{1}{n}\sum_{i=1}^{n} s_{measure,i} = s + s_{lin} \tag{5.13}$$

$$s_{err} = s_{lin} \pm k_c \sigma_d \tag{5.14}$$

The standard deviation of the sensor is depicted in Figure 5.20. Starting from large distances the standard deviation decreases from $\sigma_d = 6.7$cm towards closer distances, because the received optical power P_{opt} increases, as expected. The standard deviation reaches a minimum of $\sigma_d = 0.5$cm at an object distance of $s = 0.7$m. Therefore optimal optical conditions for the receiver are given for this distance measurement point.

For shorter distances σ_d even increases because of the poor focusing capability of the receiving optics for short distant objects. The effect is caused only by the optical setup and not by the receiving sensor. This problem applies to most optical sensors, thus short range measurements should be avoided. In many cases this can be done by mounting the sensor at least 50cm away from the object to be measured.

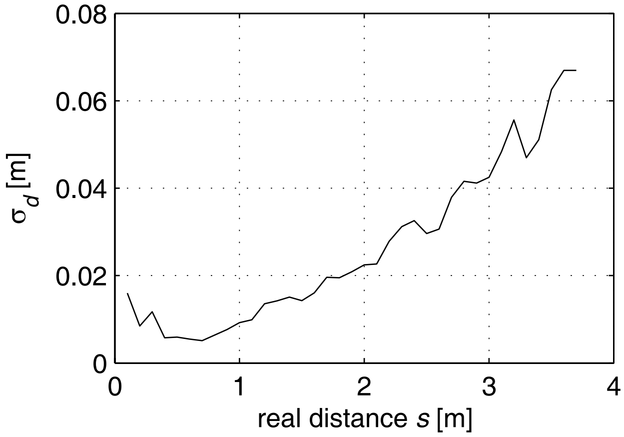

Figure 5.20 Standard deviation of the high-speed readout circuit

The OEIC was fabricated in a modified 0.6µm BiCMOS technology. All modifications concerned the implementation of the fast integrated PIN photodiode. An anti-reflection coating to enhance the photodiode responsivity R is available in the technology used. From the chip photograph depicted in Figure 5.21 all relevant functional blocks can be seen.

These are an ESD protection circuitry for the PIN photodiode A, the octagonal photosensitive area of the photodetector B, the clock driver stage for generating inverse clock signals without phase-shift in between C, the transimpedance amplifier with feedback network D, the combination of the analogue-digital multiplication stage and the active-differential low-pass filter E and output buffers to drive the measurement equipment F. Furtheron bond pads and blocking capacitors for voltage supplies can be identified. The active circuitry is operated at a supply voltage of 5V. The cathode of the PIN photodiode is biased at 8V.

The diameter of the photosensitive area of the integrated PIN photodiode is 100µm. The effective pixel size including the building block B-E is about $A_{pixel} = 220{\times}400\mu m^2$. Therefore a fill factor of $\eta_{fill} \sim 9\%$ can be derived. In a following redesign step the chip can be optimized according to minimise the active chip area to increase the optical fill factor.

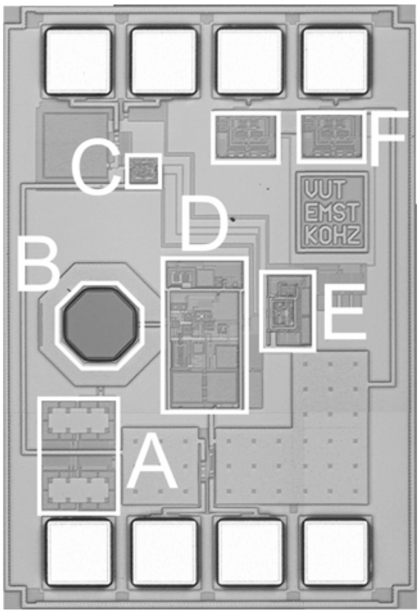

Figure 5.21 Chip photograph of the distance measurement OEIC

6 Low-Power Readout Circuits

The active readout circuit introduced in chapter 5 uses a fast transimpedance amplifier to transform the optical received signal into a signal proportional voltage. Integrated, high-speed amplifiers are associated with high power consumption. For future multi-pixel systems low-power readout circuits are necessary.

This can easily be understood by having a look at a mid resolution multi-pixel array of 32×32 pixels. All OEICs introduced in this thesis are operated at a supply voltage of 5V. Therefore a current flow of 200µA through a pixel already leads to a power consumption of 1mW. A pixel power consumption of 1mW forces a power dissipation of the 32×32 pixel IC of 1024mW, which has to be drained through the back side contact of the chip.

Therefore low-power readout circuits consuming less than 100µW of electrical power are necessary. One way to achieve this goal is to correlate the weak current signal directly with the modulation voltage and amplify the slowly varying output voltage afterwards by a low-power amplifier. The bridge-correlator circuit with PIN photodiode introduced in [48], [49], [50] and [51] is capable of doing this correlation. Distance measurements up to 3.7m could be done in combination with a differential post-amplifier.

Another way to avoid high-speed amplifiers is to perform an opto-electronic correlation directly within the detector element. Thus only DC output currents have to be further processed. A passive structure with an integrated double-anode photodetector has been investigated in detail in [49], [50] and [52]. A very promising new approach is shown in [53] where distances up to s_d = 15m could be measured.

6.1 PIN Bridge-Correlator Circuit

A classical approach in imaging technology to measure very weak optical signals is to store all photogenerated charge carriers on a capacitor. By adjusting the accumulation time it is possible to adjust the output voltage swing of the photodetector. This method is used e.g. for all CCD cameras. In a CCD camera the parasitic capacitance between a transparent photo-gate and the substrate is used as storage capacitor.

For time-of-flight systems it is necessary to correlate the received optical signal P_{opt} with an electrical modulation signal V_{mod}. This can be done by charging and discharging a capacitor by the photocurrent I_{pd} within a single modulation period T_p. Therefore a built-in capacitance as e.g. the photodiode capacitance C_{pd} cannot be used. Instead an on-chip capacitor C_{int} is used as correlating element. The main advantage of this solution is that background light can be suppressed almost ideally, whereas the square-wave signal is integrated over many periods. The circuitry capable of performing this correlation is the so-called bridge-correlator circuit. As photodetector element the highly efficient high-speed PIN photodiode shown in Figure 4.6 a) is used.

6.1.1 Functional Principle

The main components of the bridge-correlator circuit are shown in Figure 6.1. It consists of the PIN photodiode D_{pin}, the integration capacitor C_{int}, four switches and a bias voltage source V_{bias}. The cathode of the PIN photodiode is connected to V_{cath}, which can be chosen freely, as long as it exceeds V_{bias} at about 3V. The capacitor C_{int} is implemented as poly-poly capacitor. The switches are realized by NMOS transistors. The bias voltage source V_{bias} serves as level shifter. This is necessary because the sign of the output voltage ΔV_{out} can be positive or negative. A following amplifier or output buffer stage can only process signals ranging from 0V to 5V, therefore the bias voltage is set to be approximately V_{bias} = 2.5V.

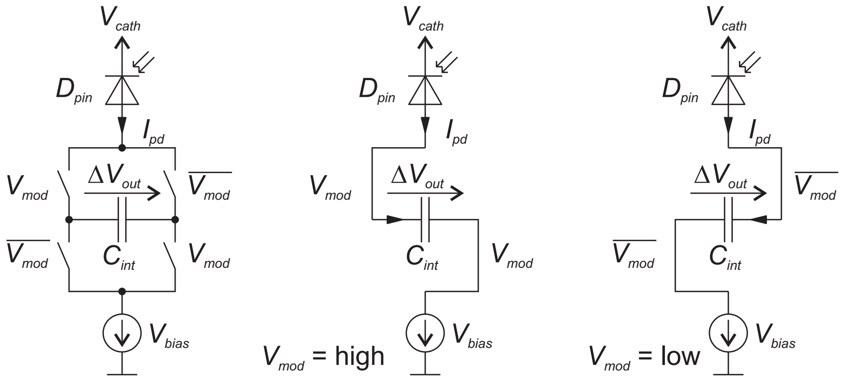

Figure 6.1 Setup of the ideal bridge-correlator circuit

The basic operating principle of the bridge-correlator circuit can be easily understood by having again a look at Figure 6.1. To illustrate the principle idea of the circuit all parasitic components, as the photodiode capacitance C_{pd} and the poly to substrate capacitance of the integration capacitor C_{int}, are neglected. They will be discussed in detail later on.

By switching the cross-coupled switches during one period in opposite way, it is possible to charge and discharge the integrating capacitor C_{int} by the photocurrent I_{pd}. In detail the switches are controlled by the digital square-wave modulation signal V_{mod}. Short circuiting of C_{int} is prevented by using non-overlapping clock signals for the two pairs of switches.

By implementing signals V_{mod} and $\overline{V_{mod}}$ having exactly the same duration for turn on time it is possible to suppress background light totally within one clock period. The situation is depicted in Figure 6.2. The photocurrent dating from slowly varying background light, indicated as light gray areas, charges C_{int} positive during the first half period. During second half period exactly the same amount of charge carriers discharges the capacitor. Therefore the actual value of ΔV_{out} at the beginning of the first period and the end of the second period is not influenced by background light. The mean value of the output voltage is only determined by the initial state.

The weak optical reflected signal, indicated by dark grey areas, having the same frequency as the modulation voltage V_{mod} again charges C_{int} positive during first half period. During second half period a smaller amount of charge carriers is available for discharging C_{int}. The difference in charge is integrated by C_{int}. Thus the output voltage ΔV_{out} increases. ΔV_{out} depends only on received signals having the frequency f_{mod} and not on DC signals.

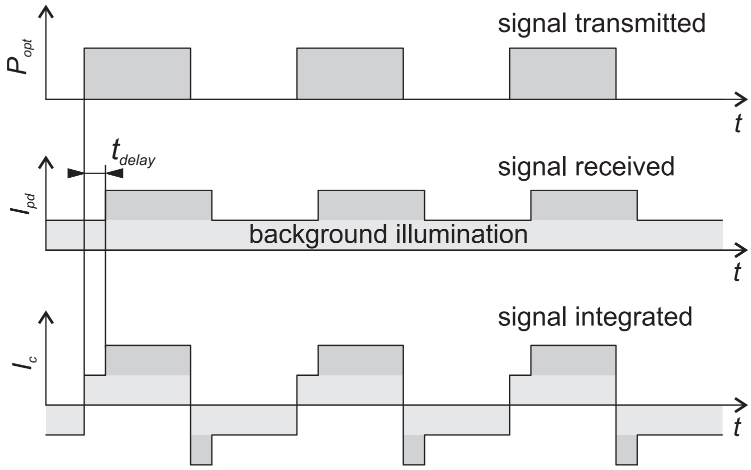

Figure 6.2 Suppression of background light by the ideal bridge-correlator circuit

The output voltage depends on the amplitude and the phase of the received signal. This property is shown in Figure 6.3. Signals dating from different distant objects have different time delays t_{delay1} and t_{delay2}. The amount of charges during the charging and the discharging period are different although the same amplitude is assumed. Depending on the time delay of the received optical signal, represented by the photocurrent I_{pd}, the mean capacitor voltage ΔV_{out} increases or decreases within every period. Therefore a phase selective correlation is performed. The situation changes if parasitics are added to the circuitry.

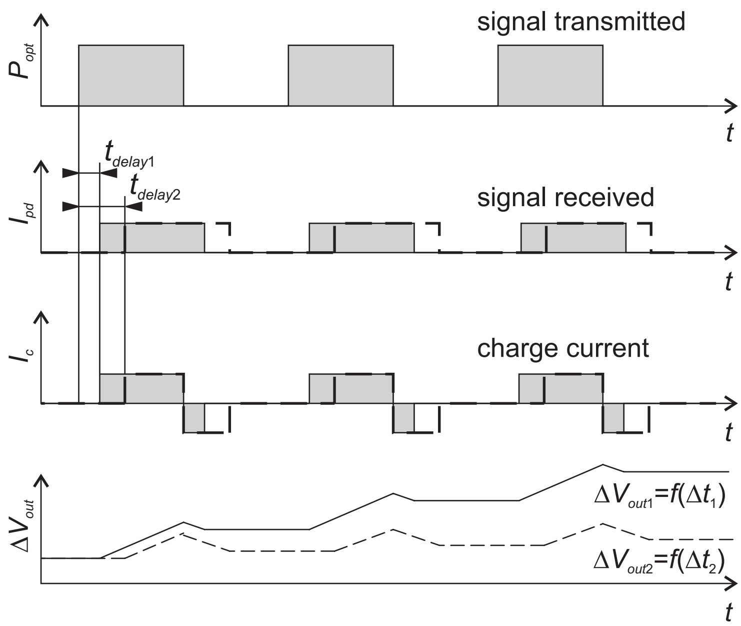

Figure 6.3 Phase selective output voltage of the ideal bridge-correlator circuit

Simulations on the ideal circuit structure shown in Figure 6.1, neglecting any parasitics, were done to study the circuit behaviour. The simulated results were equal to the theoretical results shown in Figure 6.3. In detail background light is suppressed by the circuit. The signal current is integrated on C_{int} depending on the phase delay between sent signal V_{mod} and the received signal P_{opt}.

6.1.2 Layout Considerations and Simulation Results

By implementing the circuit as an OEIC especially two types of parasitic capacitances have to be taken into account. These are the parasitic capacitances C_{par1} and C_{par2} of the integration capacitor C_{int} and the photodiode capacitance C_{pd}. To simulate the real circuit behaviour the parasitic capacitances are added to the circuit structure as depicted in Figure 6.4.

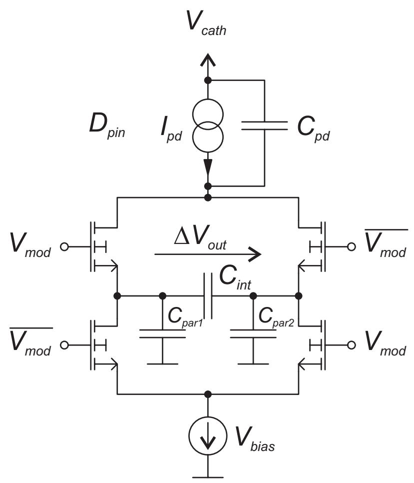

Figure 6.4 Setup of the real bridge-correlator circuit

The capacitances C_{par1} and C_{par2} are mainly determined by the parasitic capacitance of bottom capacitor plate of C_{int} to substrate which is implemented as a poly1 layer. It is isolated by a thick oxide layer. To preserve symmetry of the circuit C_{int} is implemented by two capacitors which are connected anti parallel. Therefore C_{par1} is equal to C_{par2}. The influence of these capacitances on the simulation results is comparable to additional loss elements. The reason for this can be understood by performing one modulation cycle. Starting from totally discharged capacitors C_{int}, C_{par1} and C_{par2} the modulation voltage V_{mod} is set to high. Therefore C_{par2} is short circuited by the lower right transistor and V_{bias}, whereas C_{int} and C_{par1} are connected in parallel. The charge Q_{par1} stored on C_{par1} during first half period is given by (6.1). After switching of V_{mod} the capacitance C_{par2} is connected to the photodiode. C_{par1} instead is short circuited by the lower left transistor and V_{bias}. Therefore the charge Q_{par1} is lost. The same charge loss occurs during second half period due to C_{par2}, Therefore the effectiveness of the integration process is lower than expected by the ideal structure.

$$Q_{par1} = Q_{total} \frac{C_{par1}}{C_{par1} + C_{int}} \tag{6.1}$$

Adding the photodiode capacitor C_{pd} to the bridge-correlator setup, changes the circuit topology. From comparing Figure 6.1 and Figure 6.4 it can be seen that the photogenerated current I_{pd} now has two possible current flow paths. The first path is the bridge-correlator circuit itself. The second path is the photodiode capacitance C_{pd}. Therefore the photocurrent is not forced through the switched bridge-correlator under all circumstances anymore.

The simulations methods were similar to the one explained in chapter 5.1.2. Also the bridge-correlator circuit does not have any stable DC operating point, therefore only transient simulations could be done. A typical simulation result done, using the more realistic circuitry of Figure 6.4 is shown in Figure 6.5. The photodiode capacitance was set to be $C_{pd} = 170\text{fF}$ to simulate an octagonal PIN photodiode having a diameter of $d_{pd} = 100\mu\text{m}$.

In contrast to the original functionality of the circuit, namely correlating and integrating at the same time, saturation of the output voltage ΔV_{out} occurs. The saturation effect is caused by the photodiode capacitance C_{pd} and the parasitic capacitances C_{par1} and C_{par2}. The influence of these capacitances will now be discussed in detail.

As can be seen from the simulation result, the correlation works well, for different time delays t_{delay} between the received photocurrent I_{pd} and the modulation voltage V_{mod}. The final DC output value of ΔV_{out} depends only on the time delay and the amplitude of I_{pd}. The settling time until the output voltages ΔV_{out} reach their final values is approximately $t_{final} = 0.6\mu\text{s}$. Out of this the $f_{mod} = 20\text{MHz}$ photocurrent is integrated on C_{int} at maximum over 12 periods. Further investigations to understand the occurrence of the saturation phenomenon have to be done. To separate the different effects for all further simulations the parasitic capacitances C_{par1} and C_{par2} will be neglected. This is valid since they behave like additional loss elements as was explained before.

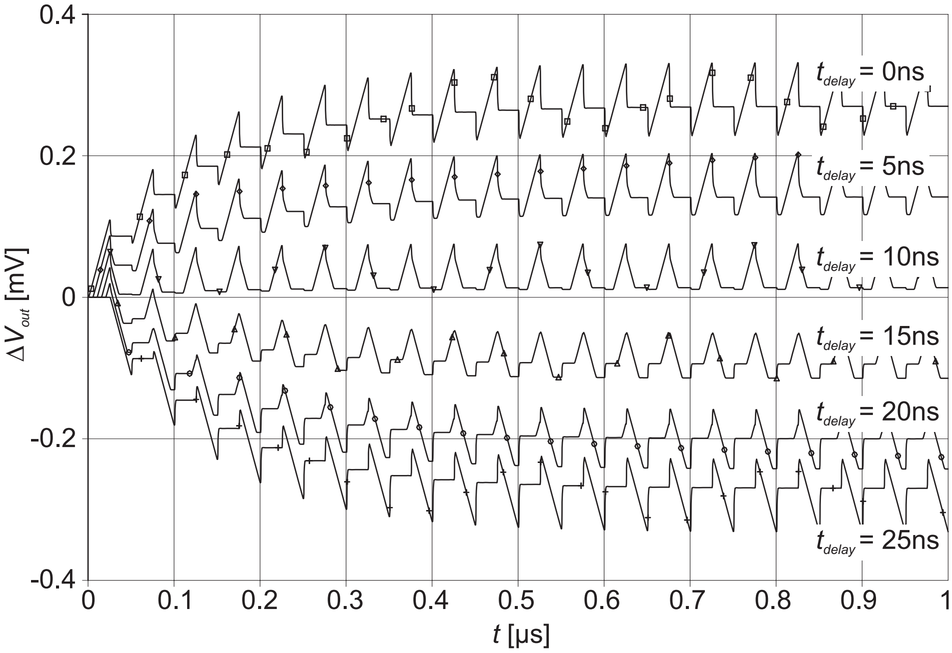

Figure 6.5 Simulation result of the bridge-correlator circuit for different time delays t_{delay} with $C_{pd} = 170\text{fF}$, $C_{int} = 2\text{pF}$, $f_{mod} = 20\text{MHz}$, $I_{pd} = 10\text{nA}$

Neglecting the parasitic capacitances the influence of three dominating circuit parameters has to be analysed in detail. These are the value of the integration capacitor C_{int}, the photodiode capacitance C_{pd} and the modulation frequency f_{mod}. The size of C_{int} can be selected arbitrarily. The photodiode capacitance is determined by the optical active area A_{pd} and the voltage across the photodiode $V_{cath}-V_{bias}$. The modulation frequency determines the unambiguous range and some other properties of the entire distance measurement system, e.g. the photon noise decreases with increasing frequency, the phase sensitivity $\Delta\varphi/\Delta s$ increases with increasing f_{mod}.

The influence of different integration capacitors C_{int} on the output voltage ΔV_{out} is shown in Figure 6.6. From a theoretical point of view a smaller integration capacitance leads to a higher output voltage swing for a constant charge according to $Q = C \cdot V$. Therefore one would assume that the use of a low-capacitance value for C_{int} leads to a maximum output voltage swing ΔV_{out} and therefore to a maximum correlation sensitivity η_{sen} of the sensor. From the simulation results a different behaviour can be seen. Depending on the value of C_{int} the time to reach the steady-state output value t_{final} increases with increasing C_{int}. Thus the maximum readout speed can be adjusted by choosing C_{int} properly.

The voltage ripple of ΔV_{out} decreases with increasing C_{int} as expected. This is important for the readout of the circuit since the voltage ripple has to be suppressed by a low-pass filter stage afterwards. A low voltage ripple relaxes the demand on the filter to reach a sufficiently high suppression of the high-frequent distortions.

The more important result is that the final steady-state value of ΔV_{out} does not depend on C_{int}. Thus the sensitivity of the circuit cannot be influenced by varying the integration capacitance.

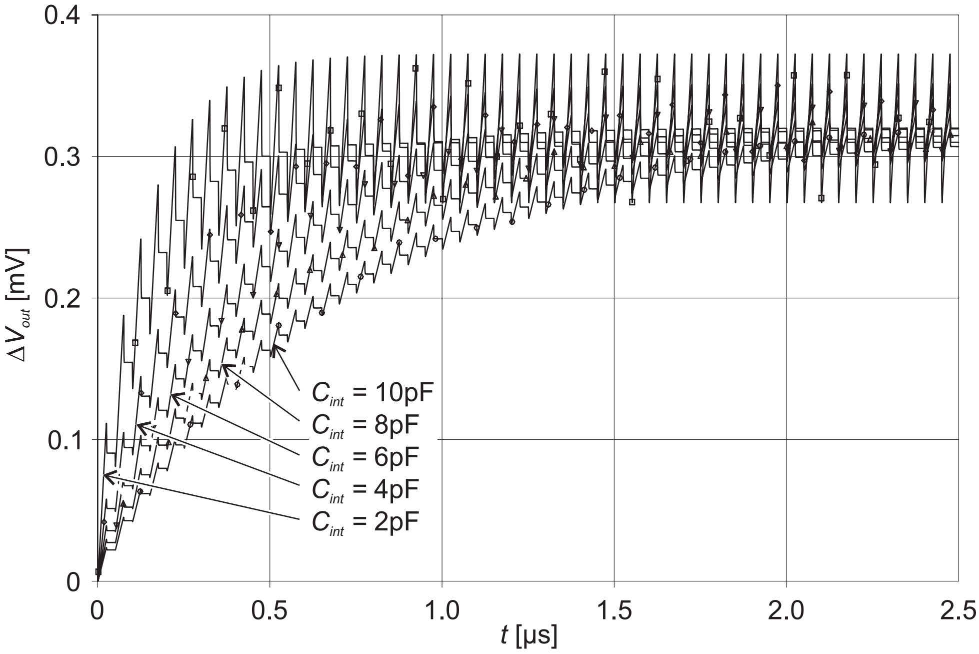

Figure 6.6 Simulated output voltages ΔV_{out} depending on the integration capacitance C_{int} with C_{pd} = 170fF, t_{delay} = 0s, f_{mod} = 20MHz, I_{pd} = 10nA

The dependence of ΔV_{out} on the photodiode size, represented by the photodiode capacitance C_{pd} is shown in Figure 6.8. In this case the maximum reachable output voltage depends on C_{pd}. In detail it is inversely proportional to C_{pd}, whereas the voltage ripple is constant.

Also the time to reach the steady-state output value is inversely proportional to C_{pd}. This can be seen as an indication that for low-capacitance photodetectors, the charge accumulation process is more effective. Therefore more optical energy is processed until the final value is reached, leading to a better overall performance of the pixel. The minimum size of the photodetector is limited by the capability of the receiving optics to focus the optical power into the small detector.

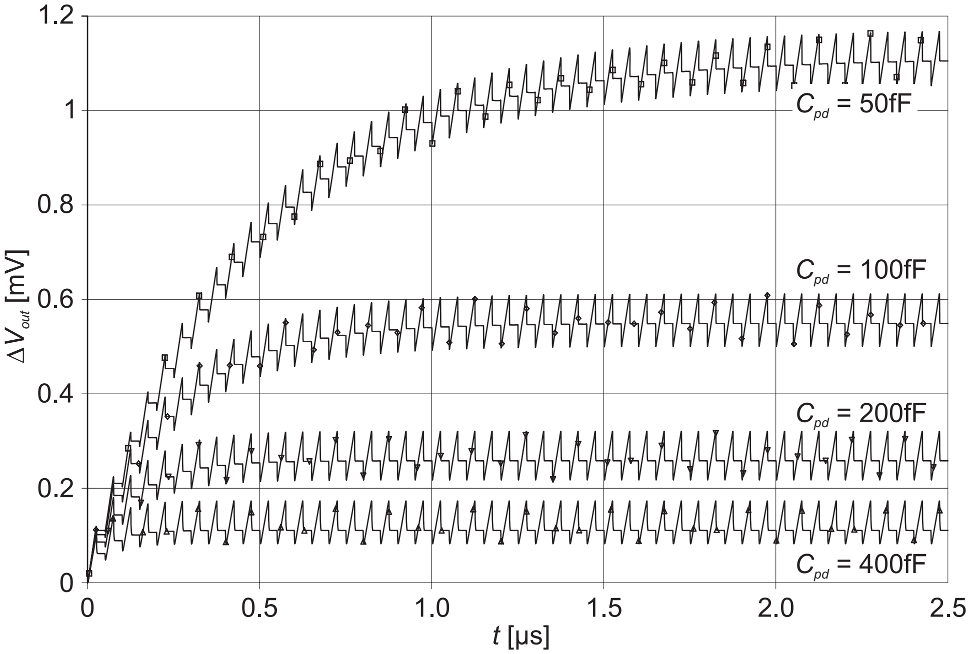

Figure 6.7 Simulated output voltages ΔV_{out} depending on the photodiode capacitance C_{pd} with C_{int} = 2pF, t_{delay} = 0s, f_{mod} = 20MHz, I_{pd} = 10nA

Finally the modulation frequency f_{mod} is stepped from 5MHz up to 40MHz. The behaviour of the output voltages ΔV_{out} depending on f_{mod} shown in Figure 6.8 is comparable to the one shown in Figure 6.7 for different photodiode capacitances C_{pd}. The achievable output voltage ΔV_{out} and the settling time t_{final} increase with decreasing frequency. Therefore the correlation sensitivity η_{sen} can be enhanced by decreasing C_{pd} and decreasing f_{mod}.

The voltage ripple increases with decreasing frequency. Therefore the ratio of phase-dependent DC output signal to high-frequent distortion does not improve by reducing f_{mod}. Due to the extension of the unambiguous range and therefore the measurement range, by decreasing f_{mod} the correlation sensitivity η_{sen} increases at the cost of decreasing phase sensitivity. Also the minimum achievable standard deviation σ_d determined by the photon noise increases with decreasing modulation frequency.

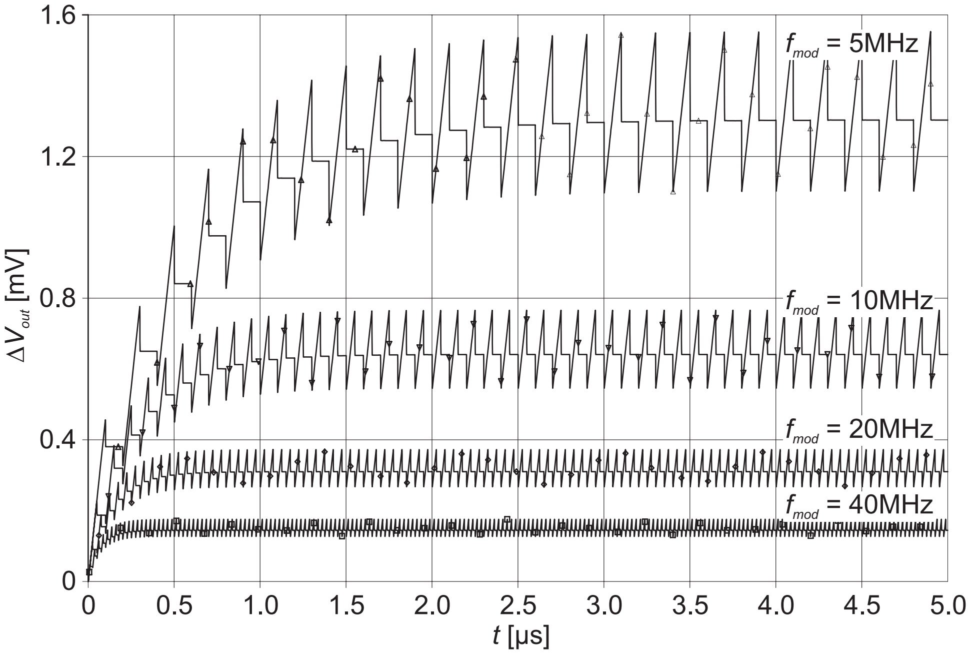

Figure 6.8 Simulated output voltages ΔV_{out} depending on the modulation frequency f_{mod} with C_{pd} = 170fF, C_{int} = 2pF, t_{delay} = 0s, I_{pd} = 10nA

Putting it all together the low-frequent behaviour of the switched bridge-correlator circuit can be expressed by the empirically derived equation (6.2) with the output voltage ΔV_{out}, the phase-shift φ between modulation voltage V_{mod} and I_{pd}, the amplitude of the photocurrent I_{pd} without background light, the modulation frequency f_{mod}, the photodiode capacitance C_{pd}, the integration capacitor C_{int}, the time t and two constants k_1 and k_2.

$$\Delta V_{out}(t) = \frac{\frac{\pi}{2} - \varphi}{2\pi} \frac{k_1 I_{pd}}{f_{mod} C_{pd}} \left(1 - e^{-k_2 \frac{f_{mod} C_{pd}}{C_{int}} t}\right) \qquad 0 < \varphi < \pi \qquad (6.2)$$

By using Matlab software for curve fitting the parameter k_2 is determined to be approximately $k_2 = 4$. Since k_2 only determines the time constant of the transient response it is not relevant for the overall system performance and therefore will not be analyzed in more detail furtheron.

The more important factor k_1 directly determines the correlation sensitivity η_{sen} of the circuit. If a constant output noise level is assumed then the knowledge of η_{sen} is sufficient to determine the minimal detectable optical power. Performing again curve fitting on the simulation results leads to (6.3). The factor 4 in the numerator of (6.3) simply compensates for the attenuation due to the first term of eq. (6.2).

$$k_1 = \frac{4}{2\pi\sqrt{2}} \qquad (6.3)$$

By inserting the fitted parameter values for k_1 and k_2 the low-frequent behaviour of the switched bridge-correlator circuit is described very well by (6.2). For the same input parameters used for the simulations of Figure 6.5−Figure 6.8 the output voltages ΔV_{out} are calculated. The results are shown in Figure 6.9. The calculated values of ΔV_{out} match with the simulated ones neglecting the voltage ripple.

From the comparison of calculated and simulated voltages the validity of eq. (6.2) is stated under the assumption of neglecting the parasitic capacitances C_{par1} and C_{par2}. This is valid because the parasitics simply lower the maximum reachable correlation sensitivity but do not influence the principle behaviour of the circuit. Out of this a model to describe the functionality concerning the low-frequent transient behaviour is given by (6.2).

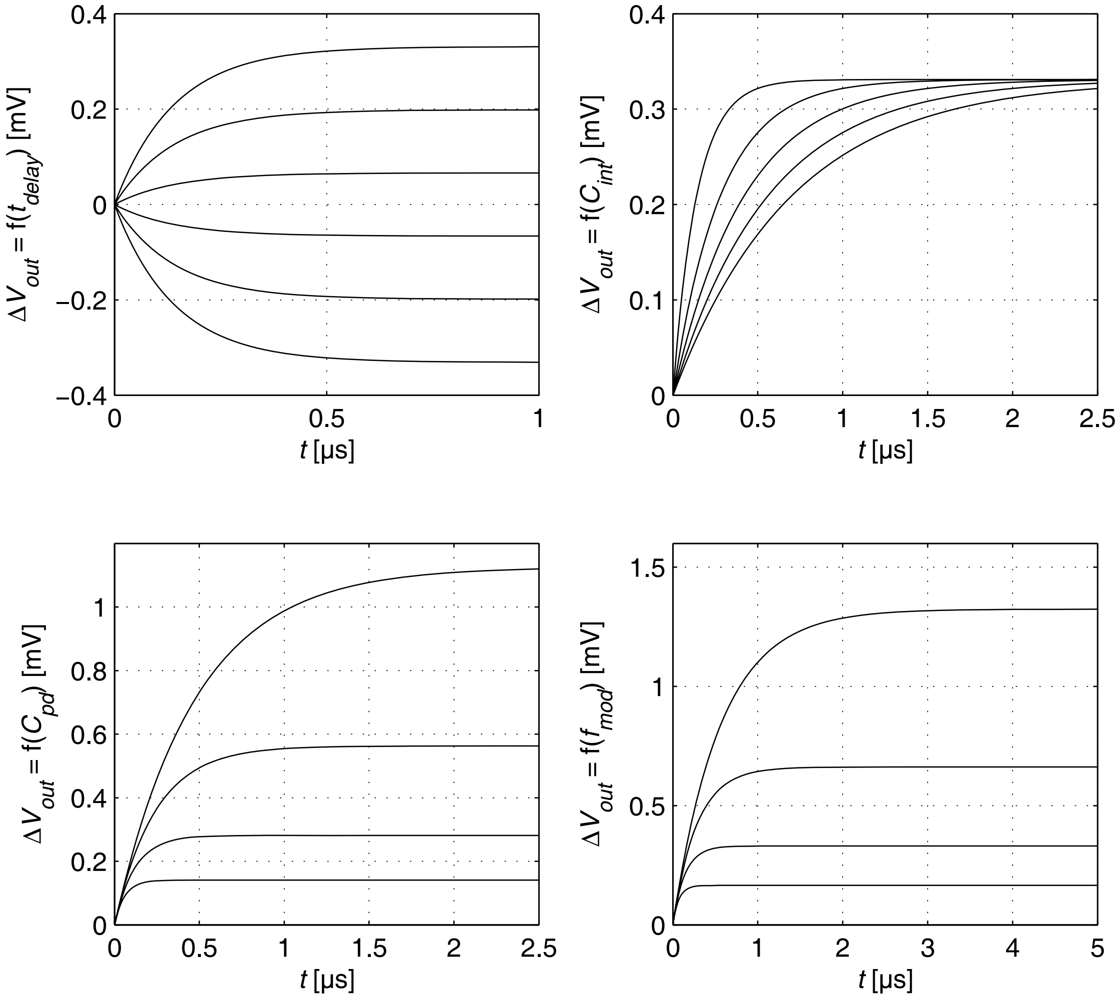

Figure 6.9 Calculated output voltages ΔV_{out} for the switched bridge-correlator circuit

By using the terms of the denominator of k_2 eq. (6.2) can be rewritten to (6.4) with the impedance of the photodiode Z_{pd} at the modulation frequency f_{mod}. From (6.4) the very interesting conclusion that the maximum achievable correlation sensitivity η_{sen} is only determined by the impedance of the photodiode can be drawn.

$$\Delta V_{out}(t) = \frac{\pi - 2\varphi}{\pi}\frac{I_{pd}}{\sqrt{2}}\frac{1}{2\pi f_{mod} C_{pd}}\left(1 - e^{-k_2 \frac{f_{mod} C_{pd}}{C_{int}} t}\right) = \left(1 - \frac{2\varphi}{\pi}\right)\frac{I_{pd}}{\sqrt{2}} Z_{pd}\left(1 - e^{-k_2 \frac{2\pi}{Z_{pd} C_{int}} t}\right) \tag{6.4}$$

The direct proportional dependence of η_{sen} on Z_{pd} can be understood more clearly by analysing the circuit at the frequency f_{mod}. The situation is shown in detail in Figure 6.10. The resulting network contains only one active source, namely the current source I_{pd}. All other elements appear as passive elements at f_{mod}. The entire bridge-correlator circuit is connected in parallel with the photodiode impedance Z_{pd}.

Since no other active element is included in the circuit the voltage signal across Z_{pd} cannot exceed $I_{pd} \cdot Z_{pd}$. The DC voltage ΔV_{out} of the integration capacitance C_{int} is transformed by the switching circuit to the frequency f_{mod}. Out of this a square-wave voltage signal having the frequency f_{mod} and the amplitude ΔV_{out} is applied from C_{int} to Z_{pd}. Since the voltage ΔV_{out} is caused by I_{pd} meaning that no voltage can be generated by C_{int} also this voltage is limited by $I_{pd} \cdot Z_{pd}$. Due to the use of square-wave signals an additional coefficient of approximately $1/\sqrt{2}$ has to be considered.

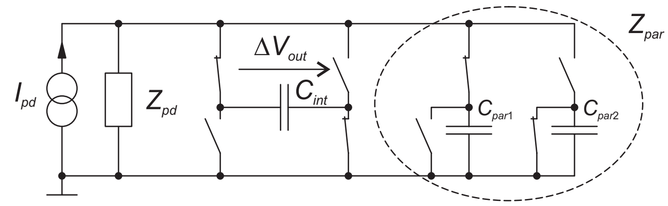

Figure 6.10 Switched bridge-correlator circuit at modulation frequency f_{mod}

Taking the parasitic capacitances C_{par1} and C_{par2} again into account as indicated in Figure 6.10 it can be seen that always one capacitance is connected in parallel with Z_{pd} whereas the other one is discharged by a switch. The influence of the parasitics is therefore similar to an increased photodiode capacitance C_{pd}.

Extending (6.4) can be done straight forward by introducing the constant k_3 which will again be determined by simulations. The final model for the low-frequent behaviour of the switched bridge-correlator circuit neglecting the high-frequent distortions is given by eq. (6.5).

$$\Delta V_{out}(t) = \frac{\pi - 2\varphi}{\pi}\frac{I_{pd}}{\sqrt{2}}\frac{1}{2\pi f_{mod}\left(C_{pd} + k_3\left(C_{par1} + C_{par2}\right)\right)}\left(1 - e^{-k_2 \frac{f_{mod}\left(C_{pd} + k_3\left(C_{par1} + C_{par2}\right)\right)}{C_{int}} t}\right) \tag{6.5}$$

Due to the symmetrical setup of C_{int}, the parasitic capacitances C_{par1} and C_{par2} are equal in size. Although they are switched inversely in time, their impact on the output voltage over one period T_p is the same. Thus they can be summarized for the model to the total parasitic capacitance C_{par} as stated by eq. (6.6).

$$C_{par} = C_{par1} + C_{par2} \tag{6.6}$$

Performing a final simulation on the bridge-correlator circuit including all elements leads to the results depicted in Figure 6.11. The results are comparable to the one with varying photodiode capacitance C_{pd} shown in Figure 6.7. The maximum output voltage decreases with increasing parasitic capacitance. The same applies for the rise time of ΔV_{out}.

For the optimal case of very small values of C_{par} the voltage curve approaches the one, only determined by the included photodiode capacitance C_{pd}. For values of C_{par} exceeding C_{pd}, the behaviour of the output voltage is dominated by the parasitic capacitance. To reach the maximum correlation sensitivity η_{sen} large values of C_{par} should be avoided. From the short analysis it can be seen that the resulting behaviour is determined by a parallel connection of C_{pd} and C_{par} as was stated in (6.5).

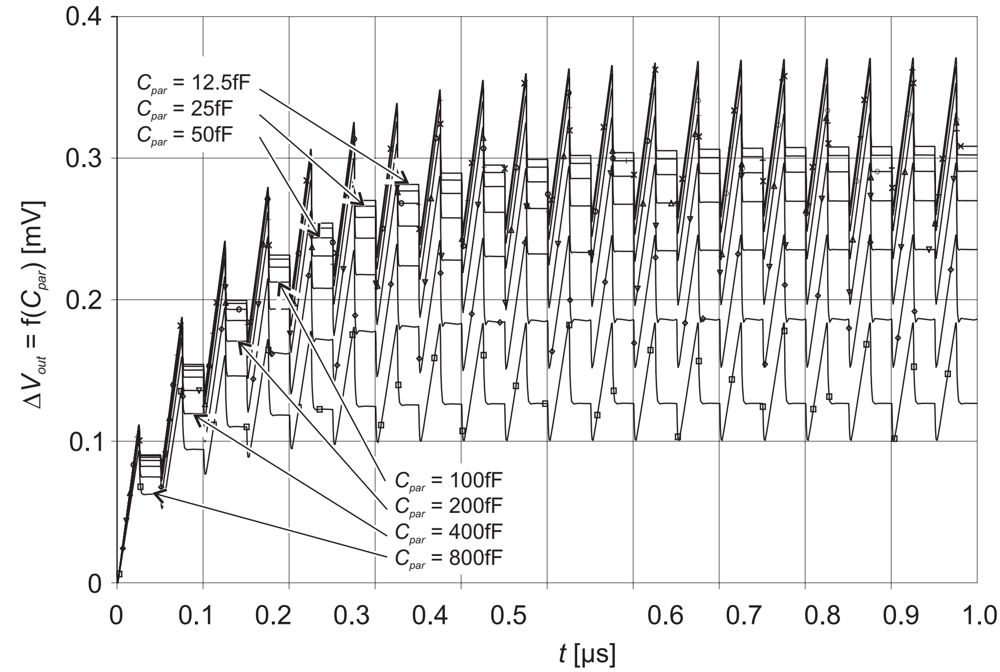

Figure 6.11 Simulated output voltages ΔV_{out} depending on the parasitic capacitance C_{par} with C_{pd} = 170fF, C_{int} = 2pF, t_{delay} = 0s, f_{mod} = 20MHz, I_{pd} = 10nA

For the same data set used to simulate ΔV_{out} of Figure 6.11, calculations have been done. By inserting the values into eq. (6.5) and adjusting the parameter k_3 the output voltages ΔV_{out} shown in Figure 6.12 result. The parameter k_3 is determined by curve fitting to be approximately $k_3 = 0.3$. Therefore the influence of the parasitic capacitance C_{par} on ΔV_{out} is qualitatively the same as the one of the photodiode capacitance C_{pd}, but quantitatively lower by the factor 0.3. From the output voltages of Figure 6.12 it can be seen that the calculated values fit to the simulated ones of Figure 6.11. Thus eq. (6.5) describes the low-frequent behaviour of the switched bridge-correlator circuit.

The model can be used to calculate the maximum achievable overall performance of a distance measurement system. Starting from the transmitted optical power, the attenuation due to the optical setup can be calculated using (3.2). Based on the received optical power and the photodiode responsivity R the photocurrent I_{pd} is calculated. As final result the signal dependent output voltages ΔV_{out} are determined. Since the noise contribution of the correlator circuit due to the mixed-signal setup cannot be simulated it has to be estimated by the designer as a first guess or directly measured at a test structure.

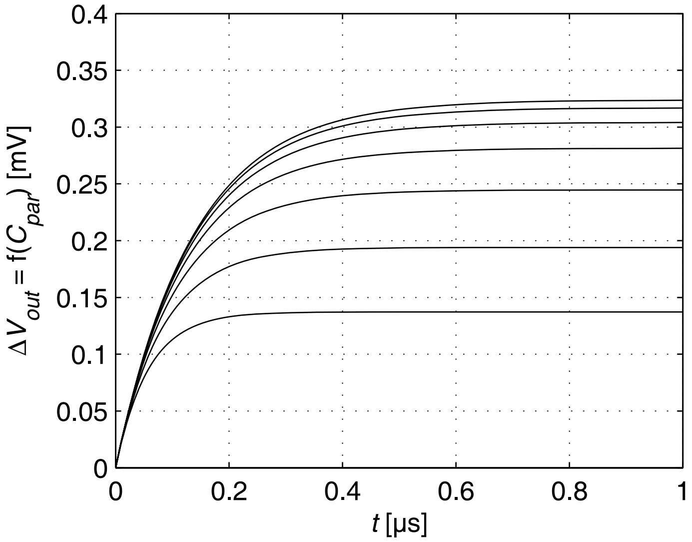

Figure 6.12 Calculated output voltages ΔV_{out} depending on the parasitic capacitance C_{par} with C_{pd} = 170fF, C_{int} = 2pF, t_{delay} = 0s, f_{mod} = 20MHz, I_{pd} = 10nA

Time consuming simulations from the system designer's point of view are necessary only to investigate the influence of further parasitic effects, such as e.g. the behaviour of the CMOS switches.

The effects of charge injection due to the gate-source C_{GS} and gate-drain C_{GD} capacitances of the CMOS switches have been investigated in detail during the actual circuit design. The main influence is an additional high-frequent distortion of ΔV_{out} having the frequency f_{mod}. Various charge compensation schemes to suppress clock feedthrough have been tested. Almost no improvement on the low-frequent behaviour of the circuit could be shown using compensation methods. Having a closer look on the critical node N_1 in Figure 6.13 shows that all switches are compensated by the symmetric circuit structure itself.

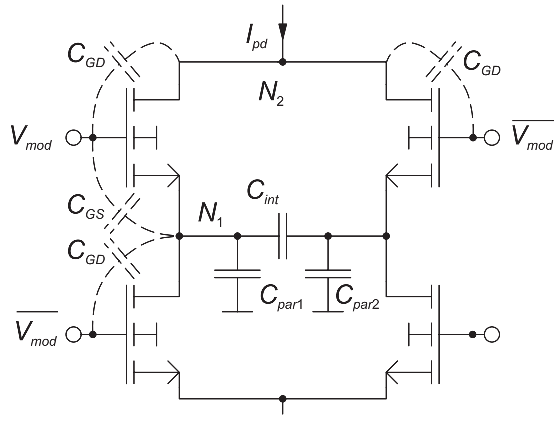

Figure 6.13 Charge injection caused by CMOS switches

The charge injection from the upper transistor to the node N_1 during a change of V_{mod} from low to high is $Q_{inj} = V_{mod} \cdot C_{GS}$. At the same time the gate voltage of the lower transistor changes from high to low. Thus the charge $Q_{inj} = -V_{mod} \cdot C_{GD}$ is injected to N_1. For small transistors C_{GS} and C_{GD} differ approximately 5% according to simulations. Therefore only a small net charge injection to node N_1 occurs. The same situation applies to the node N_2.

Out of this the optimal switch design is to use minimal CMOS transistors. The reason for this is to minimise the gate-source C_{GS} and gate-drain C_{GD} capacitances and to maximise the optical fill factor η_{fill} of the pixel.

6.1.3 Measurement Results

To test the bridge-correlator circuit the measurement setup shown in Figure 5.9 is used. Two design series of the bridge-correlator circuit have been realised to demonstrate the distance measurement capability of the bridge concept. The *first-silicon OEIC* consists of a PIN photodiode having a diameter of d_{pd} = 50µm and an integration capacitance of C_{int} = 10pF [48], [49], [50]. The *redesigned OEICs of the second series* contain photodetectors having a diameter of d_{pd} = 100µm and two different sizes of integration capacitances, namely C_{int} = 2pF and C_{int} = 10pF.

In the first step it will be focused on the *first-silicon OEIC* having the smaller photodiode. The IC was fabricated in a modified 0.6µm BiCMOS technology including poly-poly capacitors. The ratio of parasitic to nominal capacitance of poly-poly capacitors in this technology is approximately 1/13. Therefore the total parasitic capacitance of C_{int} = 10pF is C_{par} = 770fF. The modulation frequency was chosen to be f_{mod} = 9.72MHz. Due to the small size of the PIN photodiode the parasitic photodiode capacitance is only C_{pd} = 60fF. Using (6.5) to calculate the minimum and maximum final steady-state output values of ΔV_{out} it is possible to determine the correlation sensitivity η_{sen} of the bridge-correlator circuit. The correlation sensitivity is the most important number to compare the effectiveness of different circuit concepts. The main drawback of this number is that it neglects any noise components introduced by the circuit itself. For the bridge-correlator circuit η_{sen} is given by eq. (6.7).

$$\eta_{sen} = \frac{2}{\sqrt{2}\,2\pi f_{mod}\left(C_{pd} + 0.3C_{par}\right)} \tag{6.7}$$

Inserting the device values of the first-silicon OEIC into (6.7) leads to a correlation sensitivity of η_{sen} = 79.5kΩ. This value is low compared to correlation sensitivity of the high-speed circuit introduced in chapter 5 of η_{sen} = 8.2MΩ, but it has to be kept in mind that the switched-correlator circuit is completely passive. Therefore it can be used for multi-pixel arrays. To increase η_{sen} an external instrumentation amplifier having a gain of 10 is used for the actual distance measurements. This results in a total correlation sensitivity of η_{sen} = 795kΩ. The external amplifier also performs low-pass filtering of the output signal ΔV_{out} to suppress the high-frequent distortions caused by the modulation signal V_{mod}. The main advantage compared to the high-speed readout circuit is the almost perfect background light suppression capability of the bridge-correlator circuit.

The correlation sensitivity of the *first-silicon bridge-correlator* in combination with the external amplifier is 10 times lower than η_{sen} of the high-speed readout circuit. Nevertheless it is also capable of measuring distances in the range of $s_d = 0.1\text{m}-3.7\text{m}$. This is due to the fact that the noise contribution of the bridge-correlator circuit is much lower. The reason for this is that no noisy active high-speed amplification stage is necessary prior to the correlator stage. In general pre-amplification of the high-frequent received signal should be avoided. High-frequent noise caused by the input stage is transformed to the low frequency range by the multiplication stage and further amplified by following amplifier stages. In contrast the noise contribution of a slow post-amplifier is much less resulting in an improved signal-to-noise ratio.

The single distance measurement time of the *first-silicon bridge-correlator* is $t_{measure} = 8\text{ms}$. A typical measured output voltage waveform of ΔV_{out} is shown in Figure 6.14. Within the measurement time $t_{measure}$ 18 correlation functions are recorded to suppress slowly varying distortions. The suppression of background light was tested by illuminating the object with neon lamps and halogen lamps. No change of the output signal caused by the additional illumination could be noticed. As mentioned before this is because of the cancellation of any DC current within one modulation period by the bridge-correlator structure.

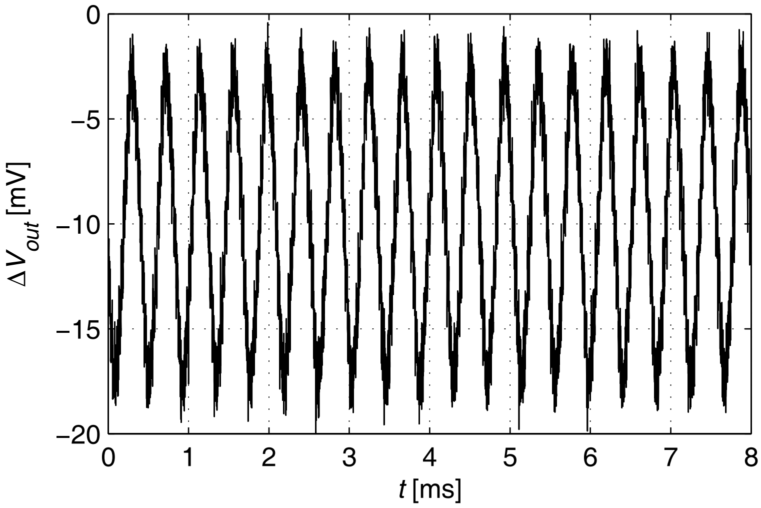

Figure 6.14 Measured output signal ΔV_{out} of the first-silicon bridge-correlator circuit

The model given by (6.5) describes beside the correlation sensitivity also the transient response of the bridge-correlator circuit. The first order time constant τ_{bc} is therefore given by (6.8).

$$\tau_{bc} = \frac{C_{int}}{4 f_{mod}\left(C_{pd} + 0.3\left(C_{par1} + C_{par2}\right)\right)} \tag{6.8}$$

Inserting the component values of the *first-silicon OEIC* leads to a time constant of $\tau_{bc} = 0.88\mu\text{s}$. Using the calculated time constant it is possible to compare the output signal of the model with a measured signal. The result is depicted in Figure 6.15. The measured signal is covered by noise having an amplitude of approximately 1mV.

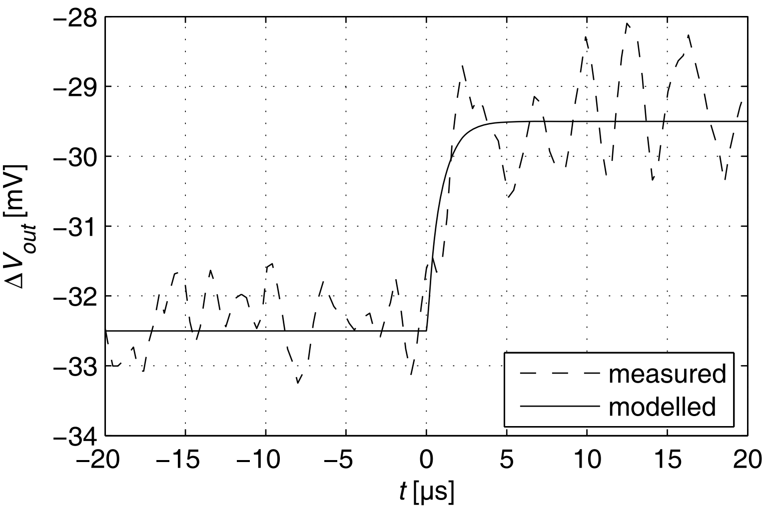

Figure 6.15 Measured and modelled output signal ΔV_{out} of the first-silicon bridge-correlator circuit

Out of this the rise time of the measured signal cannot be determined exactly. Plotting the output voltage of the model shows that both curves show the same transient behaviour. Thus the validity of the model could also be proven on an arbitrarily chosen set of output voltage values.

Distance measurements have been performed on white paper serving as diffuse reflecting object. The sampling rate of the PC based oscilloscope was set to 3MSamples/s. The bias voltage of the bridge-correlator circuit was $V_{bias} = 2\text{V}$ to meet the input voltage range of the output buffers. As illumination source serves a laser diode generating an average optical power of $P_{opt} = 2\text{mW}$ at a wavelength of $\lambda = 650\text{nm}$.

The distance measurement characteristic is shown in Figure 6.16. By mechanically adjusting the optical setup the OEIC is capable of measuring distances in the range of $s_d = 0.1\text{m}-3.7\text{m}$. Especially for short distances the coupling of the received light into the small photodiode is difficult, because the focusing capability of the receiving lens decreases with decreasing distances.

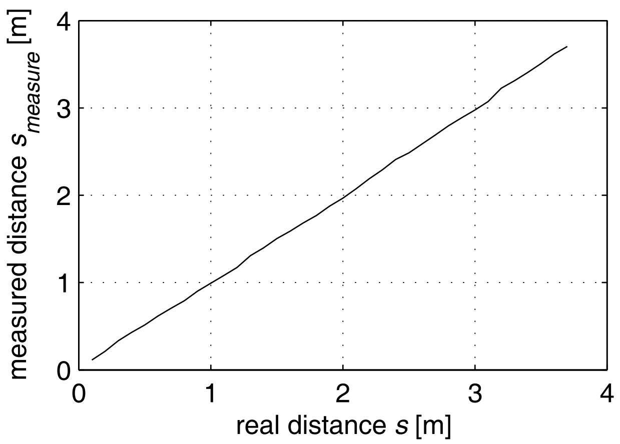

Figure 6.16 Distance measurement characteristic of the first-silicon bridge-correlator circuit, P_{opt} = 2mW

The problem of focusing the received light into the photodiode is a pure opto-mechanical problem that limits the measurement of short distances. The OEIC itself is capable of measuring also short distances since it determines the entire correlation function over the phase range of 2π for every distance measurement.

The linearity error over the entire distance range is less than $s_{lin} = \pm 3.5$cm. The measurement result determined by averaging 300 distance measurements is shown in Figure 6.17. A minimal resolution of $s_{res} = 5$cm determined by the measurements at 3.1m and 3.2m is reached.

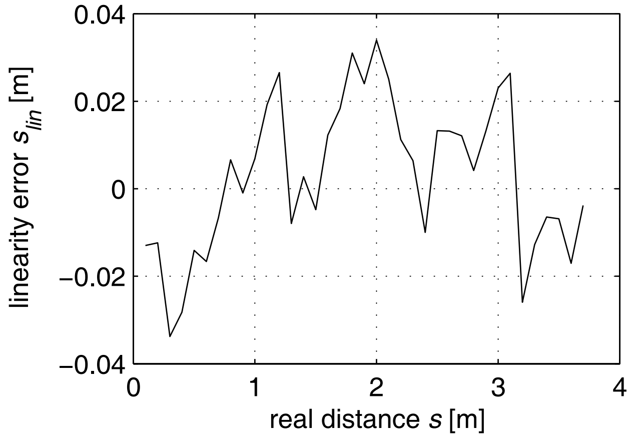

Figure 6.17 Linearity error of the first-silicon bridge-correlator circuit, P_{opt} = 2mW

The standard deviation depicted in Figure 6.18 is better than $\sigma_d = 2.7$cm over the full distance measurement range. It decreases for shorter distance values down to $\sigma_d = 0.18$cm for the optimal distance range around $s = 0.5$m. For object distances less than 0.3m the standard deviation increases again due to the bad optical setup. This is due to the fact that only a small part of the received optical power P_{opt} is focused into the PIN photodiode. In practice short distance measurements can easily be avoided by mounting the sensor at least 30cm away from the closest object distance to be measured. This is equivalent to shifting the entire distance measurement range s_d to larger distances.

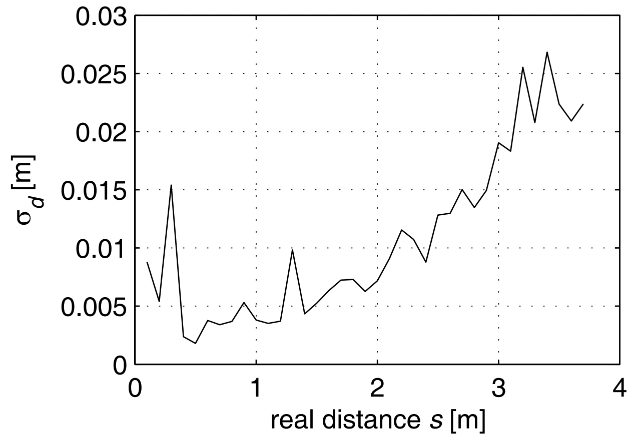

Figure 6.18 Standard deviation of the first-silicon bridge-correlator circuit, P_{opt} = 2mW

To overcome the problem of the large focus spot caused by the receiving optics a *redesign* of the bridge-correlator circuit has been done. The *second-generation OEIC* contains a PIN photodiode having a diameter of $d_{pd} = 100\mu m$. Resulting from the increased active area also the photodiode capacitance increased up to $C_{pd} = 170fF$. Furtheron different values of the integration capacitor $C_{int} = 2pF$ and $C_{int} = 10pF$ have been implemented. To reduce the parasitic capacitance of C_{int} the substrate below the capacitor was depleted to increase the correlation sensitivity η_{sen}. The resulting parasitic capacitance is approximately 1/40 of C_{int}. Using again the model of (6.5) it is possible to calculate the correlation sensitivity η_{sen} and the time constant τ_{bc} also for the redesigned OEICs. The calculated values are shown in Table 6.1.

C_{int}		C_{par}	η_{sen}	τ_{bc}
pF		fF	kΩ	µs
2	standard	154	54	0,12
10	standard	769	29	0,32
2	reduced	50	63	0,14
10	reduced	250	47	0,52

Table 6.1 Calculated values of the correlation sensitivity η_{sen} and the time constant τ_{bc} of redesigned bridge-correlator with $f_{mod} = 19.44MHz$

Compared to the first-silicon design it can be seen that the correlation sensitivity η_{sen} for the redesigned OEICs is lower than for the first-silicon one. There are two reasons for this. The first one is the increased photodiode capacitance C_{pd} due to the larger photodiode. The second one dates from the increased modulation frequency of $f_{mod} = 19.44MHz$. The frequency has been doubled to shorten the unambiguous range to $s_{unamb} = 7.7m$ and therefore to double the phase sensitivity of the overall system. To compensate for the lower correlation sensitivity an on-chip differential amplifier having a gain of 100 was implemented.

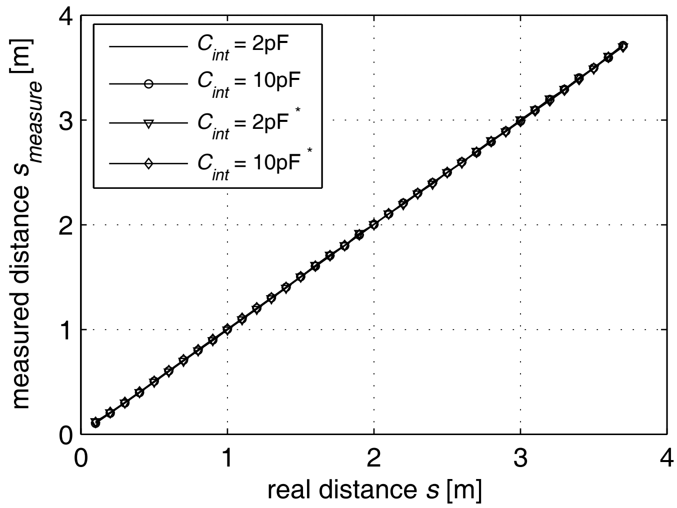

Figure 6.19 Distance measurement characteristic of the redesigned bridge-correlator circuit, * reduced parasitic capacitance, $f_{mod} = 19.44MHz$, $P_{opt} = 1.5mW$

The distance measurement characteristics of the redesigned OEICs are shown in Figure 6.19. Due to the increased photodetector area the coupling into the photodiode is more efficient. Out of this the transmitted optical power could be decreased down to P_{opt} = 1.5mW for the distance measurements. As diffuse reflecting object white paper is used. Also the measurement time was lowered from $t_{measure}$ = 8ms of the first-silicon OEIC down to $t_{measure}$ = 2ms of the redesigned bridge-correlator circuit.

Having a closer look at the resulting linearity error s_{lin} depicted in Figure 6.20 indicates that the error could be reduced down to $s_{lin} = \pm 2$cm. Due to the higher modulation frequency of f_{mod} = 19.44MHz the phase can only be shifted by $N = 8$ steps by the CPLD. As was shown in Figure 3.7 using only $N = 8$ phase steps causes a non-negligible systematic linearity error of 2cm at f_{mod} = 10MHz. By using a modulation frequency of f_{mod} = 19.44MHz this results in a systematic error of 1cm. This error is already corrected in Figure 6.20.

Regarding the linearity error s_{lin} depending on different values and types of the integration capacitor C_{int} the performance of all redesigned circuits is similar.

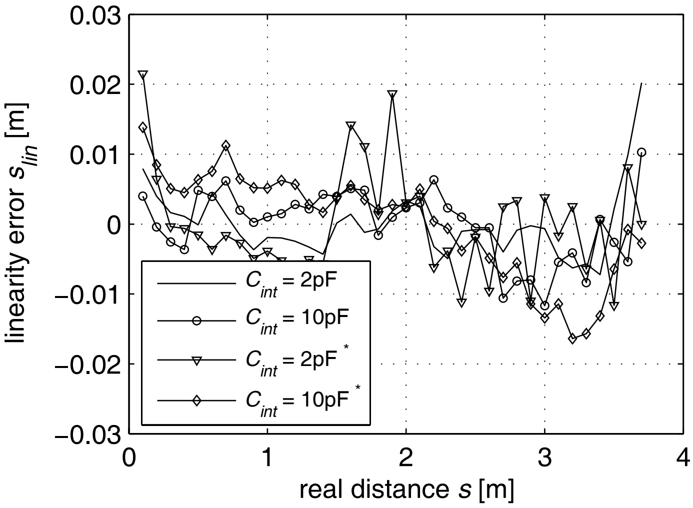

Figure 6.20 Corrected linearity error of the redesigned bridge-correlator circuit, * reduced parasitic capacitance, f_{mod} = 19.44MHz, P_{opt} = 1.5mW

The main influence on the circuit performance caused by different types and values of the integration capacitor C_{int} can be seen by the standard deviation σ_d. The standard deviation shown in Figure 6.21 was determined by measuring 50 distance measurement points at every distance.

For the standard capacitor of C_{int} = 10pF, the standard deviation is even worse than for the first-silicon OEIC because the photodiode capacitance C_{pd} was increased, whereas the transmitted optical power P_{opt} was decreased at the same time. This bad combination of parameter changes led to a maximum standard deviation of σ_d = 4.8cm. For the other integration capacitors the standard deviation could be improved compared to the first results. In detail the maximum standard deviations at s = 3.7m is σ_d = 2.4cm for C_{int} = 2pF. For the reduced parasitic capacitances, the standard deviation further decreases to σ_d = 2.3cm for C_{int} = 10pF and σ_d = 2.0cm for C_{int} = 2pF.

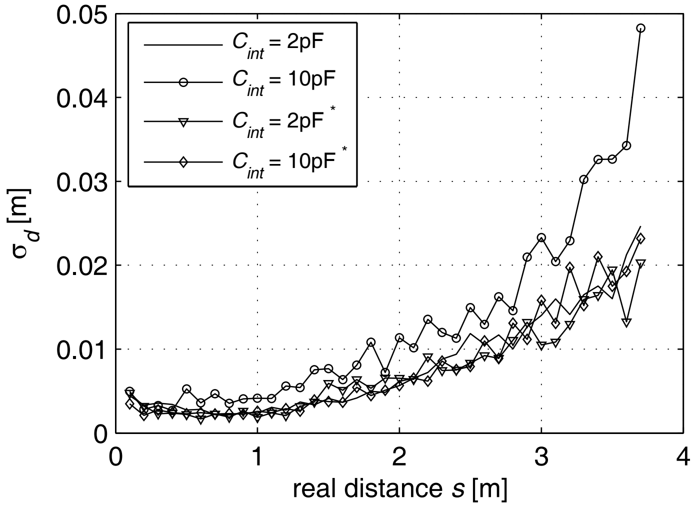

Figure 6.21 Standard deviation of the redesigned bridge-correlator circuit, * reduced parasitic capacitance, f_{mod} = 19.44MHz, P_{opt} = 1.5mW

Out of this it can be seen that reducing the parasitic capacitance C_{par} helps to improve the system performance. Further improvement could be done by implementing photodiodes having a considerably lower photodiode capacitance C_{pd}.

The OEICs were fabricated in the same 0.6µm BiCMOS technology as the high-speed readout circuit introduced in chapter 5. The main functional components are highlighted in the chip photograph shown in Figure 6.22. These are the PIN photodiode A, the clock driver stage B, the switched bridge-correlator network C, the integration capacitance D and the differential output amplifier E having a gain of 100. Furtheron blocking capacitors for the supply voltages and ESD protection structures for the PIN photodiode can be seen. The area consumption of the blocks ACDE necessary in every pixel is $250 \times 200 \mu m^2$. The fill factor is $\eta_{fill} = 16\%$. By reducing the area of the amplifier E the fill factor can be increased in future designs.

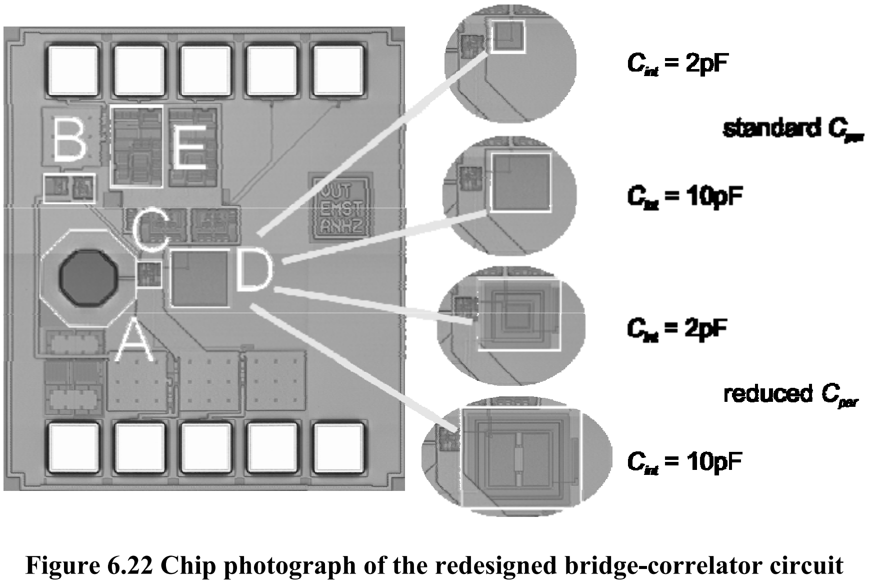

Figure 6.22 Chip photograph of the redesigned bridge-correlator circuit

6.2 Enhanced-Sensitivity PIN Bridge-Correlator Circuit with Active Amplifier

In the detailed analysis of the passive bridge-correlator circuit in chapter 6.1 it can be seen that the integration capability of the circuit is limited. Two dominating sources causing this non-perfect behaviour are identified. These are the photodiode capacitance C_{pd} and the parasitic capacitance C_{par} of the integration capacitor. If an entire passive circuitry is of fundamental importance only the use of low-capacitance photodiodes helps to improve the correlation sensitivity η_{sen} considerably. The use of integration capacitors with reduced parasitic capacitance did not show the desired effect. If an active circuitry is possible, considerable improvements can be achieved as is described in the following.

6.2.1 Operating principle

A common way to improve switched-capacitor designs regarding parasitic capacitances is not to minimize the parasitics, but to eliminate their influence on the circuit by virtually eliminating them at all. For the photodiode capacitance C_{pd} this means that any photocurrent flow into C_{pd} has to be avoided. From eq. (6.9) it can be seen that no current flow into C_{pd} means, that the photodiode voltage V_{pd} has to be constant.

$$V_{pd}\left(t_1\right) = V_{pd}\left(t_0\right) + \frac{1}{C_{pd}} \int_{t_0}^{t_1} I_c dt = V_{pd}\left(t_0\right) + \frac{1}{C_{pd}} \int_{t_0}^{t_1} 0 dt = V_{pd}\left(t_0\right) \tag{6.9}$$

This can also be interpreted as a decoupling of the photodiode and the readout circuit. The newly developed *third-generation OEIC* based on the bridge-correlator circuit performs exactly this operation. The voltage across the photodiode is kept constant by connecting the photodiode to the input terminal of an amplifier. The circuitry is shown in Figure 6.23. The bridge-correlator circuit is placed in the feedback path of the amplifier similar to an ordinary integrator circuit.

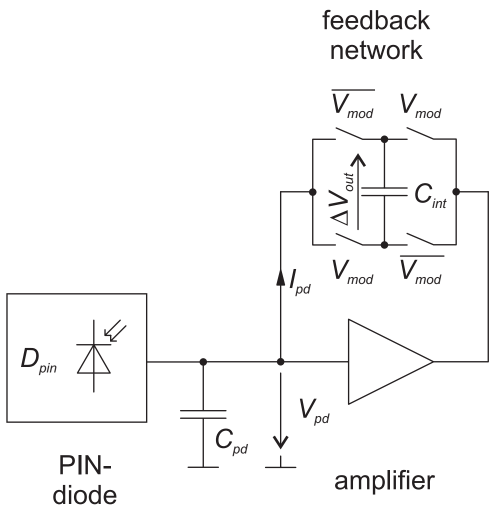

Figure 6.23 Amplifier-supported switched bridge-correlator circuit

The bandwidth of the amplifier f_{3db} has to be higher than the modulation frequency to compensate the photodiode capacitance C_{pd} for the received signal at the frequency f_{mod}. If the influence of C_{pd} is eliminated, again only one signal path for I_{pd} at the frequency f_{mod} is available. Out of this I_{pd} is again forced through the bridge-correlator circuit. Now the integration capacitor C_{int} is charged by the received optical current to the output voltage ΔV_{out}. The influence of C_{pd} theoretically is eliminated by using an amplifier having a gain of $A_{amp} = \infty$. Since the voltage across C_{pd} is constant, the voltage at the amplifier output has to vary. The amplitude of the square-wave signal at the amplifier output is exactly $|\Delta V_{out}|$. This can easily be seen by setting V_{mod} to low. In this case the output of the amplifier has to be $V_{pd}+\Delta V_{out}$. Setting V_{mod} to high leads to $V_{pd}-\Delta V_{out}$. Therefore the second requirement on the amplifier is that the slew rate is high enough to compensate C_{pd} even for large output signal levels of ΔV_{out}.

Simulations have been performed on the improved circuit structure. All simulations performed so far have been done using the same initial operating point. A more convenient way to simulate the circuit behaviour is to use a set of pulsed current sources for the photocurrent I_{pd}, which are turned on and off in a sequential way. Out of this the entire correlation functions for $N = 8$ phase steps is simulated, avoiding any initial transient process in between. The results for photocurrents in the range of I_{pd} = 1nA−100nA are shown in Figure 6.24.

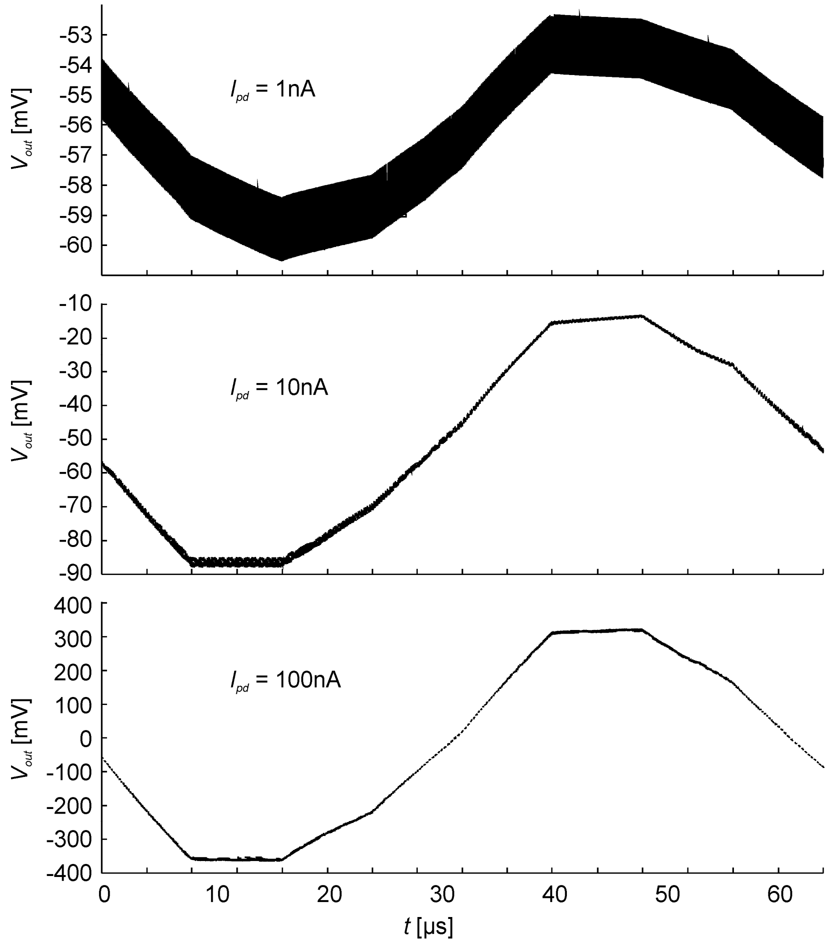

Figure 6.24 Simulated output voltages ΔV_{out} for different input signal levels

From the piecewise straight lines it can be seen that the circuit integrates the photocurrent. No saturation effects occur for an integration time of a single step of t_{step} = 8µs. The pure integrating behaviour is also shown by the reached output voltages. For the signal input current I_{pd} = 10nA the maximum output voltage difference is ΔV_{out} = 80mV. Having again a look on Figure 6.7 shows that even for the redesigned bridge-correlator circuit a maximum output voltage change of ΔV_{out} = ±1.2mV is expected. The reachable output voltage of this new third-generation OEIC is determined only by the time t_{step} and can reach large values also for small input current levels.

An upper limit for the output voltage ΔV_{out} is given by the amplifier output voltage range. The amplification factor of most amplifiers decreases when the output voltage approaches the output voltage limits. Therefore especially for large-signal current I_{pd} nonlinear behaviour of the circuit is expected. This effect can be avoided by adjusting the integration time for large input signal levels.

Comparing the output voltages for I_{pd} = 100nA and I_{pd} = 10nA shows that the waveforms are exactly the same except for the difference in amplitude by a factor of ten. The output waveform for I_{pd} = 1nA is depicted as a thick line. This indicates that the voltage signal is covered by a distortion having the frequency f_{mod}. Since the amplitude of the distortion does not vary for different input current levels it is caused by the circuit itself. In detail the distortion dates from the switching of the bridge-correlator. During the switching time of approximately 1ns the amplifier sees a strongly varying load in the feedback path.

Furtheron it can be noticed that the second segment of the first output wave has a negative slope, whereas the two other waveforms are almost horizontal during the time interval t = 8µs−16µs. This negative slope dates from a slow initial transient response of the system, which could not be eliminated during simulations. This transient response is also included in the two other waveforms, but the influence cannot be seen due to the larger amplitude of the output voltages.

6.2.2 Measurement Results

Measurements have been performed using the same optical setup as for the redesigned bridge-correlator circuit. Due to the higher sensitivity of the circuit, no adjustments on the optical setup have been made throughout the measurement. This is an important difference to the measurement performed so far, because the variation of the optical received power is considerably larger. The transmitted optical power was set to be only P_{opt} = 1mW. The movement of the object is controlled by a linear motor system.

A typical measured output voltage waveform is shown in Figure 6.25. The differential output voltage of the OEIC is amplified by a factor of 10 by using an external differential to single-ended instrumentation amplifier. By having a look on Figure 6.14 it can be seen that the original bridge-correlator circuit reached a maximum output voltage change of approximately ΔV_{out} = 15mV also by using an external amplifier. The third-generation OEIC reaches an output voltage of ΔV_{out} = 500mV, which is limited by the time of a single phase step of t_{step} = 210µs. Therefore a sensitivity enhancement of at least factor 30 is reached. Keeping in mind that the optical transmitted power has been reduced and the coupling into the photodiode is not optimized the enhancement is even higher.

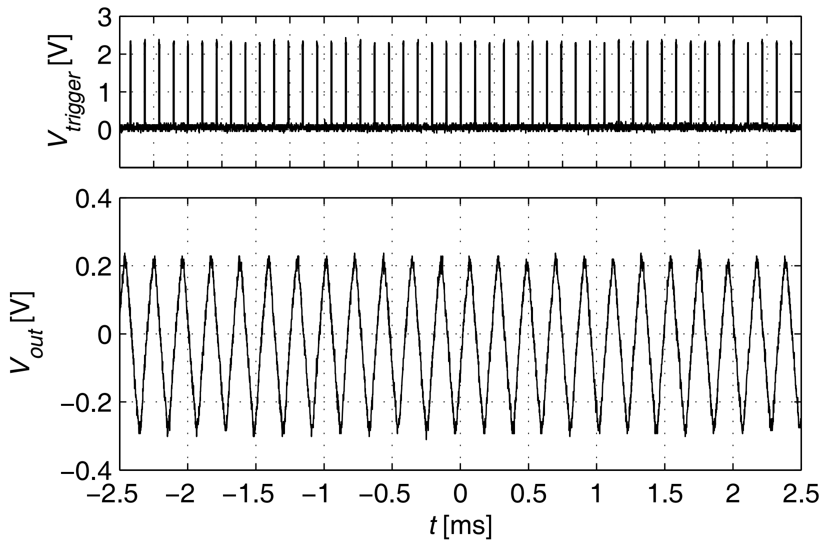

Figure 6.25 Measured output voltage V_{out} of the enhanced-sensitivity PIN bridge-correlator circuit

For a single distance measurement 23 triangle correlation functions are recorded. The single distance measurement time is $t_{measure} = 5\text{ms}$, which is comparable to former results.

The distance measurement characteristics of the OEIC shown in Figure 6.26 is determined by measuring 60 distance values for every object distance. The measurement range is limited to $s_d = 0.7\text{m}{-}3.4\text{m}$ because no adjusting of the optical setup is performed. Therefore especially for short object distances only a small portion of the receivable optical power is focused into the PIN photodiode. To be able to receive light for every object distance it was necessary to defocus the laser beam at the diffuse reflecting object surface. Therefore also the spot diameter at the PIN photodiode increases and is larger than the photodiode area of $A_{pd} = 75\times125\mu\text{m}^2$. This results in an attenuated received optical power for all object distances.

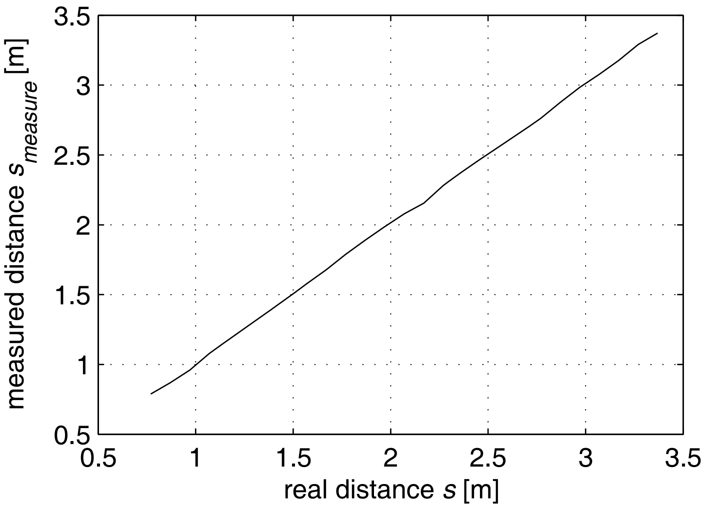

Figure 6.26 Measurement characteristic of the enhanced-sensitivity PIN bridge-correlator circuit

From the distance measurement characteristics the linearity error s_{lin} of the OEIC is determined. The result depicted in Figure 6.27 shows a maximum deviation from the real distance s of $s_{lin} = \pm 2$cm. Since the linearity error is completely random and does not depend on the intensity of the received optical signal it cannot be corrected. The reason for the relatively large error compared to the high output signal amplitude is not known yet. Nevertheless the linearity error with reduced transmitted optical power of $P_{opt} = 1$mW is equal to the linearity error s_{lin} of the second-generation OEIC.

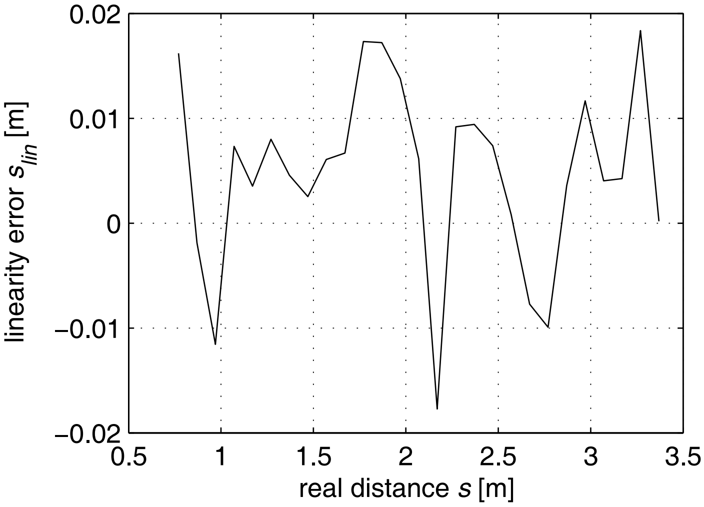

Figure 6.27 Linearity error s_{lin} of the enhanced-sensitivity PIN bridge-correlator circuit

A real improvement in terms of improved distance measurement capability can be seen from the achieved standard deviation σ_d shown in Figure 6.28. The maximum standard deviation determined from 60 measurement values is less than $\sigma_d = 14$mm for a single distance measurement time of $t_{measure} = 5$ms. It decreases from large distances towards $s = 1.6$m and increases for smaller object distances because of the poor focus capability of the optical setup which has not been modified during the entire measurement.

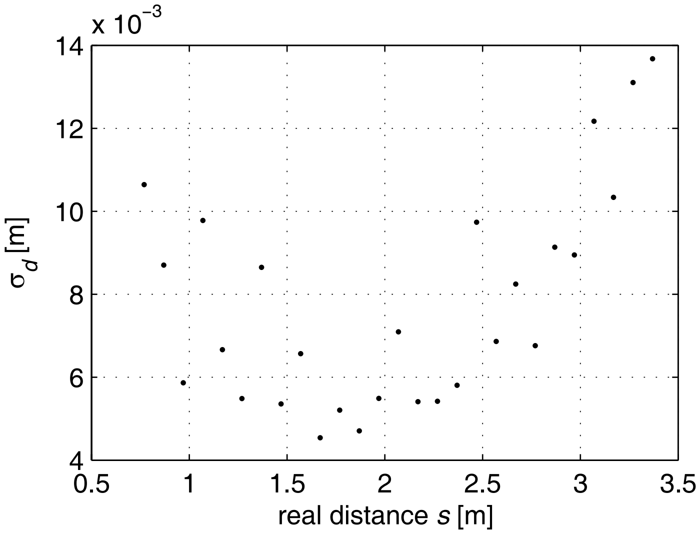

Figure 6.28 Standard deviation σ_d of the enhanced-sensitivity PIN bridge-correlator circuit

The third-generation bridge-correlator circuit was built in a modified 0.6µm BiCMOS technology, similar to the technology used for the original bridge-correlator circuit. Also this technology includes a PIN module to build fast integrated optical detectors. The chip photograph of the OEIC is shown in Figure 6.29. The relevant functional blocks are the clock-driver stage A, the rectangular PIN photodiode B, the readout circuit C including the bridge-correlator circuit and the amplifier and finally two output voltage buffers D to drive the measurement equipment. Furtheron blocking capacitors to buffer and stabilise the power supply can be seen.

For a multi-pixel design only the blocks B and C are necessary in every pixel. The total pixel area consisting of these two blocks is $A_{pixel} = 85{\times}180\mu m^2$. The optical active photodiode area is $A_{pd} = 75{\times}125\mu m^2$. Therefore a very high optical fill factor of $\eta_{fill} = 61\%$ is reached. The entire OEIC is connected to a voltage supply having an output voltage of 5V.

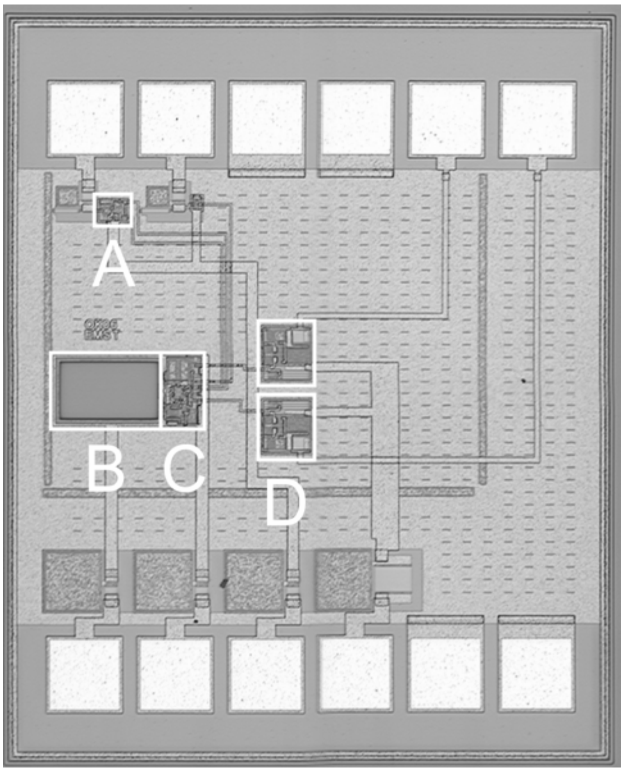

Figure 6.29 Chip photograph of the third-generation PIN bridge-correlator circuit

6.3 Single-Sided Modulated Double-Anode Receiver

Both distance measurement OEICs, the active high-speed readout circuit and the passive switched bridge-correlator circuit, use a fast integrated PIN photodiode to transform the received optical signal P_{opt} into an electrical current signal I_{pd}. The actual correlation is performed by the readout circuit.

The single-sided modulated double-anode receiver presented in [53] uses a so-called double-anode photodetector to detect and directly correlate the optical received signal. This highly sensitive OEIC is capable of measuring distances within a range of $s_d = 0.1\text{m}-15\text{m}$. A single distance measurement time of only $t_{measure} = 5\text{ms}$ is necessary to obtain a measurement value at $s = 15\text{m}$. Comparing this total acquisition time to the time-of-flight of an ultrasound sensor of $t_{tof} = 87\text{ms}$ demonstrates the fast measurement capability of the OEIC.

The setup of the single-sided modulated double-anode receiver is shown in Figure 6.30. The main functional components are the DAP device, the active transimpedance stage, the output low-pass filter and the voltage buffer to drive the external measurement equipment.

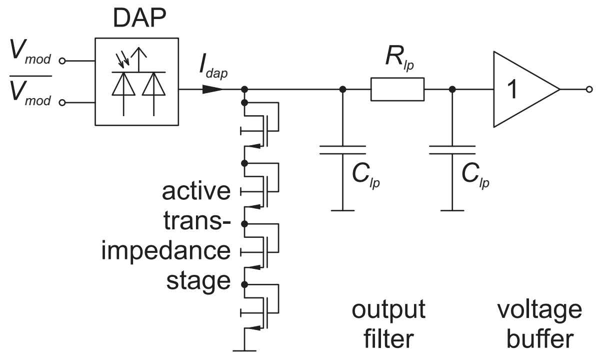

Figure 6.30 Setup of single-sided modulated double-anode receiver

The OEIC operates in the following way. The received optical power P_{opt} is correlated with the modulation signal V_{mod} by the DAP device. The output current of the DAP is fed to a chain of diode-connected MOS transistors, forming a large current-dependent resistor. To suppress high-frequent distortions of the output signal caused by the modulation voltage a low-pass filter network is connected in parallel to the active transimpedance stage. Since the output voltage is determined only by the very small photocurrent any current flow from outside has to be avoided. Therefore a high-impedance voltage buffer is necessary to decouple the circuit from the surrounding circuitry.

The detailed operating principle of the DAP is explained in chapter 4.3. The separation effect of the DAP relies on the lateral electrical field between the two anodes. The direction of the field can be changed by switching the anode voltages in opposite way. The same effect is reached by supplying one anode with the modulation voltage having twice the amplitude and keeping the other anode at a constant voltage. The situation is shown in Figure 6.31.

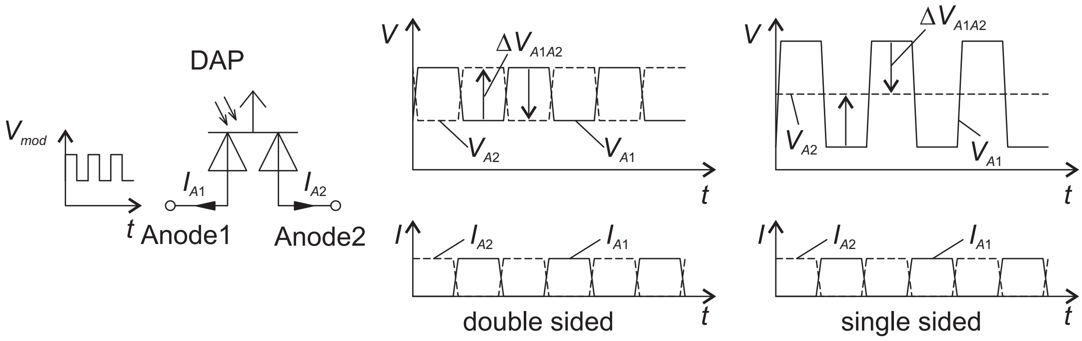

Figure 6.31 Result of different modulation concepts for the DAP device

By modulating only anode 1 it is possible to readout a low-frequent amplitude and phase proportional output current at the anode 2. This signal current can directly be processed by the transimpedance stage. The large-signal modulation voltage V_{mod} having an amplitude in the range of some Volts does not appear at anode 2. Therefore a large, area consuming low-pass filter network to suppress the modulation voltage V_{mod} as it was used for a first-silicon OEIC presented in [52] is not necessary anymore.

The modulation voltage V_{mod} is generated by the clock driver stage. The functional principle of the clock driver is shown in Figure 6.32. It is built up as three-stage architecture. The first stage consisting of a single inverter is used to recondition the input signal. It raises the voltage level of the digital signal up to 5V and decreases the rise time and fall time. The second stage contains another inverter and a transfer gate to generate an inverted and a non-inverted output signal with a phase-shift of 180° in between. The third stage acts as an output buffer to avoid any feedback from the DAP device to the transfer gate. Furtheron it is used to set the modulation voltage level. This is done by supplying the output inverters with the variable voltage $V_{mod,high}$.

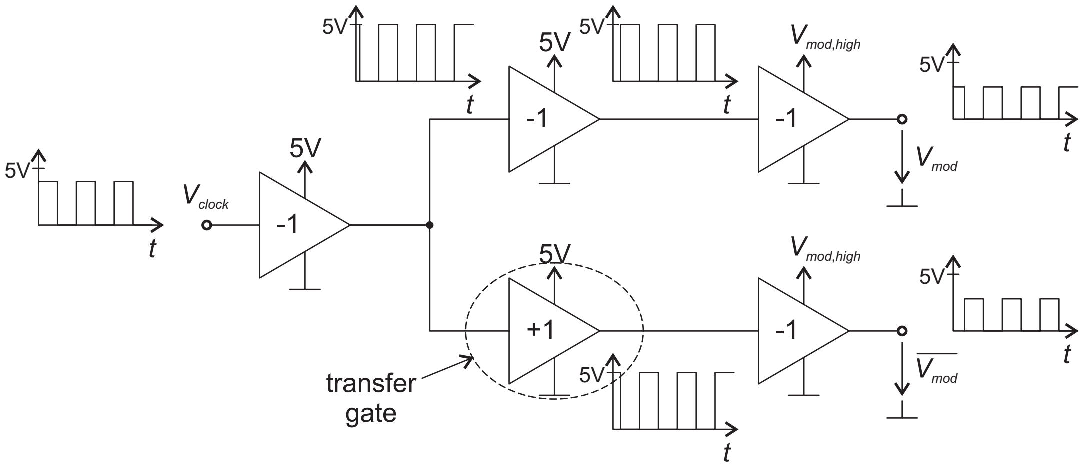

Figure 6.32 Clock driver stage for the single-sided modulated DAP device

Although the large-signal voltage V_{mod} can be avoided at anode 2, still distortions having the frequency f_{mod} appear in the output signal. They date from the capacitive coupling of the modulation voltage from anode 1 to anode 2.

Having a closer look on the equivalent circuit of the DAP depicted in Figure 4.13 shows that the coupling capacitance C_{A1A2} between the anodes can cause an AC current flow from anode 1 to anode 2.

The realized OEIC contains a DAP of the size $A_{pd} = 100\times100\mu m^2$. Due to the four times larger photodetector area also the parasitic capacitance values increase. They are approximately three times larger than for the smaller DAP of the size $A_{pd} = 50\times50\mu m^2$ resulting in $C_{CA1} = C_{CA2} = 90fF$ and $C_{A1A2} = 50fF$. The modulation voltage V_{mod} is switched by the on-chip clock driver stage between 0V and 3.1V within $t_{rise} = 1ns$. Using this information the current flow through C_{A1A2} is given by (6.10). The current into anode 2 is of block type. Therefore a 1ns long and 155µA strong current pulse occurs during the rise of V_{mod}. Exactly the same current pulse with negative sign occurs during the fall of V_{mod}.

$$I_{A1A2} = C_{A1A2}\frac{dU_{A1A2}}{dt} = C_{A1A2}\frac{\Delta U_{A1A2}}{\Delta t} = 50\text{fF}\frac{3.1\text{V}}{1\text{ns}} = 155\mu\text{A} \tag{6.10}$$

Although the current through C_{A1A2} is a pure AC current it has to be compensated. This is due to the fact that the actual photocurrent lying in the range of nA is approximately 10^5 times lower than the coupling current I_{A1A2} during switching. Since the capacitance cannot be avoided the optimal way to compensate the coupling effect is to inject the same amount of charges with negative sign at the same time into the node A2. The circuitry performing this operation is shown in Figure 6.33. The capacitor C_{comp} having the same size as the coupling capacitance C_{A1A2} is connected to the inverted modulation signal. Out of this the charge injection is compensated. The compensation capacitor is realised as a poly-poly capacitor.

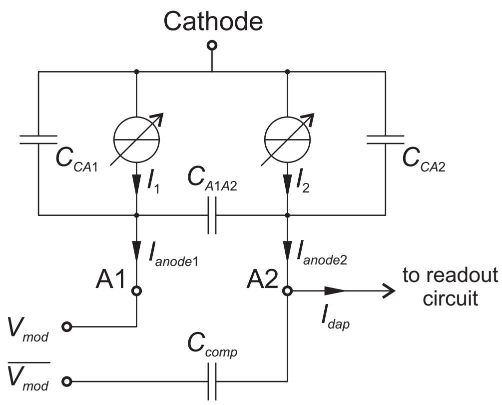

Figure 6.33 Compensation of the coupling capacitance C_{A1A2} by charge injection from the inverted modulation signal

Since the capacitance values of poly-poly capacitors vary due to technology tolerances the charge cancellation is not perfect. The charges caused by the difference of C_{comp} and C_{A1A2} still are injected to anode 2. The following transimpedance stage is capable of processing this considerable smaller amount of charges.

The resulting current from anode 2 to the readout circuit I_{dap} therefore consists of two parts. These are the correlated photocurrent having always a positive sign and a small AC current caused by the capacitance mismatch. The waveform of I_{dap} is depicted in

Figure 6.34. The DAP output current I_{dap} contains a phase-depending current of the received optical signal and exactly half of the current caused by background light. Therefore also the background light has to be processed by the readout circuit.

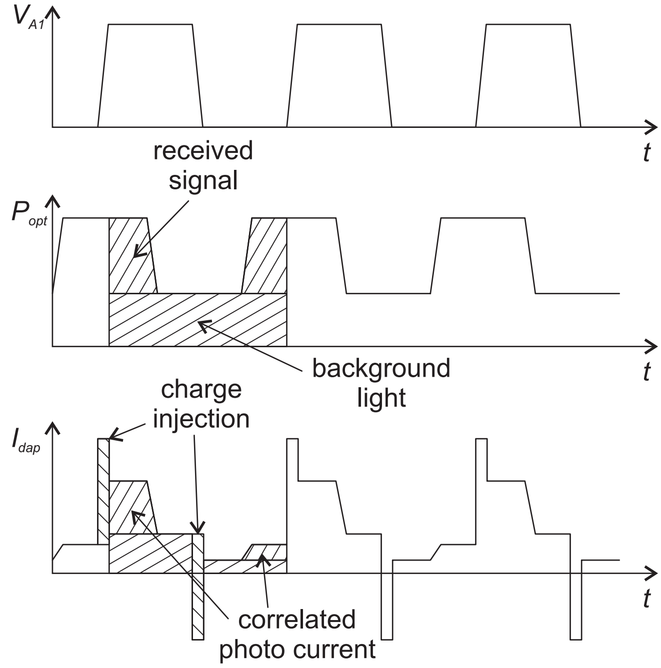

Figure 6.34 Current output waveform of single-sided modulated compensated DAP

The problem that half of the background light has to be processed by the readout circuit at every device output terminal applies to all integrated mixing photodetectors. It directly dates from the uni-polar modulation process, resulting in only positive signal output currents. This effect usually limits the dynamic range of the sensor, because any integration process of the photo-generated charges saturates faster due to the background light. Therefore the integration time has to be decreased resulting in a decreased sensitivity.

Saturation effects can be avoided by using a nonlinear resistive network to perform the current to voltage conversion. This is done by the on-chip implemented active transimpedance stage.

6.3.1 Automatic Gain Setting with Transimpedance Stage

The active transimpedance stage depicted in Figure 6.35 consists of four diode-connected NMOS transistors. It has two main functionalities. First of all it should provide a large transimpedance to transform the small photocurrent in the range of nA into measurable voltages. The second not so obvious one is to compensate the drop of the optical received power $P_{opt}(1/s^2)$ due to the increasing object distances.

From eq. (3.2) it can be seen that the received optical power decreases quadratically with increasing object distance. Therefore also the resulting photocurrent decreases quadratically. To linearise the dependency of the output voltage level on the object distance the transimpedance has to be automatically adjusted for lower input currents.

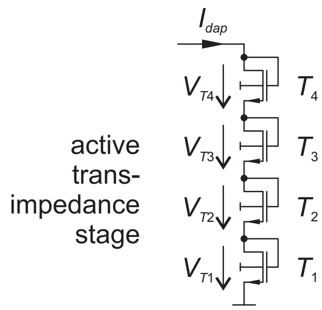

Figure 6.35 Active transimpedance stage

To derive the transimpedance of the stage let us consider the transistor T_1 only. According to [54] the DC output voltage of a diode-connected MOS transistor is given by (6.11) with the threshold voltage V_T, the saturation drain to source current I_{DSsat}, the gate width W, the gate length L and the process constant K'. For the expected very small photocurrent the transistor voltage V_{T1} is therefore approximately V_T. Neglecting the back-gate effect also the voltage across the transistors T_2–T_4 is V_T. Therefore the DC operating point of the output voltage is determined to be approximately $4 \cdot V_T$.

$$V_{GS} = V_{T1} = V_T + \sqrt{\frac{I_{DSsat}}{K' \frac{W}{L}}} \tag{6.11}$$

The total transimpedance of the stage is the sum of the reciprocal values of the transistor transconductances g_m. (6.12).For T_1 the transimpedance Z_{T1} is given by (6.13) around the DC operating point of I_{DS0}. Again neglecting the back-gate effect the total transimpedance is approximately $4 \cdot Z_{T1}$.

$$g_m = \left. \frac{dI_{DS}}{dV_{GS}} \right|_{I_{DS} = I_{DS0}} \tag{6.12}$$

$$Z_{T1} = \frac{1}{g_m} = \frac{1}{2} \sqrt{\frac{L}{K'W} \frac{1}{I_{DS0}}} \tag{6.13}$$

Since the separation efficiency η_{sep} of the DAP device is in the range of 50% always an additional bias current caused by the received light flows through the transimpedance stage. The situation is illustrated in detail in Figure 6.34. This signal dependent current and the current caused by background light determine the bias current I_{DS0}. The correlated signal current is always smaller than I_{DS0} and is treated as small-signal current.

Simulations have been performed on the presented structure to determine the transimpedance of the circuit. The results depicted in Figure 6.36 show the transimpedance depending on I_{DS0} of the transistor T_1, the combination of T_1+T_2, T_1+T_2+T_3 and the total transimpedance T_1+T_2+T_3+T_4. For the interesting measurement range of 0.1nA up to 100nA the total transimpedance decreases from Z_{tot} = 2.1GΩ down to Z_{tot} = 3.2MΩ.

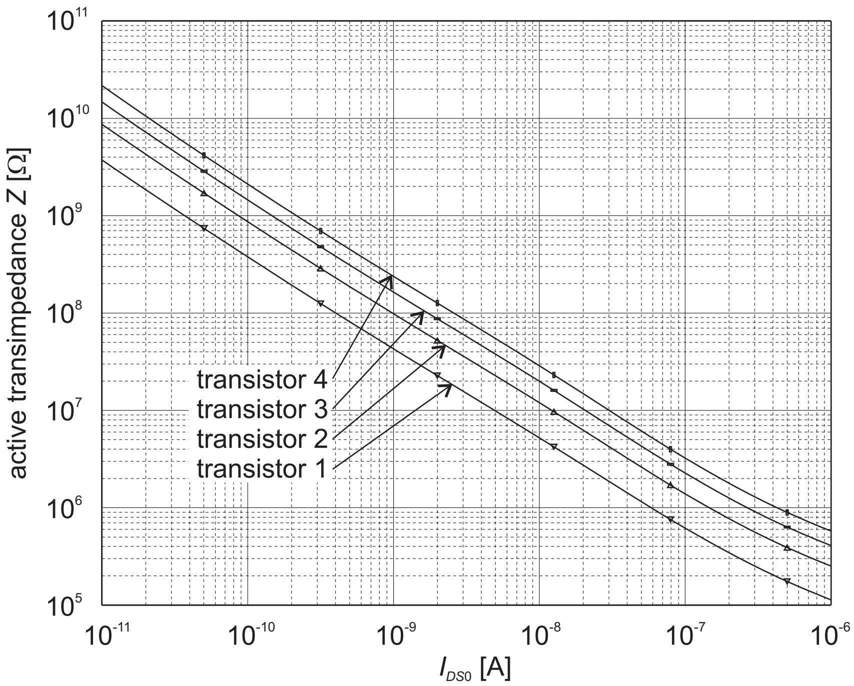

Figure 6.36 Simulated low frequency transimpedance, depending on the DC bias current I_{DS0}

This decrease is approximately indirect proportional to the current I_{DS0} and not as stated by (6.13) by the square root of I_{DS0}. The reason for this effect is that (6.13) is only valid down to currents in the range of µA. The expected photocurrent of an optical distance measurement system is approximately 1000 times smaller. The exact value of the total transimpedance Z_{tot} is given by the empirically derived eq. (6.14).

$$Z_{tot} = \frac{0.77\Omega}{\sqrt[1.06]{\dfrac{I_{DS0}}{1\text{A}}}} \tag{6.14}$$

By using the current-dependent transimpedance it is possible to determine the interrelationship of the amplitude of the output voltage and the object distance. To demonstrate the intended circuit functionality background light is neglected in a first step. Therefore I_{DS0} determining the total transimpedance is only given by the signal proportional current I_{ph}.

The step by step derivation is shown in (6.15). The optical received power P_{opt} decreases quadratically with increasing distance. The photocurrent is proportional to the received optical signal and therefore also decreases quadratically with increasing object distance. The total transimpedance increases with decreasing bias current I_{DS0} according to eq. (6.14). Therefore it increases by the power of 1.88 with increasing distance. Thus the resulting output voltage V_{out}, determined by the multiplication of the total transimpedance and the photocurrent, depends on the object distance by $s^{-0.12}$ instead of s^{-2}. This means that the output voltage V_{out} is therefore almost independent of the object distance and the received signal level.

$$P_{opt} \sim \frac{1}{s^2} \rightarrow I_{ph} \sim \frac{1}{s^2} \rightarrow Z_{tot} \sim \frac{1}{\sqrt[1.06]{I_{DS0}}} \sim \left(\frac{I_{ph}}{\eta_{sen}}\right)^{-\frac{1}{1.06}} \sim s^{1.88} \rightarrow V_{out} \sim Z_{tot} I_{ph} \sim \frac{s^{1.88}}{s^2} = s^{-0.12} \quad (6.15)$$

Therefore theoretically a change of the received optical signal by a factor of 1000 is mapped onto a change of the output voltage of only 57%. In practice two main distortions occur. The first one is the noise contribution to the signal because of the large transimpedance of the stage which increases for smaller input currents.

The second one is the nonlinear distortion caused by background light. As soon as the background light is considerably higher than the received optical signal, it determines the bias current I_{DS0} through the transimpedance stage. When this is the case the transimpedance Z_{tot} is determined only by the background light and it becomes independent of the received signal. Out of this the output voltage and therefore the sensitivity of the circuit decrease with decreasing received optical power. Therefore background light should be filtered away before entering the photodetector.

Furtheron only small changes around the bias current I_{DS0} are allowed to maintain linearity of the circuit for the recording of an entire correlation function. The functionality of the transimpedance stage relies on the fact that the direction of the current flow is always positive. A negative current cannot be processed by the diode-connected MOS transistors. Therefore negative currents have to be prevented to flow into the transimpedance stage.

From Figure 6.34 it can be seen that the actual signal current is composed of the wanted DC current and a fraction of an AC current having the fundamental frequency of f_{mod} = 9.72MHz. This AC current is unavoidable and is caused by two different sources. One source of the occurrence of the AC current is the received optical modulated light P_{opt} itself having the frequency f_{mod}. The second source is the uni-polar modulation process of the DAP device. Due to the modulation process also a part of the received background light is transformed up to f_{mod}. Since the separation efficiency of the DAP device is around η_{sep} = 58% the average DC output current I_{DS0} is always higher than the AC current.

Only the modulated part of the received light causes a change of the output voltage depending on the phase-shift between the modulation voltage V_{mod} and P_{opt}. The DAP output current caused by background light is independent of the phase-shift of V_{mod} and simply contributes as an additional bias current to I_{DS0}. Because of the limited separation efficiency η_{sep} the change of the output current is small. Therefore the constraint that the change of the mean value of I_{dap} compared to the DC bias current I_{DS0} has to be small during recording of an entire triangle correlation function is always fulfilled.

After proving that the constraints to operate the active transimpedance stage are fulfilled under normal operating conditions, the prevention of a negative current flow into the stage has to be realized.

Having again a look on Figure 6.34 shows that the charge injection caused by the mismatch of the coupling capacitance C_{A1A2} and the compensation capacitance C_{comp} might be larger than the sum of the signal current and the current caused by background light. This results in short time periods of negative current flow from the double-anode photodetector. In detail the time period is determined by the rise time of V_{mod} and is about $t_{rise} = 1\text{ns}$. The spectrum of these short current spikes is therefore composed of high-frequent signals having frequencies exceeding 1GHz.

In eq. (6.10) an amplitude of an uncompensated current spike of $I_{A1A2} = 155\mu\text{A}$ was calculated. Relying on the technology used to fabricate the OEIC the matching of the compensation capacitance is expected to be 85%−115%. Therefore a resulting current spike of ±22µA has to be suppressed. To ensure that no negative current flow through the transimpedance stage is caused by the coupling capacitance the spike current is set to be less than 1% of the bias current I_{DS0}. This can be realised by connecting a capacitor in parallel to the transimpedance stage. The entire output low-pass filter performing exactly this operation is shown in Figure 6.37 a). To illustrate the operating principle an AC analysis of the circuit is performed as shown in Figure 6.37 b).

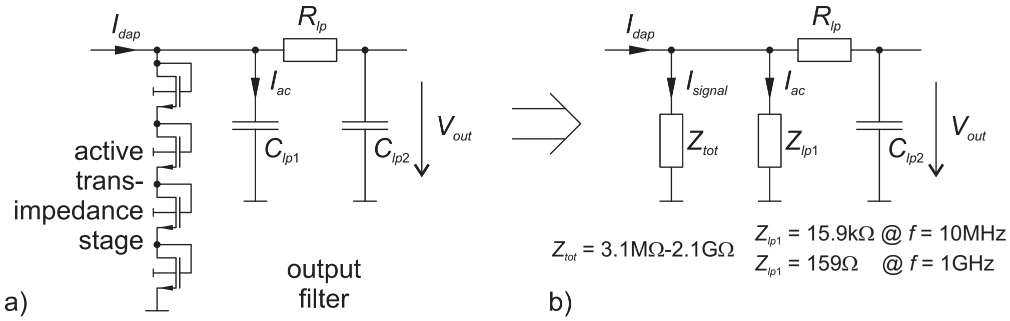

Figure 6.37 Output low-pass filter network for the active transimpedance stage

The total transimpedance Z_{tot} of the transimpedance stage is determined by the bias current I_{DS0} only. In a first design step the resistive branch is assumed to be more or less independent of the frequency. To reach a suppression of the current spikes below 1% independent of I_{DS0} also the fraction of the AC current I_{AC} through the MOS transistors has to depend on I_{DS0}. This effect is reached by the parallel connection of the current-dependent impedance Z_{tot} and the constant impedance Z_{lp1}. The smaller the bias current I_{DS0} gets, the larger the transimpedance Z_{tot} becomes and as a result the smaller the current flow dating from the charge injection through Z_{tot} is. Instead of filtering I_{AC} in the frequency domain, it is filtered in the current domain.

To dimension the capacitor C_{lp1} a bias current of $I_{DS} = 100\text{nA}$ is assumed. The total transimpedance at this point is $Z_{tot} = 3.1\text{M}\Omega$. To reach a distortion caused by the injected current of less than 1% the AC current through the transistor stack has to be less than 1nA. This means that the compensated current pulse of 22µA has to be suppressed according to (6.16) by a factor of $k_{sup} = 22000$.

$$k_{sup} = \frac{I_{AC,comp}}{I_{DS} \cdot 1\%} = \frac{22\mu\text{A}}{100\text{nA} \cdot 1\%} = 22000 \tag{6.16}$$

Based on the current divider rule therefore the capacitance C_{lp1} has to have a maximum transimpedance of $Z_{lp} = 140\Omega$. The lowest occurring frequency of the 1ns pulse is around 1GHz. Out of this the minimum capacitance value can be determined to be $C_{lp1} = 1.1\text{pF}$. The finally implemented on-chip poly-poly capacitor has a nominal value of $C_{lp1} = 1\text{pF}$.

To verify the constant suppression of the pulse current let us consider a very weak optical received signal causing a bias current of $I_{DS0} = 0.1\text{nA}$. In this case the total transimpedance is $Z_{tot} = 2.1\text{G}\Omega$. The current into the transimpedance stage dating from the charge injection is according to the current divider rule with $Z_{lp1} = 159\Omega$ $I_{AC} = 1.6\text{pA}$. Also for the minimum expected input current, the distortion caused by the modulation voltage is only slightly larger than 1%.

The same circuit behaviour is used to suppress the distortions at the modulation frequency $f_{mod} = 9.72\text{MHz}$. As was mentioned before the distortions caused by the received optical signal are always smaller than I_{DS0} because of the limited separation efficiency η_{sep} and the uni-polar modulation process of the DAP device. Therefore to reach a suppression of the distortion of better than 1% a suppression factor of $k_{sup} = 100$ for all operating points is sufficient.

Using the current divider rule for the case of maximum optical received power represented by the minimum total transimpedance of $Z_{tot} = 3.1\text{M}\Omega$ leads to a maximum impedance of $Z_{lp1} = 31\text{k}\Omega$ at a frequency of $f_{mod} = 10\text{MHz}$. Out of this the minimum capacitance to suppress all optical current caused distortions at $f_{mod} = 10\text{MHz}$ is calculated to be $C_{lp1} = 513\text{fF}$. Also this condition is fulfilled by the use of a 1pF poly-poly capacitor.

Transient simulations on the circuit performed in the time domain indicated that the suppression of the high-frequent distortions is not as good as promised by the circuit design procedure. The reason for this could not exactly be identified but one part of the problem dates from the parasitic gate-to-source capacitances C_{GS} of the MOS transistors. As shown in Figure 6.38 they form an additional capacitive path of four serial connected capacitances to ground.

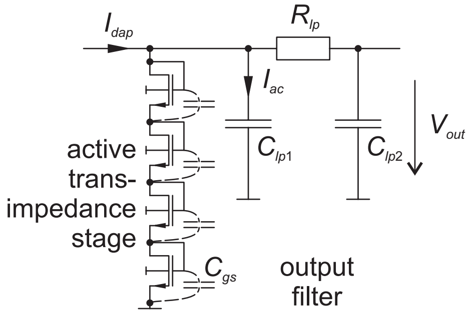

Figure 6.38 High frequency parasitic capacitances of the transimpedance stage

Therefore the resulting high-frequency transimpedance $Z_{tot,HF}$ of the transimpedance stage is given by the parallel connection of the current-dependent low frequency transimpedance $Z_{tot,LF}$ and the frequency-dependent impedance Z_{par} (6.17). The lower value of $Z_{tot,LF}$ and Z_{GS} determines the high frequency suppression. Especially for a low input current $Z_{tot,LF}$ becomes extremely high and can therefore be neglected compared to Z_{par} for high frequencies. The simulated equivalent capacitance C_{par} including C_{gs} and all parasitic capacitances to substrate for all transistors is $C_{par} = 8.3\text{fF}$. This results in a simulated bandwidth of the active transimpedance stage of $f_{3dB} = 6\text{MHz}$ for $I_{DS} = 100\text{nA}$.

$$Z_{tot,HF} = Z_{tot,LF} \| Z_{par} = \frac{Z_{tot,LF} \frac{1}{j\omega C_{par}}}{Z_{tot,LF} + \frac{1}{j\omega C_{par}}} \tag{6.17}$$

To reach still a sufficiently good suppression of the high-frequent distortions an additional voltage low-pass filter is connected to the transimpedance stage. The low-pass filter consisting of R_{lp} and C_{lp2} was designed to have a 3dB cut off frequency of f_{3dB} = 2.5MHz. Finally a voltage buffer is connected to the filter output to prevent any current flow from the surrounding circuitry into the transimpedance stage.

In the final design step transient simulations of the entire circuitry have been performed. The DAP device was simulated using the equivalent circuit shown in Figure 4.13. Especially the behaviour of the current sources had to be approximated in an optimal way, since their parameters as e.g. the separation efficiency η_{sep} depend on the modulation voltage in a nonlinear way.

A sample simulation result of the entire distance measurement OEIC is depicted in Figure 6.39. The mean value of the DAP output current was set to be I_{DS0} = 7nA. The amplitude of the phase-dependent signal current has been 3nA. From the simulation results it can be seen that an increase of the time delay t_{delay} between the modulation voltage V_{mod} and the received optical signal P_{opt} leads to an increasing negative voltage slope of the output voltage. All simulated output voltages V_{out} decrease during the entire simulation because the large capacitor C_{lp1} has to be charged by the photocurrent to reach the steady-state output value. The resulting high-frequent voltage ripple is 1mV, which is small enough for the following distance measurements. The coincidence of the voltage curves for t_{delay} = 0ns and t_{delay} = 10ns dates from the time skew of the clock driver stage (see also Figure 5.8).

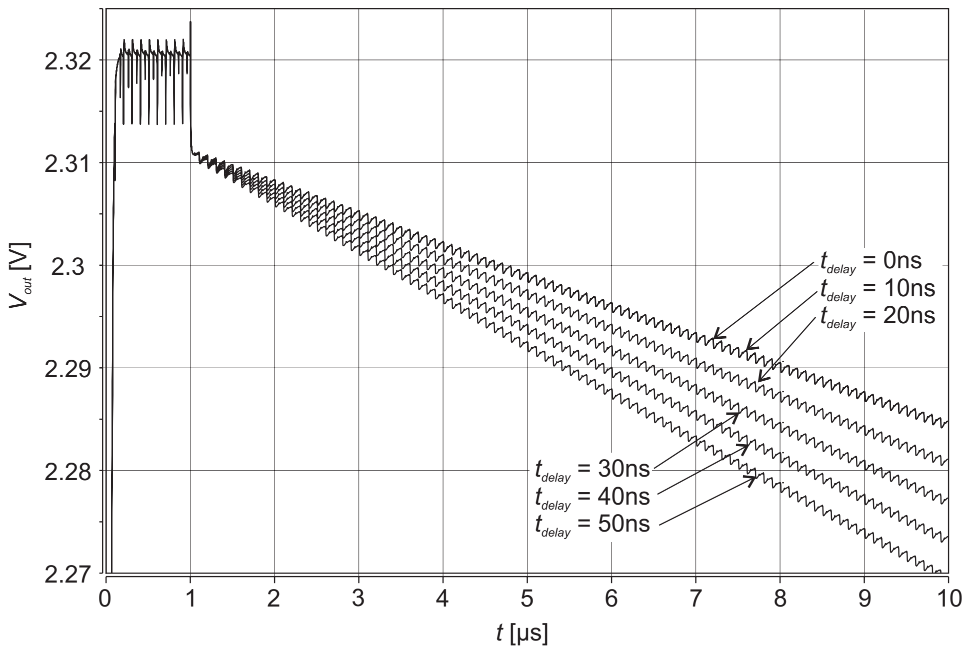

Figure 6.39 Simulation results of distance measurement OEIC with DAP device and active transimpedance stage

6.3.2 Measurement Results

All distance measurements have been performed in a laboratory environment. Background light was generated by neon lamps mounted at the laboratory ceiling. The illuminance at the diffuse reflecting object surface is 300lux. By assuming a conversion efficiency of neon lamps according to [55] of approximately 826lux/(W/m^2) this results in an optical power density at the object surface of 0.36W/m^2 in the visible wavelength range. The spot diameter of the laser-beam at the object surface is 1cm. The optical power caused by background light for this area is 28.5µW and is negligible compared to the transmitted optical power of P_{opt} = 1.6mW. It has to be kept in mind that if the field of view of the sensor increases also the received background light increases. The total measurement time for a single distance measurement is $t_{measure}$ = 5ms. White paper having a diffuse reflectivity of almost 100% served as non-cooperative object.

A typical sensor output signal recorded for an s = 8m distant object is depicted in Figure 6.40. It can be seen that 23 triangle correlation functions are acquired within the measurement time of $t_{measure}$ = 5ms. Each triangle function consists of 16 phase steps.

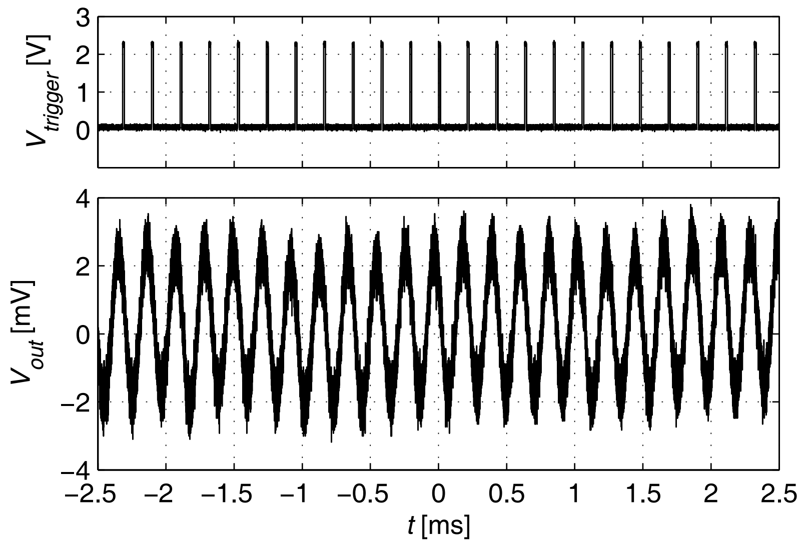

Figure 6.40 Sensor output signal for 8m distant object

From the measured output signal the sensitivity of the circuit can be derived. Therefore the received optical power is estimated under the assumption of negligible free-space attenuation and an efficiency of the receiving lens of η_{lens} = 0.7. The laser diode used to illuminate the object transmitted an optical power of $P_{opt,tra}$ = 1.6mW at a wavelength λ = 650nm. The diameter of the receiving lens is d_{lens} = 0.0254m. Inserting these values into (3.2) leads according to (6.18) to a maximum receivable optical power of $P_{opt,rec}$ = 2.8nW.

$$P_{opt,rec} = P_{opt,tra} e^{-2\beta s} \cdot \frac{A_{lens}\eta_{lens}\rho_{ref}\cos(\Phi)}{s^2\pi} = 1.6\times10^{-3}\,\mathrm{W}\frac{(0.0127\mathrm{m})^2\,\pi\cdot0.7}{(8\mathrm{m})^2\,\pi} = 2.8\mathrm{nW} \tag{6.18}$$

The responsivity of the DAP device at the wavelength of λ = 660nm is R = 0.42A/W and is only slightly different for the λ = 650nm laser source used for distance measurements. Therefore a photocurrent of $I_{ph} = 1.18\text{nA}$ is generated. The phase-dependent variation of the output signal is 5mV. Therefore a minimum correlation sensitivity of $\eta_{sen} = 4.2\cdot 10^6\text{V/A}$ is reached under the assumption of perfect coupling of the received light into the double-anode photodetector. This value must not be mixed up with the internal active transimpedance. The active transimpedance has to be much higher because it has to compensate for the non-perfect mixing capability of the DAP device, the finite extinction ratio of the laser source and the photocurrent caused by background light. The separation of all these effects cannot directly be done by measurements.

Keeping in mind that this output circuit is an all passive structure the value of η_{sen} is comparable to the one simulated for the TIA based high-speed readout circuit. The noise contribution of the circuit due to the passive setup is much less than the one of the active circuit. This can easily be seen by comparing Figure 5.16 showing a noise floor of approximately 15mV and Figure 6.40 where a noise contribution of ≈1mV can be identified.

Due to the much better signal-to-noise ratio the sensor is capable of measuring four times larger distances. The distance measurement characteristic ranging from $s_d = 0.1\text{m}-15\text{m}$ is shown in Figure 6.41. It was determined by shifting the object in 10cm steps from 15m down to 0.1m. For each object distance 100 distance measurements are averaged.

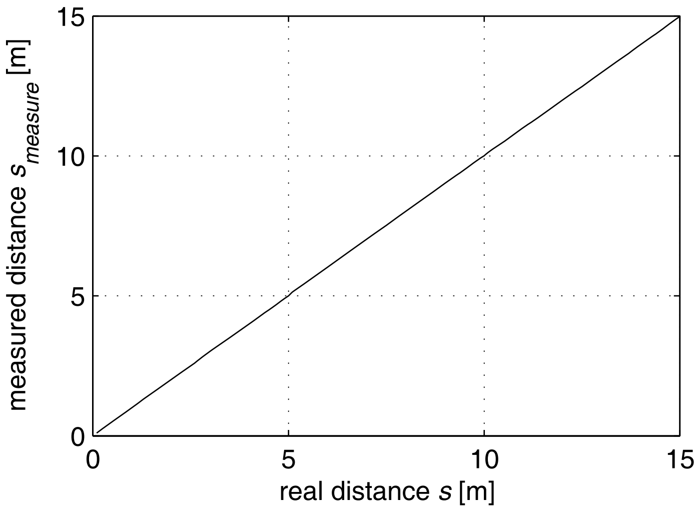

Figure 6.41 Distance measurement characteristic of the all passive DAP based sensor

From the distance measurement characteristic the linearity error s_{lin} is obtained by subtracting the measured distance from the real distance. The result is shown in Figure 6.42. The linearity error over the entire distance range is less than $s_{lin} = \pm 3.5\text{cm}$. This is according to (6.19) equal to a linearity error referred to the maximum achievable distance measurement range of ±0.23%.

$$\frac{s_{lin}}{\max(s_d)} = \frac{\pm 0.035\text{m}}{15\text{m}} = 0.23\% \tag{6.19}$$

From Figure 6.42 it can be seen that the linearity error beginning from large distance values increases almost continuously. At the object distance of s = 5m the error suddenly drops approximately by 3cm. The reason for this is that the optical setup, especially the focus had to be adjusted to couple the received optical power into the DAP device.

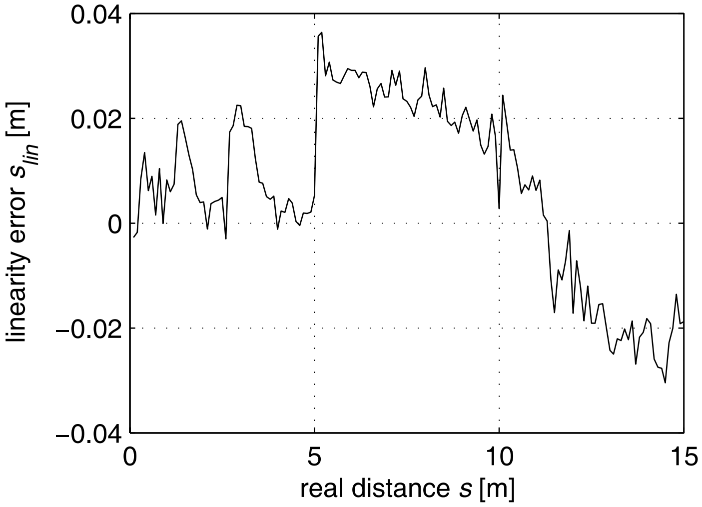

Figure 6.42 Linearity error of the all passive DAP based sensor

This causes not only a change of the amplitude of the received optical signal. Also the optical power distribution at the DAP surface changes rapidly. This results in a change of the separation efficiency η_{sep} because the point of maximum optical power moves closer to one or the other anode. Out of this also the separation speed may vary because deeply penetrating photons impinging on the DAP device see a different local electric field at the point of the electron-hole pair generation, depending on the impinging point. Since the change of the travel time through the device is only 200ps this effect cannot be measured directly.

Further investigations on this phenomenon could help to further decrease the linearity error. For instance a redesign of the position of the anodes at surface of the DAP device could help to reduce this effect. Also the use of an illumination source generating a more homogenous optical power distribution at the object surface e.g. by using an optical diffuser could help.

Also the minimal achievable standard deviation directly depends on the properties of the optical setup. The standard deviation of the sensor is calculated for the same data set of distance measurement points as was used to determine the distance measurement characteristic. The result is depicted in Figure 6.43. For a single distance measurement time of $t_{measure}$ = 5ms and an optical transmitted power of P_{opt} = 1.6mW the maximum standard deviation is less than σ_d = 3.4cm. It also decreases from large distances towards smaller ones and again increases around $s_{measure}$ = 5m. The increase dates from the non-perfect optical setup. Nevertheless for object distances shorter than s = 10m the standard deviation is kept below σ_d = 2cm. This is low enough for many control tasks.

As was shown the main limitation of the sensor is the unsatisfying optical setup. Especially for the measurement of short distances dedicated lenses have to be developed to be able to build up a three-dimensional measurement system without moving parts. The development of these lenses is not part of this work and has to be done by an optical system designer.

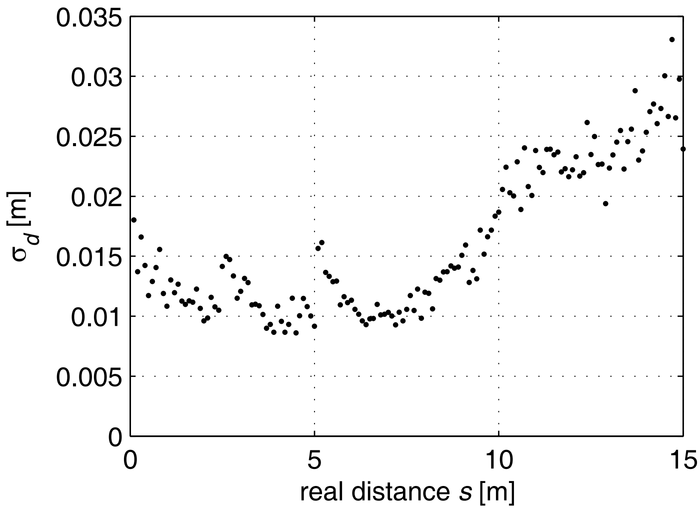

Figure 6.43 Standard deviation of the all passive DAP based sensor

Another interesting property of the active transimpedance stage is shown in Figure 6.44. It shows the dependence of the standard deviation on the amplitude of the fundamental wave of the output voltage V_{out}. With increasing amplitude the standard deviation decreases approximately according to one over V_{out}. This behaviour is typical for a system having a constant noise floor. The signal-to-noise ratio increases linearly with the increasing output signal V_{out}.

The more interesting detail dates from the change of the output voltage. It ranges approximately from $V_{out} = 0.7\text{mV}$ up to $V_{out} = 3.2\text{mV}$. Therefore the amplitude increases from far distant objects to closer ones only by a factor of 4.5. The receivable optical power for the same distance range of $s_d = 0.1\text{m}-15\text{m}$ changes according to (6.18) by a factor of 22500.

For far distant objects the coupling into the DAP device is almost ideal. Due to the poor focus behaviour of the receiving optics for short distances, resulting in a large spot diameter at the sensor surface, only a small amount of the received light is focused into the photodetector. By estimating that only one percent of the light reaches the photodetector still the change of the optical power is 225 times compared to a change of the output voltage by a factor of 4.5. In practice a change of the received optical power may also date from materials having a different reflectivity.

Out of this a strong compression of the dynamic range is performed by the transimpedance stage by mapping a large change of the received optical power onto a small change of the output voltage amplitude. In detail the output voltage change is 50 times lower than the change of optical power. Keeping the change of the output voltage level considerable low is especially important for a subsequent following ADC stage. If automatic gain switching of the ADC has to be avoided this is the only way to utilise the voltage measurement range in an optimal way and therefore to minimise additional quantisation noise.

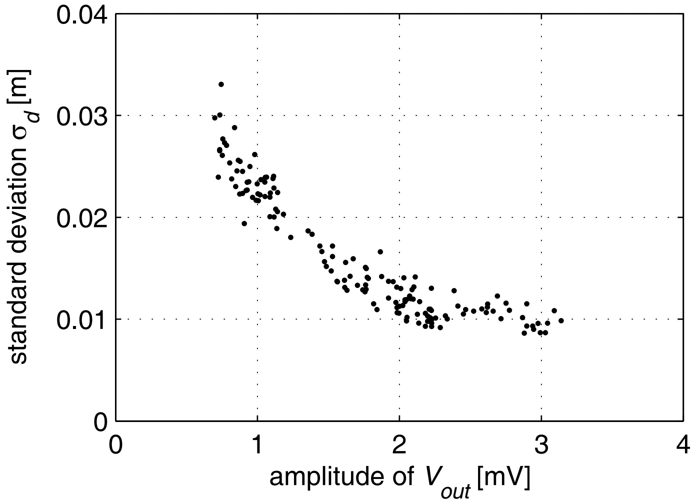

Figure 6.44 Dependence of the standard deviation on the output voltage amplitude of the all passive DAP based sensor

The newly developed OEIC with integrated double-anode photodetector and active transimpedance stage was fabricated in a modified 0.6µm BiCMOS technology. All modifications concerned the integration of PIN photodiodes. Especially the n^{-} type epitaxial layer provided by the technology to build photodiodes is necessary to implement the DAP device. The epitaxial layer serves as insulating layer between the p^{+} type anodes. Out of this it is possible to apply different voltages to the anodes without causing a feedthrough current flow in between. Furtheron an anti-reflection coating was used to maximise the DAP responsivity. A chip photograph of the realised opto-electronic integrated circuit is shown in Figure 6.45.

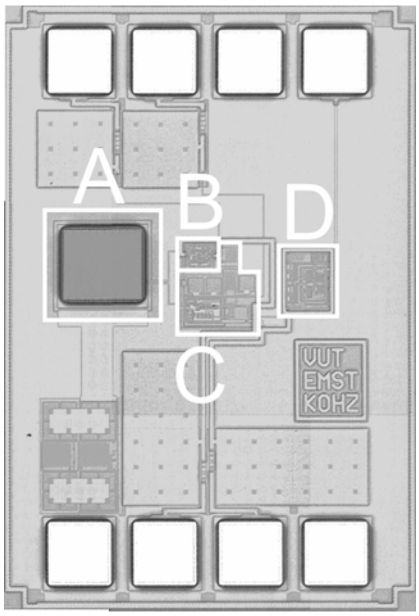

Figure 6.45 Chip photograph of the all-passive DAP based sensor

All functional blocks introduced in this chapter can be identified. The key component is the integrated double-anode photodetector A. The optical active area of the DAP device is $A_{pd} = 100{\times}100\mu m^2$. The clock driver stage used to provide the modulation voltage with variable amplitude and the inverse compensation signal is indicated as B. The entire readout circuit including the active transimpedance stage and the low-pass filter network are placed within the area C. Finally the output voltage buffer to drive the measurement equipment and to prevent distortions from the outside entering the readout circuit is named D. Furtheron blocking capacitors placed beside the voltage supply pads and an ESD protection circuit for the DAP device are shown.

For a multi-pixel design a small CMOS voltage follower to be included in every pixel is sufficient to perform the decoupling operation. The larger and therefore more power consuming voltage follower used here to drive the measurement equipment is only necessary as output buffer stage. Also the clock driver stage is not necessary in every pixel. Out of this only the photodetector block A and the readout block C are necessary within every pixel. The area occupation of the pixel therefore is $A_{pixel} = 150{\times}220\mu m^2$. Based on the active photodetector area of $A_{pd} = 100{\times}100\mu m^2$ this results in an optical fill factor of $\eta_{fill} = 30\%$.

7 Conclusion and Comparison with State-of-the-Art Systems

Within this thesis the development and reached measurement results of three new types of opto-electronic integrated correlation receivers for time-of-flight based distance measurement systems are shown. The common problem of measuring the distance of an object by determining the travel time of light from the transmitter to the object and back to the receiver has been solved by three substantially different operating principles.

To be able to compare the results reached by the three receiver concepts with current solutions an overview of the state-of-the-art of optical distance measurement systems is given in the beginning. Prior to the development of new receivers the expectable physical conditions had to be specified. They are:

- eye-safety
- non-cooperative object
- measurement distances up to some meters
- accuracy in the cm range

Due to eye-safety reasons the transmittable optical power is limited to the mW range. The objects are made of materials occurring in daily life, this means they are diffuse reflecting objects. The combination of low transmittable power and diffuse reflecting objects leads to a receivable optical power in the nW range. The dynamic range is more than three decades. Because of the very high vacuum speed of light of $c_0 = 3\times10^8$m/s the TOF to be measured is 6.6ns per meter at an accuracy of 66ps per cm.

To determine the short time delay of the very weak optical signal at a high accuracy direct time measurement cannot be performed. To solve the problem the optical signal is square-wave modulated. Afterwards the sent electrical and the received optical signal are correlated by the newly developed receivers. From the resulting correlation function the distance information is retrieved. Two different concepts to gain the distance information, namely a least square and a Fourier transform based approach have been investigated. The Fourier transform based algorithm turned out to be more robust. The systematic error introduced by the FFT due to sampling of non-bandwidth limited signals has been quantified. Out of this a minimum number of $N = 16$ equidistant samples of the correlation function are necessary to keep the resulting error sufficiently low. As fundamental physical lower border of the reachable accuracy the photon noise of the received optical signal was identified. The influence of the measurement principle was investigated in detail. The key results are that the standard deviation depends on the number of received photons, on the correlation process and on the modulation frequency. Photons caused by uncorrelated background light degrade the reachable accuracy.

One key element to measure the distance of the object accurately is to detect the received optical signal in an optimal way. Two different types of integrated photodetectors, realised in a modified 0.6µm BiCMOS technology, have been used during this work. These are a PIN photodiode and a newly developed double-anode photodetector. By supplying a sufficiently large bias voltage to the PIN photodiode a bandwidth of $f_{3dB} = 3$GHz and a responsivity of $R = 0.36$A/W at a wavelength of $\lambda = 660$nm is reached. The output signal is a signal proportional current. The DAP device directly performs an opto-electronic correlation. Different structures have been realised. For a DAP with metallised fingers a separation efficiency of $\eta_{sep} = 0.58\%$ at $\lambda = 660$nm was measured. For a DAP device without metallisation a responsivity of $R = 0.43$A/W at $\lambda = 660$nm was reached, which is close to a quantum efficiency of 100%. The output signal of the DAP consists of two DC currents at the anodes. The distance information is contained in the difference of both currents.

Based on the knowledge about the physical restrictions, the expectable input currents, the correlating principle and the properties of the photodetector elements new readout circuits could be developed. Due to the different output signal waveforms of the detectors different readout circuits were implemented. In parallel to the development of the circuits also an entire measurement setup consisting of a CPLD based high-speed electrical signal generator, signal proportional optical power generation, an opto-mechanical setup, electrical signal acquisition and online software processing was developed.

Each circuit topology is optimised for one parameter. A high-speed readout circuit was implemented to minimise measurement time. A bridge-correlator circuit deals with the optimal suppression of background light. A DAP-based circuitry was implemented to reach maximum sensitivity. All results are summarised in Table 7.1 together with all accessible data of current state-of-the-art systems.

The first circuit topology for high-speed distance measurements consists of a PIN photodiode as detector element and an active readout circuit. The main idea to reach short measurement times is to directly amplify the received signal and to avoid any slow integration process. A transimpedance amplifier for pre-amplification and an active correlating stage were implemented on the same chip. The suppression of background light is done by a differential correlation stage. The diameter of the PIN photodiode is $d_{pd} = 100\mu$m. The overall pixel size is $A_{pixel} = 220 \times 400\mu m^2$. This results in a fill factor of $\eta_{fill} = 9\%$. The single distance measurement time is only $t_{measure} = 500\mu$s for a range up to 3.7m. Having a look at Table 7.1 this measurement time is short compared to the other systems. Only the pulsed runtime system introduced in [13] and [14] reaches a higher frame rate by using an optical peak power of $P_{opt} = 70$W. With averaging a linearity error of $s_{lin} = 2$cm/5cm at a measured distance of $s_{measure} = 2$m/3.7m could be achieved for an optical transmitted power of $P_{opt} = 1.44$mW. For a future redesign, optimisation of the readout circuit to minimise additional noise has to be done. By reducing the noise level the distance measurement range can be increased and the standard deviation decreased. Also the total chip area of the pixel A_{pixel} has to be reduced to increase the optical fill factor η_{fill}.

The second correlation concept takes care of the suppression of background light. Perfect suppression of even strong background illumination can only be reached by processing the DC current signal already in the first circuit stage. This property is reached by the bridge-correlator circuit. Again a high-speed PIN photodiode serves as detector element. The output current charges an integration capacitor C_{int} during the first half period. During second half period the capacitor is switched in the opposite way and the photocurrent discharges C_{int}. Therefore a DC current is cancelled out within one period, resulting in an optimal background light suppression. The signal current is instead accumulated on C_{int}. A detailed model of the circuit was developed to describe the low-frequent behaviour. It turned out that the presence of the parasitic photodiode capacitance C_{pd} limits the output voltage and therefore the maximum reachable correlation sensitivity η_{sen}. The future development of low-capacitance photodiodes will help to improve the sensitivity of the all-passive circuit.

The passive bridge-correlator circuit was developed in two design steps. For the *first-silicon OEIC* an external differential amplifier having a differential gain of 10 was necessary. The *redesigned version* already contains an internal differential amplifier having a gain of 100. The redesigned bridge-correlator circuit is capable of measuring distances within the range of $s_d = 0.1\text{m}-3.7\text{m}$ for a transmitted optical power of $P_{opt} = 1.5\text{mW}$ within $t_{measure} = 2\text{ms}$. Compared to other systems of Table 7.1 this is still very fast. Therefore repetition rates of 500s^{-1} are possible. The linearity error is $s_{lin} = \pm 2\text{cm}$. Suppression of background light is inherently given by the circuitry due to the bipolar modulation process. The standard deviation of $\sigma_d = 2\text{cm}$ for an integration capacitor of $C_{int} = 2\text{pF}$ and reduced parasitic capacitance is very low. Only the external MSM-based, non multi-pixel capable system of [25] and the CMOS-CCD based system presented in [29] and [31] reach a lower standard deviation. To lower the influence of background light the CMOS-CCD system needs an additional circuitry within every pixel.

A further development of the bridge-correlator circuit including an active amplifier within every pixel led to the third-generation OEIC. By using the bridge circuit as a feedback network for the amplifier it is now possible to reduce the saturation effect of the original bridge-correlator setup very well. The circuit performs an integration of the received signal I_{pd} and suppresses background light at the same time. The measured output voltage is at least 30 times higher than for the passive bridge circuit. The measurement range of the OEIC without adjusting the optical setup is $s_d = 0.7\text{m}-3.4\text{m}$ and is only limited by the optical setup itself. The linearity error is $s_{lin} = \pm 2\text{cm}$. The standard deviation is only $\sigma_d = 1.4\text{cm}$ which is the lowest value reported for monolithically integrated continuous-wave systems. The pixel size is only $A_{pd} = 85\times 180\mu\text{m}^2$ resulting in a two-dimensional fill factor of $\eta_{fill} = 61\%$. This is the highest value being reported so far comparing to other state-of-the-art systems.

The final and most sensitive system introduced in this thesis relies on the correlation capability of the double-anode photodetector. The DAP device used to correlate the electrical sent signal with the optical received signal is modulated only single-sided. A compensation network to suppress charge injection due to coupling between both anodes is added. The DC output current is fed to a stack of diode-connected MOS transistors which form a current-dependent transimpedance. This current dependency is used to map the high dynamic range of the optical signal onto a small dynamic range of the output voltage. A low-pass filter network to suppress high-frequent distortions is also implemented on-chip. Due to the extremely high impedance of the diodes for low input currents a high sensitivity is reached. The DAP-based pixel is capable of measuring distances in the range of $s_d = 0.1\text{m}-15\text{m}$ for a total transmitted optical power of $P_{opt} = 1.6\text{mW}$. Even for the low received optical power of $P_{opt,rec} = 2.8\text{nW}$ at $s = 15\text{m}$

a measurement time of only $t_{measure}$ = 5ms was achieved. The overall linearity error is only s_{lin} = ±3.5cm corresponding to ±0.23%, also the standard deviation of σ_d = 3.4cm is low compared to the large distance measurement range. Only circuits developed at our institute during this work were capable of measuring distances up to s_d = 15m, but with longer single distance measurement times. The pixel size of the elements necessary in every pixel of A_{pixel} = 150×220µm^2 leads to a high fill factor of η_{fill} = 30% compared to other solutions.

In this thesis the development of four new types of opto-electronic integrated receivers from the idea to the realisation has been presented. A high-speed, a passive and an active background-light suppressing and a highly sensitive circuit topology have been shown. To combine these good properties in one circuit will be the challenging and interesting task, necessary to realise a future 3D distance measurement system, which can be used for mass applications.

System	Operating Principle	Process	Max Supply Voltage	Bandwidth	Measurement Time	Frames per second	Pixel Count	Pixel Size	fill factor	Wavelength	Mean Optical Power	Max Optical Power	Range	Standard Deviation	Linearity Error	Resolution
			V	MHz	ms	fps		µm²	%	nm	mW	W	m	mm	mm	mm
Triangulation [6]	T	0.18µm CMOS	1.8			1052	375x365	11.25x11.25		635	300		0.55-0.65	0.47	1.1	
Pulsed Run Time [10]	P	0.35µm BiCMOS SiGE	3.3	1600			1	external PD						8		
CMOS with TVC [13], [14]	P	0.5µm CMOS	3.3			19.5k	4x64	130x300	100	850-910		70	8			50
CMOS with OTA [15], [17]	P	0.35µm CMOS	3.3			30	16x16	80x80	20	905	1000		2-9	450	90	
SPAD with TDC [20], [21]	P	0.8µm HV CMOS	-25.5			> 3.9	true 32x32	58x58		635	1	0.25	3.75	1.3		
SPAD with TVC [22]	P	0.8µm mod. HV CMOS	-25				1x64	38x180	0.29	905	250	250	2-5	37.5		
MSM [25]	C	discrete setup						external PD					0.55-0.75	12.13		
PMD [27]	C	0.6µm CMOS		>100			48x64	100x100	32	870	3000		1.5-3.5	35		6
CMOS-CCD [29], [31]	C	custom 0.6µm CMOS/CCD	9	43	4		176x144	n.a.		870	1000		0.5-2, 1-6	16	100	
Gates on Field Oxide [32], [33]	C	0.35µm CMOS	3.3			30	336x252	15x15		870			1-3	>28		
Correlating PIN-Detector [34]	*C*	*0.6µm mod. BiCMOS*	*5*		*20*		*1*	*250x170*	*24*	*650*	*1.6*		*0.1-15*	*50*	*100*	
PIN+TIA+OPA [36]	*C*	*0.6µm mod. BiCMOS*	*5*	*260*	*100*		*1*	*230x450*	*8*	*650*	*1.6*		*0.1-15*	*70*	*300*	
PIN+TIA+Mixer [45]	***C***	***0.6µm mod. BiCMOS***	***5***	***260***	***0.5***		***1***	***220x400***	***9***	***650***	***1.44***		***0.1-3.7***	***40***	***50***	
PIN-Bridge first-silicon *[48]*, ***[49], [50]***	***C***	***0.6µm mod. BiCMOS***	***5***	***>1350***	***8***		***1***	***150x200***	***10***	***650***	***2***		***0.1-3.7***	***27***	***70***	
PIN-Bridge redesigned *[51]*	***C***	***0.6µm mod. BiCMOS***	***5***	***>1350***	***2***		***1***	***250x200***	***16***	***650***	***1.5***		***0.1-3.7***	***20***	***40***	
enhanced-sensitivity PIN-Bridge	***C***	***0.6µm mod. BiCMOS***	***5***	***>1000***	***5***		***1***	***85x180***	***61***	***650***	***1***		***0.7-3.4***	***14***	***40***	
DAP Double Sided ***[44]***, ***[49]***, ***[50]***, *[52]*	*C*	*0.6µm mod. BiCMOS*	*8*	*500*	*32*		*1*	*125x300*	*6*	*650*	*1*		*0.4-2*		*50*	
DAP Single Sided [54]	***C***	***0.6µm mod. BiCMOS***	***8***	***500***	***5***		***1***	***150x220***	***30***	***650***	***1.6***		***0.1-15***	***34***	***70***	

Operating principle: T Triangulation, P Pulsed run time, C Continous Wave
Italic style: Work done within the project
bold style: Own results

Table 7.1 Comparison of state-of-the-art systems with own work

References

[1] H. H. Meinel; "Automotive radar and related traffic applications of millimeterwaves", *Topical Symposium on Millimeter Waves*, pp. 151-154, 1997

[2] G. Brumbi, "Grundlagen der Radartechnik zur Füllstandsmessung", Moers: Skriptum FH-Degendorf, 2003

[3] R. H. Raßhofer, "Radarsensoren mit aktiven, integrierten Millimeterwellenantennen", München: 1999

[4] Y. Oike, M. Ikeda, K. Asada; "Design of real-time VGA 3-D image sensor using mixed-signal techniques", *Proceeding of the ASP-DAC*, pp. 523-524, 2004

[5] Y. Oike, M. Ikeda, K. Asada; "Design and implementation of real-time 3-D image sensor with 640 x 480 pixel resolution", *IEEE Journal of Solid States*, vol. 39, no. 4, pp. 622-628, 2004

[6] Y. Oike, M. Ikeda, K. Asada; "A 375 × 365 3D 1k frame/s range-finding image sensor with 394.5 kHz access rate and 0.2 subpixel accuracy", *IEEE ISSCC Digest of Technical Papers*, pp. 118-119, 2004

[7] Y. Oike, M. Ikeda, K. Asada; "A 375 × 365 high-speed 3-D range-finding image sensor using row-parallel search architecture and multisampling technique", *IEEE Journal of Solid-State Circuits*, vol. 40, no. 2, pp. 444-453, 2005

[8] G. A. Reider, "Photonik: eine Einführung in die Grundlagen", Wien: Springer, 2005

[9] S. Kurtti, J. Kostamovaara; "An integrated optical receiver with widerange timing discrimination characteristics", *Proceeding of the 31st ESSCIRC*, pp. 435-438, 2005

[10] J. Pehkonen, P. Palojarvi, J. Kostamovaara; "Receiver Channel with Resonance-Based Timing Detection for a Laser Range Finder", *IEEE Transactions on Circuits and Systems-I*, vol. 53, no. 3, pp. 569-577, 2006

[11] E. Raisanen-Ruotsalainen, T. Rahkonen, J. Kostamovaara; "An integrated time-to-digital converter with 30-ps single-shot precision", *IEEE Journal of Solid States*, vol. 35, no. 10, pp. 1507-1510, 2000

[12] P. Palojarvi, K. Maatta, J. Kostamovaara; "Pulsed time-of-flight laser radar module with millimeter-level accuracy using full custom receiver and TDC ASICs", *IEEE Transactions on Instrumentation and Measurement*, vol. 51, no. 5, pp. 1102-1108, 2002

[13] O. Schrey, O. Elkhalili, P. Mengel, M. Petermann, W. Brockherde, B. Hosticka; "A 4×64 Pixel CMOS Image Sensor for 3-D Measurement Applications", *Proceeding of the 29st ESSCIRC*, pp. 333-336, 2003

[14] O. Elkhalili, O. Schrey, P. Mengel, M. Petermann, W. Brockherde, B. Hosticka; "A 4×64 Pixel CMOS Image Sensor for 3-D Measurement Applications", *IEEE Journal of Solid-State Circuits*, vol. 39, no. 7, pp. 1208-1212, 2004

[15] L. Viarani, D. Stoppa, L. Gonzo, M. Gottardi, A. Simoni; "A CMOS smart pixel for active 3-D vision applications", *IEEE Sensors Journal*, vol. 4, no. 1, pp. 145-152, 2004

[16] D. Stoppa, L. Viarani, A. Simoni, L. Gonzo, M. Malfatti; "A new architecture for TOF-based range-finding sensor", *Proceedings of IEEE Sensors*, vol. 1, pp. 481-484, 2004

[17] D. Stoppa, L. Viarani, A. Simoni, L. Gonzo, M. Malfatti, G. Pedretti; "A 16×16-Pixel Range-Finding CMOS Image Sensor", *Proceeding of ESSCIRC 2004*, pp. 419-422, 2004

[18] A. Rochas, A. Pauchard, P. Besse, D. Pantic, Z. Prijic, R. Popovic; "Low-noise silicon avalanche photodiodes fabricated in conventional CMOS technologies", *IEEE Transactions on Electron Devices*, vol. 49, no. 3, pp. 387-394, 2002

[19] A. Rochas, M. Gosch, A. Serov, P. Besse, R. Popovic, T. Lasser, R. Rigler; "First fully integrated 2-D array of single-photon detectors in standard CMOS technology", *IEEE Photonics Technology Letters*, vol. 10, no. 4, pp. 963-965, 2003

[20] C. Niclass, A. Rochas, P. Besse, E. Charbon; "Design and characterization of a CMOS 3-D image sensor based on single photon avalanche diodes", *IEEE Journal of Solid States Circuits*, vol. 40, no. 9, pp. 1847-1854, 2005

[21] C. Niclass, E. Charbon; "A single photon detector array with 64×64 resolution and millimetric depth accuracy for 3D imaging", *IEEE ISSCC Digest of Technical Papers*, vol. 1, pp. 364-365 604, 2005

[22] D. Stoppa, L. Pancheri, M. Scandiuzzo, M. Malfatti, G. Pedretti, L. Gonzo; "A Single-Photon-Avalanche-Diode 3D Imager", *Proceeding of the 31st ESSCIRC*, pp. 487-490, 2005

[23] P. Gulden, M. Vossiek, P. Heide, R. Schwarte; "Novel opportunities for optical level gauging and 3D-imaging with the photoelectronic mixing device", *IEEE Transactions on Instrumentation and Measurements*, vol. 51, no. 4, pp. 679-684, 2002

[24] P. Gulden, D. Becker, M. Vossiek; "Systematic distortions in electro-optical mixers", *Proceedings of IEEE Sensors*, vol. 2, pp. 1026-1031, 2003

[25] P. Gulden, D. Becker, M. Vossiek; "Novel optical distance sensor based on MSM technology", *IEEE Sensors Journal*, vol. 4, no. 5, pp. 612-618, 2004

[26] R. Schwarte; "Dynamic 3D-Vision", *Proceeding of the International Symposium on Electron Devices for Microwave and Optoelectronic Applications*, pp. 241-248, 2001

[27] H. Kraft, J. Frey, T. Moeller, M. Albrect, M. Grothof, B. Schink, H. Hess, B. Buxbaum; "3D-Camera of High 3D-Frame Rate, Depth-Resolution and Background Light Elimination Based on Improved PMD (Photonic Mixer Device)-Technologies", *Proceedings of 6th OPTO*, pp. 95-100, 2004

[28] R. Lange, P. Seitz, A. Biber, S. Lauxtermann; "Demodulation pixels in CCD and CMOS technologies for time-of-flight ranging", *SPIE Sensors and Camera Systems for Scientific, Industrial, and Digital Photography Applications*, vol. 3965, pp. 177-188, 2000

[29] T. Oggier, R. Kaufmann, M. Lehmann, B. Büttgen, S. Neukom, M. Richter, M. Schweizer, P. Metzler, F. Lustenberger, N. Blanc; "Novel pixel architecture with inherent background suppression for 3D time-of-flight imaging", *Proceedings of SPIE - Electronic Imaging*, vol. 5665, pp. 1-8, 2005

[30] T. Oggier, R. Kaufmann, M. Lehmann, P. Metzler, G. Lang, M. Schweizer, M. Richter, B. Büttgen, N. Blanc, K. Griessbach, B. Uhlmann, K. Stegemann, C. Ellmers; "3D-Imaging in Real-Time with Miniaturized Optical Range Camera", *Proceedings of 6th OPTO*, pp. 89-94, 2004

[31] B. Büttgen, T. Oggier, M. Lehmann, R. Kaufmann, S. Neukom, M. Richter, M. Schweizer, D. Beyeler, R. Cook, C. Gimkiewicz, C. Urban, P. Metzler, P. Seitz, F. Lustenberger; "High-Speed and High-Sensitive Demodulation Pixel for 3D-Imaging", *Proceedings of SPIE - Three-Dimensional Image Capture and Applications VII*, vol. 6056, pp. 22-33, 2006

[32] T. Ushinga, I. Abdul Halin, T. Sawada, S. Kawahito, M. Homma, Y. Maeda; "A QVGA-size CMOS time-of-flight range image sensor with background light charge draining structure", *Proceedings of SPIE - Three Dimensional Image Capture and Applications VII*, vol. 6056, pp. 34-41, 2006

[33] A. Izhal, T. Ushinga, T. Sawada, M. Homme, Y. Maeda, S. Kawahito; "A CMOS Time-of-Flight Range Image Sensor with Gates on Field Oxide Structure", *Proceedings of IEEE Sensors Conference*, pp. 141-144, 2005

[34] A. Nemecek, K. Oberhauser, H. Zimmermann; "Correlating PIN-photodetector with novel difference-integrator concept for rangefinding applications", *Proceeding of the 31st ESSCIRC*, pp. 491-494, 2005

[35] A. Nemecek, K. Oberhauser, H. Zimmermann; "Single-chip optoelectronic rangefinder using PIN-photodiode and correlated active integration", *Proceedings of SPIE*, vol. 5954, no. 0D, pp. 1-10, 2005

[36] A. Nemecek, K. Oberhauser, C. Seidl, H. Zimmermann; "PIN-Diode Based Optical Distance Measurement Sensor for Low Optical Power Active Illumination", *Proceedings of 4th IEEE Sensors Conference*, pp. 861-864, 2005

[37] Riegl Laser Measurement Systems (2006, April) Reflectivity of Various Surfaces. [Online]. Available: http://www.riegl.com/distancemeters_/distancemeter_applications_/notes_/e_gi004.htm

[38] T. Ringbeck, "Untersuchung opto-elektrischer Phasenregelkreise auf Basis von Photomischdetektoren hinsichtlich deren Anwendungspotential für die Photonik", Shaker-Verlag, 2002

[39] P. Palojarvi, K. Maatta, J. Kostamovaara; "Integrated time-of-flight laser radar", *IEEE Transactions on Instrumentation and Measurements*, vol. 46, no. 4, pp. 996-999, 1997

[40] D. E. Aspnes, A. A. Studna; "Dielectric functions and optical parameters of Si, Ge, GaP, GaAs, GaSb, InP, InAs, and InSb from 1.5 to 6.0 eV", *Physical Review*, vol. B 27, no. 2, pp. 985-1009, 1983

[41] H. Zimmermann, "Integrated Silicon Optoelectronics", Heidelberg: Springer-Verlag, 2000

[42] M. McClish, R. Farrell, K. Vanderpuye, K. Shah; "A Reexamination of Silicon Avalanche Photodiode Gain and Quantum Efficiency", *IEEE Nuclear Science Symposium Conference Record*, vol. 5, pp. 2959-2962, 2005

[43] A. Nemecek, K. Oberhauser, G. Zach, H. Zimmermann; "Fast and efficient integrated silicon PIN-finger photodetector from ultraviolet up to near infrared", *Proceeding of the IEEE International conference on Group IV Photonics*, pp. 108-110, 2005

[44] K. Oberhauser, A. Nemecek, C. Sünder, H. Zimmermann; "Universal integrated PIN photodetector", *Proceeding of the 34th European Solid-State Device Research conference*, pp. 349-352, 2004

[45] K. Oberhauser, A. Nemecek, H. Zimmermann; "PIN-photodiode based pixel architecture for high-speed optical distance measurement systems", *Proc. SPIE Detectors and Associated Signal Processing II*, vol. 5964, pp. 135-144, 2005

[46] R. Tao, M. Berroth, Z. Wang; "Monolithically integrated CMOS current-mode transimpedance", *Electronics Letters*, vol. 39, no. 25, pp. 1772-1774, 2003

[47] C. Seidl, J. Knorr, H. Zimmermann; "Simple feedback network for bandwidth enhancement of transimpedance amplifiers", *Electronic Letters*, vol. 39, no. 25, pp. 1849-1851, 2003

[48] A. Nemecek, K. Oberhauser, H. Zimmermann; "PIN-bridge distance measurement sensor", *Proceeding of the IEEE Sensors conference*, vol. 3, pp. 1538-1541, 2004

[49] K. Oberhauser, A. Nemecek, H. Zimmermann; "Integrierte Korrelationsempfänger für laufzeitbasierte optische Abstandsmessung", *Tagungsband XVIII. Messtechnisches Symposium*, pp. 54-63, 2004

[50] K. Oberhauser, A. Nemecek, H. Zimmermann; "Monolithische Korrelationsempfänger für optische Abstandsmessung", *tm - Technisches Messen*, vol. 72, no. 4, pp. 230-235, 2005

[51] A. Nemecek, K. Oberhauser, H. Zimmermann; "Distance Measurement Sensor With PIN-Photodiode and Bridge Circuit", *IEEE Sensors Journal*, vol. 6, no. 2, pp. 391-397, 2006

[52] A. Nemecek, K. Oberhauser, H. Zimmermann; "Integrated Optical Distance Measurement Correlation Sensor", *Proceedings of ODIMAP IV*, pp. 170-175, 2004

[53] K. Oberhauser, A. Nemecek, H. Zimmermann; "Time-of-Flight Based Distance Measurement Sensor with Integrated Double-Anode Photodetector", *Proceedings of IEEE MELECON 06*, pp. 377-380, 2006

[54] K. R. Laker, W. M. C. Sansen, "Design of Analog Integrated Circuits and Systems", Singapore: McGraw-Hill Book Co., 1994

[55] Universität Erlangen (2006, September) Physikalische Grundlagen, Lichtquellen, Filter, Monochromatoren, Meßgeräte. [Online]. Available: http://www.biologie.uni-erlangen.de/botanik1/photobiologie/kapitel_1.htm

List of Publications

[1] A. Nemecek, K. Oberhauser, H. Zimmermann; "Integrated Optical Distance Measurement Correlation Sensor", *Proceedings of ODIMAP IV*, pp. 170-175, 2004

[2] K. Oberhauser, A. Nemecek, C. Sünder, H. Zimmermann; "Universal integrated PIN photodetector", *Proceeding of the 34th European Solid-State Device Research conference*, pp. 349 - 352, 2004

[3] A. Nemecek, K. Oberhauser, H. Zimmermann; "PIN-bridge distance measurement sensor", *Proceeding of the IEEE Sensors conference*, vol. 3, pp. 1538-1541, 2004

[4] K. Oberhauser, A. Nemecek, H. Zimmermann; "Integrierte Korrelationsempfänger für laufzeitbasierte optische Abstandsmessung", *Tagungsband XVIII. Messtechnisches Symposium*, pp. 54-63, 2004

[5] K. Oberhauser, A. Nemecek, H. Zimmermann; "Monolithische Korrelationsempfänger für optische Abstandsmessung", *tm - Technisches Messen*, vol. 72, no. 4, pp. 230-235, 2005

[6] A. Nemecek, K. Oberhauser, G. Zach, H. Zimmermann; "Fast and efficient integrated silicon PIN-finger photodetector from ultraviolet up to near infrared", *Proceeding of the IEEE International conference on Group IV Photonics*, pp. 108-110, 2005

[7] A. Nemecek, K. Oberhauser, H. Zimmermann; "Single-chip optoelectronic rangefinder using PIN-photodiode and correlated active integration", *Proceedings of SPIE*, vol. 5954, no. 0D, pp. 1-10, 2005

[8] A. Nemecek, K. Oberhauser, C. Seidl, H. Zimmermann; "PIN-Diode Based Optical Distance Measurement Sensor for Low Optical Power Active Illumination", *Proceedings of 4th IEEE Sensors Conference*. pp. 861-864, 2005

[9] A. Nemecek, K. Oberhauser, H. Zimmermann; "Correlating PIN-photodetector with novel difference-integrator concept for rangefinding applications", *Proceeding of the 31st ESSCIRC*, pp. 491-494, 2005

[10] K. Oberhauser, A. Nemecek, H. Zimmermann; "PIN-photodiode based pixel architecture for high-speed optical distance measurement systems", *Proc. SPIE Detectors and Associated Signal Processing II*, vol. 5964, pp. 135-144, 2005

[11] K. Schneider, R. Swoboda, M. Förtsch, K. Oberhauser, A. Nemecek, C. Seidl, J. Leeb, H. Zimmermann; "High-end opto ASICs for DVD, data communication receivers and optical distance measurement", *e&i elektrotechnik und informationstechnik*, no. 12, pp. 446-451, 2005

[12] K. Oberhauser, A. Nemecek, H. Zimmermann; "Time-of-Flight Based Distance Measurement Sensor with Integrated Double-Anode Photodetector", *Proceedings of IEEE MELECON 06*, pp. 377-380, 2006

[13] A. Nemecek, K. Oberhauser, H. Zimmermann; "Distance Measurement Sensor With PIN-Photodiode and Bridge Circuit", *IEEE Sensors Journal*, vol. 6, no. 2, pp. 391-397, 2006

[14] A. Nemecek, G. Zach, R. Swoboda, K. Oberhauser, H. Zimmermann; "Integrated BiCMOS PIN Photodetectors with High Bandwidth and High Responsivity", *IEEE Journal of Selected Topics in Quantum Electronics*, pp. accepted, 2006

[15] A. Nemecek, K. Oberhauser, H. Zimmermann; "Distance Measurement Line Sensor with PIN Photodiodes", *Proceeding of the IEEE Sensor Conference*, pp. accepted, 2006

Lebenslauf

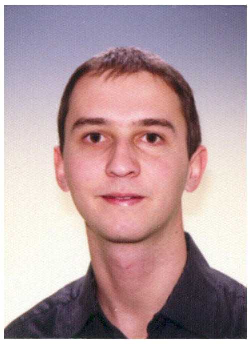

<u>Persönliches</u>	DI Klaus Oberhauser geboren am 11. April 1977 in Dornbirn / Österreich Österreicher Ledig
<u>Anschrift</u>	Gentzgasse 120/10 A-1180 Wien tel. 01 – 47 99 626 mobil. 0650 – 841 8914 mail. klaus.oberhauser@tuwien.ac.at
<u>Ausbildung</u>	
Oktober 1997 – März 2003	Studium der **Elektrotechnik** an der Technischen Universität Wien 1. Diplomprüfung: Jänner 2000 2. Diplomprüfung und Abschluss mit Auszeichnung: März 2003 Diplomarbeit: Development of a Measurement and Control Component Library for IEC 61499 (Note: Sehr gut) Studienzweig: **Automatisierungs- und Regelungstechnik**
August 2000 – Juni 2001	**Auslandsstudium** an der Technischen Universität Lund (Schweden) Schwerpunkte: englischsprachige Kurse in den Bereichen Leistungselektronik, Echtzeitsysteme, Systemidentifikation, adaptive Regler, computergesteuerte Systeme und Automatisierungstechnik
September 1991 – Juni 1996	Höhere Technische Bundes- Lehr- und Versuchsanstalt Bregenz Elektrotechnik: Energietechnik und Leistungselektronik
Juni 1996	**Matura** (mit ausgezeichnetem Erfolg)
<u>Präsenzdienst</u>	
Okt. – Mai 1997	Ableistung des Präsenzdienstes (8 Monate)
<u>Berufserfahrung</u>	
seit April 2003	Wissenschaftlicher Mitarbeiter am Institut für elektrische Mess- und Schaltungstechnik an der TU-Wien Tätigkeitsbereiche: Entwicklung und Charakterisierung opto-elektronischer integrierter Schaltungen für die optische Abstandsmessung, selbständige Organisation und Abhaltung von Lehrveranstaltungen, Betreuung von Bakkalaureatsarbeiten

Juni – September 2001	**Eberle Automatische Systeme GmbH** Selbstständige Durchführung mehrerer Programmierprojekte in VB, HTML, PHP, JAVA-Script sowie vollständige Programmierung der Firmenhomepage www.eberle.at
Juni – Juli 2000 Juli – August 1999 Juli – August 1998 Juni – August 1997	**Bregenzer Festspiele GmbH** Bühnentechniker bei diversen Opernproduktionen, zuständig für Aufbau, Umbau und Abbau der Bühne, sowie Bedienung aller technischen Einrichtungen während der Vorstellungen
Juli – August 1996	**Doppelmayr Produktions GmbH**
Aug.– Sep. 1995 Juli – August 1994 Juli – August 1993	**Vorarlberger Kraftwerke AG** Portierung von Kundenstammdaten für die Umstellung der Stromverrechnung der VKW AG, Mitarbeit Zähler- und Messwesen
Studentische Tätigkeiten	
Oktober 2001 – Oktober 2002	Vorsitzender EESTEC LC-Vienna www.eestec.org (Electrical Engineering STudents European assoCiation) EESTEC ist eine europaweite, nicht politische Vereinigung, die in enger Zusammenarbeit mit Industrie und Universität bilaterale Austauschprogramme für Elektrotechnikstudenten organisiert.
Jänner 2000	Einwöchiger Aufenthalt an der Technischen Universität Oulu (Finnland) im Rahmen des EESTEC Programms
Sprachen	Englisch verhandlungssicher, Schwedisch Anfänger
DV-Kenntnisse	MS Office, Matlab, Simulink, LabView, JAVA, Cadence, MEDICI
Stipendien	
Dezember 2002 Jänner 2001	Zuerkennung zweier **Leistungsstipendien** durch die Fakultät für Elektrotechnik der Technischen Universität Wien
Juni 1996	Zuerkennung des **Förderungspreises** der Hilti AG
Hobbies	Theater, Inlineskaten, Schifahren, Schwimmen, Kino

Wien im November 2006